Magnetism and the Magnetic Excitations of Charge Ordered La$_{2-x}$Sr$_x$NiO$_{4+\delta}$

Paul Freeman

Condensed Matter Physics

Department of Physics

University of Oxford

Thesis submitted for the degree

of Doctor of Philosophy

University College

Trinity Term 2005

Magnetism and the Magnetic Excitations of Charge Ordered La$_{2-x}$Sr$_x$NiO$_{4+\delta}$

Paul Freeman

University College – University of Oxford

Trinity Term 2005

Abstract of thesis submitted for the degree of Doctor of Philosophy

Abstract

In this thesis I present an investigation into the magnetic order and magnetic excitations of charge-ordered La$_{2-x}$Sr$_x$NiO$_{4+\delta}$ using magnetization and neutron scattering techniques.

I have studied the magnetic ordering over a wide range of doping levels, $0 \leq x \leq 0.5$, using magnetization measurements and neutron diffraction. I have compared my magnetization study with earlier work carried out over a wider range of doping levels and with measurements at higher temperatures on similar doping levels. In the magnetization measurements I discovered unusual 'memory' effects of the remnant magnetization. My neutron diffraction measurements go to lower temperatures than previous studies and extend the range of doping levels that have been studied.

Inelastic neutron scattering was employed to study the spin wave excitations of charge-ordered La$_{2-x}$Sr$_x$NiO$_{4+\delta}$, for charge-ordering with a period either commensurate or incommensurate with the crystal lattice. The effect of incommensurate ordering on the exchange interactions was observed to be insignificant, with the excitations in the incommensurately ordered materials being found to be relatively short ranged. A dip in the intensity of the spin wave excitations of charge-stripe ordered La$_{2-x}$Sr$_x$NiO$_{4+\delta}$ was observed. One possibility is that this dip is due to a coupling of the excitations to a collective excitation of the charge-stripes. In checkerboard charge-ordered La$_{3/2}$Sr$_{1/2}$NiO$_4$ I observed new modes in the spin wave excitations, and I speculate the origin of these excitations to be due to variations of the spin ordering period in this material. I compare my findings with the spin wave excitations of the Néel antiferromagnetic La$_2$NiO$_4$.

At low energies, inelastic neutron scattering revealed another excitation mode of charge-ordered La$_{2-x}$Sr$_x$NiO$_{4+\delta}$. This mode was found to be consistent with antiferromagnetic correlations among the stripe electrons.

Acknowledgements

There are a large number of people who I wish to thank for the help they gave me in preparing this thesis. First, I would like to thank my supervisor, Andrew Boothroyd, for his patience, advise and clear insight. I would also like to thank the many instrument scientists at the ILL, ISIS and SINQ, particularly Mechthild Enderle, Arno Heiss, Jiri Kulda, Chris Frost, Felix Altorfer and Christof Niedermeyer for their help with the neutron scattering experiments. For insightful discussions on my work I would also like to thank José Lorenzana.

At the Clarendon Laboratory I would especially like to thank Prabhakaran Dharmal-ingham for growing the crystals for this work and for his help with the magnetization measurements. I would also like to thank Fred Wondre for his efforts in aligning crys-tals and Lucy Helme for her spin wave calculation and artistic advise. Along with these people I would also grateful for the good company of the many students, post-docs and researchers who have my time working in Oxford enjoyable. In this respect I would like to additionally thank Stephen Lister, Carol Webster, Alexandra Olaya-Castaro, Weibke Lohstroh, Sasha babkevich, Mark Bentall, Tom Huberman, Chiron Mukherjee, David Parfitt, Russell Ewings, Alan Tennant, Roger Cowley, Roger Ward, Mike Wells, Dave Keen, Radu Coldea, and Bella Lake.

Finally I would like to thank my parents and sister for their the love, support, encourage-ment and understanding.

Contents

List of Figures

List of Tables

Chapter 1

Introduction

In 1986 J. G. Bednorz and K. A. Müller discovered superconductivity in $La_{2-x}Ba_xCuO_4$ with an anomalously high superconducting temperature $T_C \approx 40\,K$ [1]. Unlike any previously discovered superconductor this material could not be explained by the standard BCS theory of J. Bardeen, L. N. Cooper, and J. R. Schrieffer[2]. The discovery by J. G. Bednorz and K. A. Müller lead to the the discovery of a whole series of other materials that could not be explained by BCS theory. In this sense superconductors can be split into two classes; conventional superconductors that can be explained by BCS theory and unconventional superconductors that can not be explained by BCS theory.

Unconventional superconductors that possess high T_C values are almost all copper based materials, known as high-temperature (H-T_C) superconductors or more loosely known as cuprates. A common feature of all H-T_C superconductors is a structure which consists of layers of copper oxide (CuO_2), that are separated by spacer layers containing elements such as lanthanum, barium or yttrium. The discovery of cuprate superconductivity above liquid nitrogen temperatures has revolutionized the use of superconductors.

The complex role of interactions in cuprate superconductors has not yet been determined.

To fully understand high temperature superconductivity the roles played by the different interactions in these materials must be understood. When this is achieved, we will be in a better position understand high temperature superconductivity.

1.1 Charge Order

The discovery of high temperature superconductors has lead to theoretical and experimental interest in understanding other doped layered antiferromagnets. Over the last decade it has become increasingly apparent that doped antiferromagnets exhibit ordered phases involving both spin and charge. Widespread interest in these ordered phases was caused by the discovery of a striped spin-charge ordered phase in a non-superconducting layered cuprate[3]. The role of such a striped spin-charge ordered phase in the superconducting state of the cuprates is unclear, although certain theoretical scenarios suggest that a spin gap along with pairing instabilities of stripe electrons could lead to superconductivity[4]. These findings underline the importance of understanding charge stripe order.

Figure 1.1 shows the basic crystal structure of $La_{2-x}Sr_xNiO_4$, which has a crystal structure that is typical of doped layered antiferromagnets. $La_{2-x}Sr_xNiO_4$ does not superconduct[5] but is isostructural with the cuprate superconductor $La_{2-x}Sr_xCuO_4$. The structure is made of layers of Ni-O conduction layers that are separated by spacer layers of La/Sr-O in a body centred tetragonal unit cell. Substitution of one atom of La by one atom of Sr in the spacer layer, introduces one hole into the conduction layer. So the spacer layer provides the charge carriers for the conduction layer which is responsible for the electrical properties of the material, although in the case of $La_{2-x}Sr_xNiO_4$ the material is far from a conductor for $x \leq 0.8$[6].

Charge order occurs in a generic way for different types of doped layered antiferromagnetic materials, with subtle variations between different materials. Figure 1.2 shows the general trend of the temperature evolution of charge-ordering for a single conduction layer of a doped antiferromagnet. At high temperatures the holes doped into the conduction
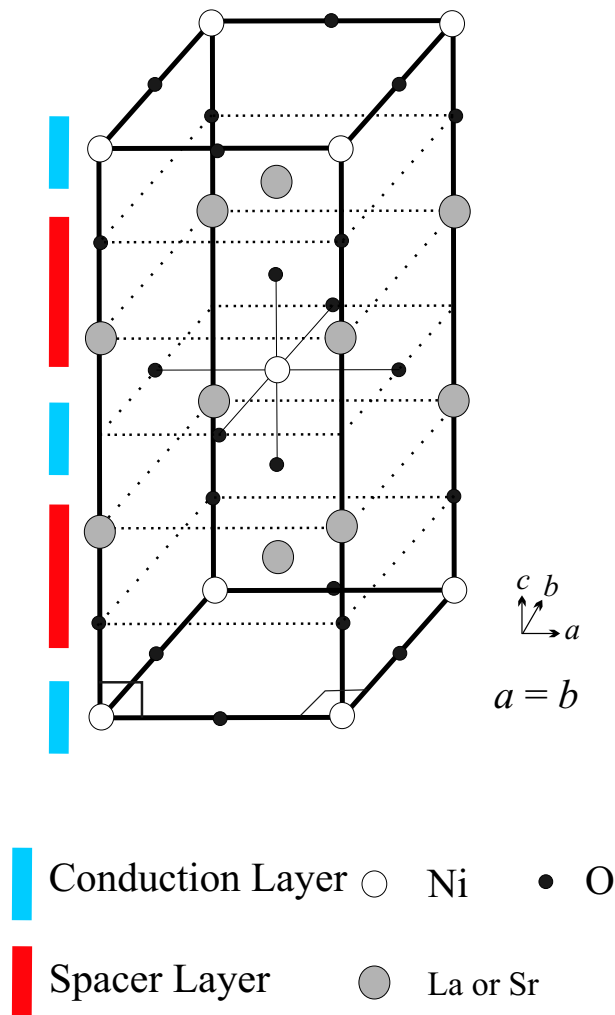
Figure 1.1: The crystal structure of $La_{2-x}Sr_xNiO_4$.

layer are randomly distributed, Fig. 1.2(a). On cooling the charges then line up into periodically spaced lines of charges, Fig. 1.2(b). These lines are known as charge-stripes, and they are centred either on the ionic metal sites or oxygen sites of the conduction layer depending on the material in question. On further reducing the temperature the spins of the metallic sites (the Ni^{2+} spins in the case of $La_{2-x}Sr_xNiO_4$) of the conduction layer order antiferromagnetically between the charge stripes, Fig. 1.2(c). The ordering of the spins is drastically affected by the charge ordering. Consider the top row of spins in Fig. 1.2(c), in the parent material the spins would be up-down-up-down-... but in the
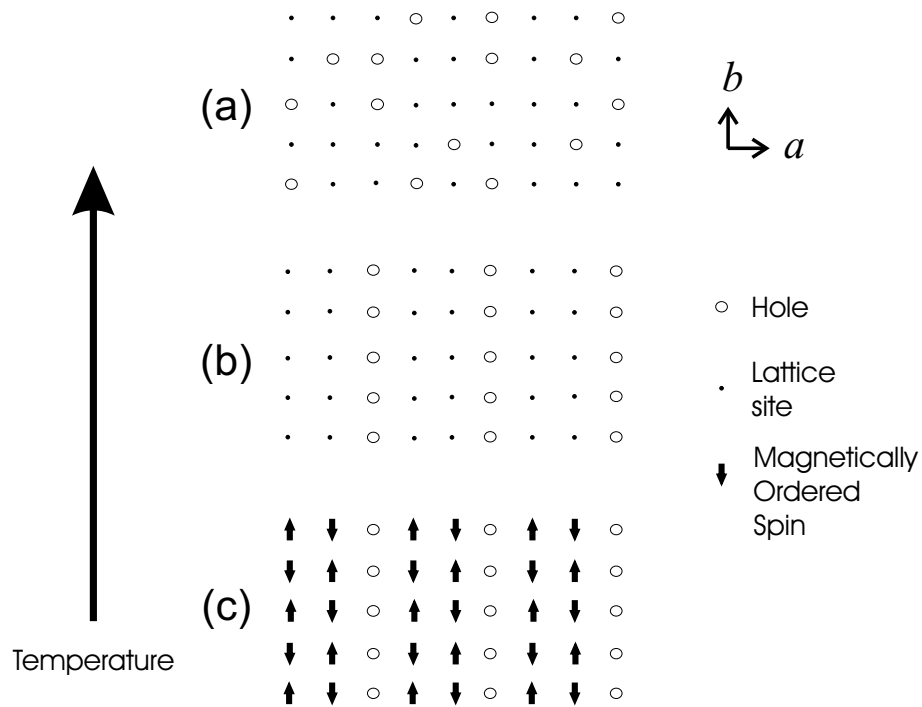
Figure 1.2: The generic temperature evolution of the charge-ordering in doped layered antiferromagnets. The figure shows the metallic sites of an ab plane, represented by circle if a hole resides on the site, a dot when no hole sits on the site, or an arrow representing the ordered spin of the metallic site. On cooling we go from (a) disorder, to (b) periodic lines of ordered holes (charge stripes) and to (c) spin stripe-order between the charge-ordering.

charge-ordered state the spins go up-down-charge-up-..., the after the charge-stripe the spins are flipped 180° compared to the parent material. The charge-stripes act as spin antiphase domain walls.

This is the standard ordering pattern on cooling from disorder, to charge order, that leads to spins ordering between charge order, with the exception of $La_2NiO_{4.125}$ where the spins and holes order cooperatively[7]. Although this pattern is experimentally well characterized, theoretical studies have not been able to reproduce the experimental observations, and to my knowledge there is only preliminary work by Kato that has been able to produce the intermediate ordering of a charge ordered state without spin ordering[8].

To produce this state Kato modelled the system by including fluctuating magnetic order that was found to stabilize the charge ordering.

1.1.1 Theoretical predictions of Charge Order

Charge-ordering was theoretically predicted before it was experimentally confirmed. Different models of doped antiferromagnets proposed by several different researchers all predicted a charge-ordering. A typical starting hamiltonian for such models is a one band Hubbard model;

$$H = t \sum_{\langle i,j \rangle, \sigma} (c_{i\sigma}^{\dagger} c_{j\sigma} + c_{i\sigma} c_{j\sigma}^{\dagger}) + U \sum_{i} n_{i,\uparrow} n_{i,\downarrow} \tag{1.1}$$

where $c_{i\sigma}$ destroys a electron at site i with spin σ, the summation $\langle i, j \rangle, \sigma$ indicates a summation over all nearest neighbour pairs on a square lattice, $n_{i,\sigma} = c_{i\sigma}^{\dagger} c_{i\sigma}$ is the number operator for particles on site i with spin σ. U and t are the on site Coulomb repulsion and the hopping matrix element for nearest neighbours, respectively. The ground state of such a hamiltonian can be shown to be antiferromagnetic at half filling, and every site has one unpaired electron. Charge-ordered states in the cuprates could be described as systems doped away from half filling, which is the case investigated by the theoretical calculations.

In the Hartree-Fock approximation it was found that charge-stripes were predicted for weak[9] and strong[10] short range Coulomb interactions. Short range Coulomb interactions are when the effective range of the Coulomb interaction is significantly reduced by the screening of the electron charge by the polarization of the ions in the material. Long range Coulomb interactions (where there is little screening) were thought to prohibit such ordering, but later theoretical calculations predicted charge-stripe ordering in the presence

of long range Coulomb interactions[11]. Further theoretical models including hybridization of the d-p bonding orbitals[12], or a p-orbital antibonding electron reservoir[13] again predicted charge-stripe ordering.

Theoretical work modelling these systems has come from very different starting points for describing the interactions of such systems. The fact that these different theoretical descriptions all predict charge-stripe order points to the robustness of charge-ordered phases.

1.2 Incommensurate Magnetic Order in $\mathbf{La_{2-x}Sr_xCuO_4}$

The compound $La_{2-x}Sr_xCuO_4$ (LSCO) is isostructural to the first high temperature super-
conductor $La_{2-x}Ba_xCuO_4$ and has an optimum superconducting temperature $T_C \approx 40\,K$
[14]. Early inelastic neutron scattering experiments on superconducting LSCO revealed
the magnetic scattering to be incommensurate with the crystal structure [15]. The dis-
covery by Tranquada *et al.* of a striped spin-charge ordered phase in non-superconducting
$La_{1.48}Nd_{0.4}Sr_{0.12}CuO_4$[3] suggested that the incommensurate magnetic excitations in
LSCO were due to charge-stripe ordering. In figure 1.3 the temperature evolution of
charge ordering in $La_{1.48}Nd_{0.4}Sr_{0.12}CuO_4$ is shown. On cooling below 70 K a structural
transition enables the holes to order into vertical and horizontal charge stripes with a
period of four lattice spacings, as shown in Fig. 1.3 (b). The hole density of these charge
stripes is equivalent to one hole for every two Cu sites. On further cooling below $\sim 50\,K$,
the spins of the Cu^{2+} sites order antiferromagnetically between the charge-stripes, as
shown in Fig. 1.3 (c). The ordering observed in $La_{1.48}Nd_{0.4}Sr_{0.12}CuO_4$ corresponds to a
stable ordering with a hole concentration of 1 hole per 8 Cu sites, i.e. 1/8 doping.

Figure 1.4 shows the generic phase diagram of a hole doped high temperature supercon-
ductor. Two regions that are not thought to be connected with charge-stripe ordering
in high temperature superconductors are the fermi liquid and non-fermi liquid phases.
These phases occur at relatively high doping levels, whereas charge-stripe ordering is be-
lieved to be important only at low doping levels. For low doping levels there exists an
antiferromagnetic phase (AFM) below the Néel temperature T_N. In the case of LSCO
this antiferromagnetic state is lost for approximately x > 0.02. When the sample is suffi-
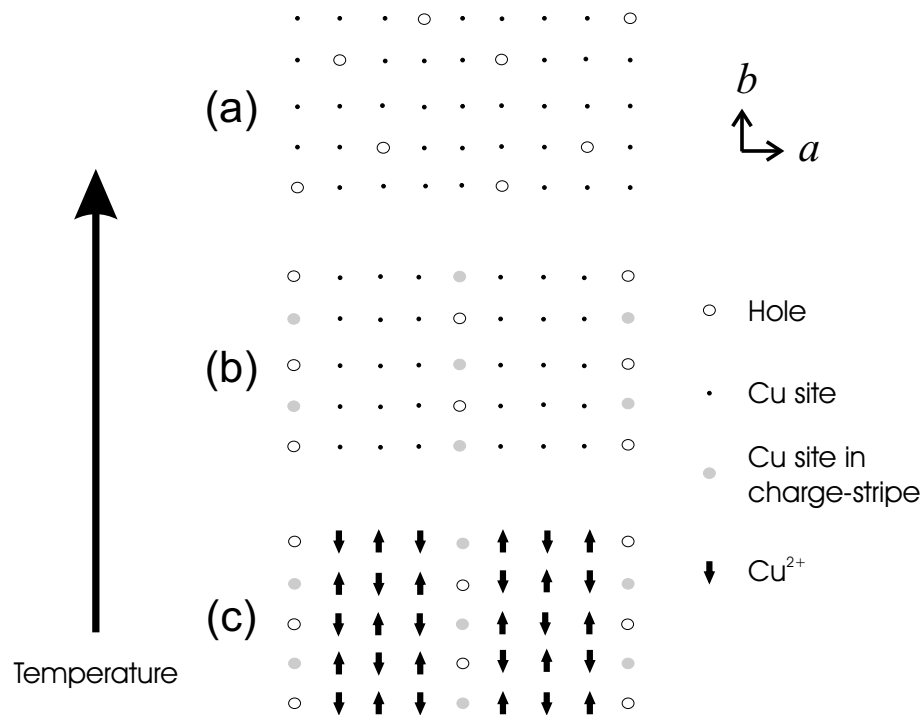
Figure 1.3: The temperature evolution of the charge-ordering in $La_{1.48}Nd_{0.4}Sr_{0.12}CuO_4$. The figure shows the Cu sites of an ab plane, represented by circle if a hole resides on Cu site, a dot when no hole is on the Cu site, or an arrow representing the ordered spin of the Cu^{2+} site. On cooling we go from (a) disorder, to (b) periodic lines of ordered holes (charge stripes) with one hole per two Cu sites and finally to (c) spin stripe-order between the charge-ordering.

ciently doped the ground state of the material is found to superconduct, for $x_c > 0.05$ in the case of LSCO. Increasing the doping level further leads to an increase in the critical superconducting temperature T_C until an optimum value of T_C is reached, after which further increasing the doping level slowly suppresses T_C to $0\,K$. High temperature superconductors are split into three categories by their doping level: optimally doped where the T_C is maximum, underdoped and overdoped.

For doping levels between the antiferromagnetic phase and the superconducting phase there exist two phases: the 'spin glass' and pseudogap phases. The spin glass phase is
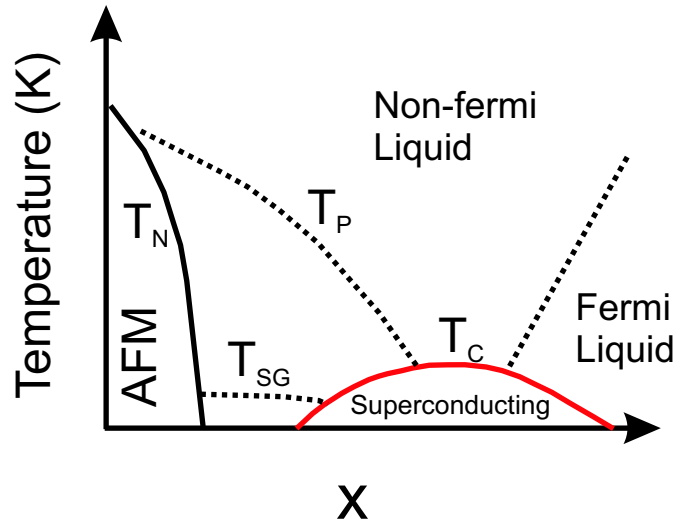
Figure 1.4: The generic temperature versus doping level, x, phase diagram for a hole doped high temperature superconductor. The solid black line indicates the Néel temperature, T_N, for antiferromagnetic order and the red line indicates the critical temperature T_C of superconductivity. The dotted lines indicate the pseudogap temperature T_P and 'spin glass' temperature T_{SG}.

identified in magnetization measurements such as those taken by Chou *et al.*[16]. Zero field cooled (ZFC) and field cooled (FC) magnetization measurements (see chapter 5.1) differ at temperatures below T_{SG}, indicating magnetic irreversibility. The observed magnetic irreversibility is qualitively similar to the magnetic irreversibility observed in spin glasses, and hence this phase is known as the 'spin glass' phase with transition temperature T_{SG}. On cooling below the psuedogap temperature, T_P, several properties of the material undergo a change that is indicative of the opening of an energy gap or a phase transition, although the exact value of T_P depends on the property being examined. This part of the phase diagram is therefore known as the pseudogap phase, a review of which can be found in the article by Battlogg and Varma [17]. Angle-resolved photoemission spectroscopy measurements of the pseudogap reveal that the gap goes to zero in four directions and thus has the same symmetry as the 'd-wave' superconductivity of these materials.

The role played by charge ordering in superconductivity is unclear. Most theorists believe that charge order competes with superconductivity, but some argue that it plays a crucial part in the formation of the superconducting state. A suppression of the superconductivity in 1/8 doped $La_{1.875}Ba_{0.125}CuO_4$[18] could indicate charge-stripe ordering seen in $La_{1.48}Nd_{0.4}Sr_{0.12}CuO_4$ hinders superconductivity. On the other hand, theoretical scenarios of a spin gap and pairing instabilities of stripe electrons have been shown to lead to superconductivity[4].

Inelastic neutron scattering work has revealed incommensurate magnetic excitations[19, 20, 21, 22] occurring for a wide range of doping levels in LSCO. Figure 1.5 shows the observed positions of magnetic scattering for (a) superconducting and (b) spin glass phases of LSCO. In the superconducting phase four magnetic satellites are observed in the low energy excitation spectrum. Approximating the orthorhombic structure of LSCO as tetragonal, the four satellites are evenly displaced away from the antiferromagnetic wavevector at positions $(1/2 \pm \delta,\ 1/2,\ l)$ and $(\ 1/2,\ 1/2 \pm \delta,\ l)$. The doping dependence of these excitations is $\delta = x$, although δ saturates at a value of 1/8 for $x > 1/8$ [19]. If these magnetic excitations have the same origin as the magnetic order in $La_{1.48}Nd_{0.4}Sr_{0.12}CuO_4$, then the excitations indicate charge ordering correlations with a spacing of $1/2\delta$ Cu sites. In the spin glass phase we do not observe the same magnetic excitations as those of the superconducting phase, but instead the magnetic correlations shown in Fig. 1.5 (b) are observed. The magnetic satellites are spaced around the antiferromagnetic wavevector at positions $((1 \pm \sqrt{2}\delta)/2, (1 \pm \sqrt{2}\delta)/2,\ l)$ and $((1 \pm \sqrt{2}\delta)/2, (1 \mp \sqrt{2}\delta)/2,\ l)$[20, 22]. As in the superconducting state $\delta = x$. The correlations in the spin glass phase contain a static component. If these correlations are due to charge-stripes, they indicate charge correlations at $45°$ to the Cu-O bonds with one hole per Cu site, equivalent to a diagonal charge-ordering like

that seen in $La_{2-x}Sr_xNiO_4$. Therefore the ordered state of the spin glass phase of the cuprates would resemble the charge-ordered state of $La_{2-x}Sr_xNiO_4$ (shown in figure 1.6 (c)) but with the charge stripes separated by a larger number of Cu sites. The diagonal correlations of Fig. 1.5 (b) are observed to persist into the superconducting state[22]. Further experimental results from infa-red [23] and Raman [24] measurements support the interpretation of the neutron scattering measurements, indicating charge-stripe correlations with the same orientation.

In the Néel state with $x > 0$, neutron scattering measurements indicate phase separation occurs into an antiferromagnetic phase with $n_h \sim 0$ and a spin glass phase with $n_h \sim 0.02$[21]. This phase separation is probably the first observation of phase separation in lightly doped antiferromagnets, and shows how the incommensurate magnetic correlations of the spin glass phase develop from low doping levels.
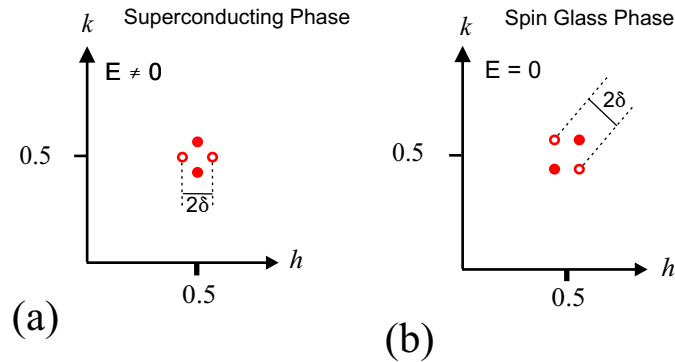
Figure 1.5: (a) The positions of incommensurate magnetic excitations in superconducting LSCO. (b) The positions of incommensurate magnetic Bragg reflections in the spin glass phase of LSCO.

More recently inelastic neutron scattering measurements have now been used to map out the spin wave dispersion in $La_{1.84}Sr_{0.16}CuO_4$ [25], $La_{1.875}Ba_{0.125}CuO_4$ [26] and $YBa_2Cu_3O_{6.6}$ [27]. Theoretical modelling of the structure factor for the magnetic excitations has been able to reproduce the features observed in the inelastic neutron scattering

experiments[28, 29, 30, 31]. The one common feature of these models is that they are based on charge stripes, thus helping to establish stripes as a theoretically well founded phenomena in these materials.

1.3 Charge-Ordering in $La_{2-x}Sr_xNiO_4$

The occurrence of charge-ordering in $La_{2-x}Sr_xNiO_4$ (LSNO) is a well established exper-imental fact. Charge-stripe order has been studied in LSNO by neutron[32, 33, 34, 35, 36, 37, 38, 39] and x-ray[40, 41, 42, 43] diffraction for doping levels in the range 0.135 $\leq x \leq 0.5$. Raman[44, 45], infa-red[45, 46] and optical[47] scattering experiments are all consistent with this ordered picture. As well as being static on the time scale probed by neutrons and photons, the charge stripes are found to be well correlated with correlation lengths in excess of $100\,\text{Å}$ for certain levels of doping[34, 45, 42]. These two proper-ties, static and long-range order, make LSNO an excellent system for studying the basic properties of spin-charge stripes.

Figure 1.6 shows the temperature evolution of charge-ordering in LSNO for $x = 1/3$ doping. In Fig. 1.6(a) I show the high temperatures disordered state, where the holes are randomly distributed in the ab plane. On cooling below the charge order temper-ature, T_{CO}, the holes align themselves into charge-stripes at 45° to the Ni-O bonds, as shown in Fig. 1.6(b). Then at a lower temperature the Ni^{2+} spins align themselves an-tiferromagnetically between the charge-stripes in the manner shown in Fig. 1.6(c), with the charge-stripes acting as spin anti-phase domain walls. The temperature evolution of charge-ordering in other doping levels of LSNO occurs in the same fashion.

Compared to the phase diagram of high temperature superconductors, the phase diagram of LSNO is relatively simple. In figure 1.7 I show the phase diagram of LSNO[34, 38]. For low doping levels there exists an antiferromagnetic (AFM) phase below the Néel temperature T_N. For slightly higher doping levels charge-ordering occurs in a manner similar to Fig. 1.6, on cooling the material charge-orders at T_{CO} and then the spins order
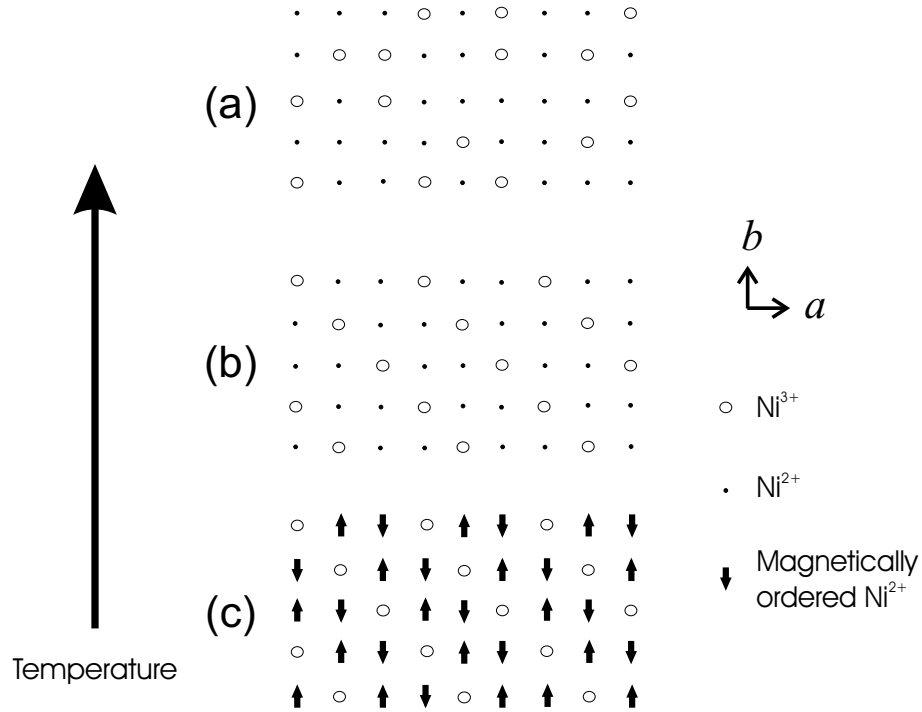
Figure 1.6: The temperature evolution of the charge-ordering in La$_{5/3}$Sr$_{1/3}$NiO$_4$ (LSNO). The figure shows the Ni sites of an ab plane, circles represent holes residing on Ni^{3+} sites, dots represent the Ni^{2+} with unorder spins, while the solid arrows represent the Ni^{2+} spins. In LSNO on cooling, we go from (a) disorder, to (b) periodic lines of ordered holes at 45° to the Ni-O bonds (charge stripes) and to (c) spin stripe-order between the charge-ordering.

at a low temperature T$_{SO}$. On increasing the doping T$_{CO}$ and T$_{SO}$ increase to maximum for $x = 1/3$. Increasing the doping level above $x = 1/3$ causes both T$_{CO}$ and T$_{SO}$ to decease. Although the spin ordering temperature continues to decrease for increasing x, for $x \geq 0.5$ a highly stable checkerboard charge-ordered state emerges, which undergoes a change in character at lower temperatures[38]. A checkerboard charge ordered state is where a hole would reside on every other Ni site in the ab plane, forming a pattern of holes that resembles a checkerboard (see section 1.3.2 for further details on the charge-ordering of $x = 0.5$).
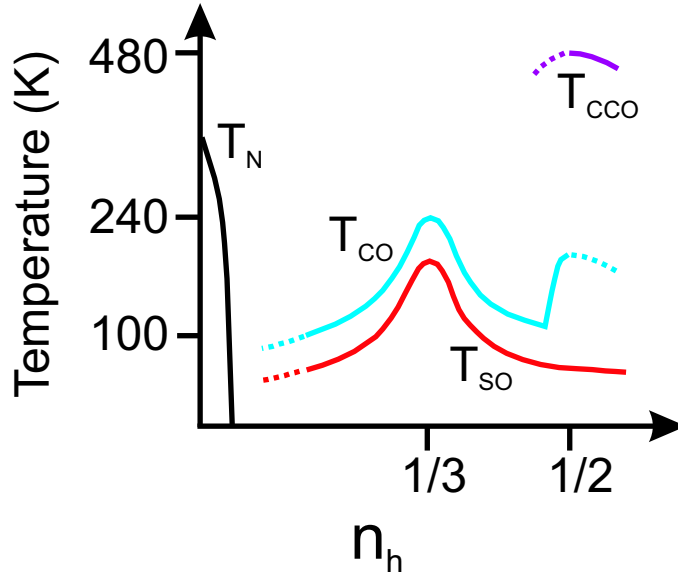
Figure 1.7: The temperature versus doping level, x, phase diagram of hole doped $La_{2-x}Sr_xNiO_4$. The solid black line indicates the Néel temperature, T_N, for antiferromagnetic order, For higher doping levels the solid blue line indicates the charge-ordering temperature, T_{CO}, the solid red line indicates the stripe spin-ordering temperature, T_{SO}, and the solid purple line indicates the checkerboard charge-order temperature, T_{CCO}. The dashed lines indicate areas of the phase diagram which have not yet had their properties ascertained.

In Fig. 1.6(c) I showed the charge-ordered ground state of LSNO with $x = 1/3$, in this material the charge-stripes are evenly spaced by the distance $3 = 1/x$ Ni sites. For other doping levels the charge-stripes are found on average to be approximately $1/x$ Ni sites apart. Figure 1.8 shows the incommensurate charge and spin Bragg reflections produced by charge-ordering in LSNO. The charge-ordering produces small structural distortions in the crystal structure which produce weak Bragg reflections at $(h\pm\varepsilon,\ k\pm\varepsilon,\ l)$ positions in reciprocal space, for $l =$ odd integer. Whereas the magnetic structure of charge-stripe spin order produces Bragg reflections at $(h+1/2\pm\varepsilon/2,\ k+1/2\pm\varepsilon/2,\ l)$ positions in reciprocal space, for $l =$ integer. For both the charge order and spin order ε has the same value with $\varepsilon \approx x$ and ε is known as the incommensurability. In the case of ε being a simple
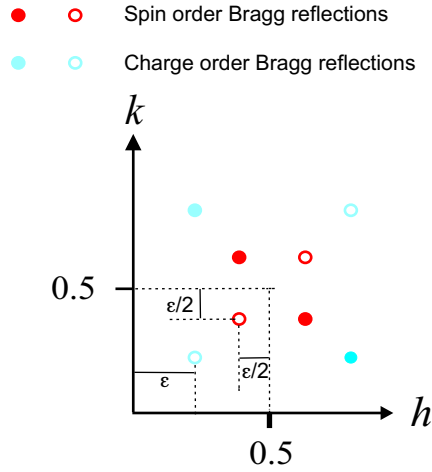
Figure 1.8: The positions of the first-order magnetic and charge order Bragg peaks produced by charge-ordering in LSNO (ignoring l dependence). The Bragg peaks along (110) represent charge-ordering as shown in Fig. 1.6, and the peaks from the equivalent domain in which the magnetic ordering is rotated by 90° relative to that shown in Fig. 1.6 are superimposed.

fraction only $l = $ odd peaks should occur, as the charge-order can stack in a body centred tetragonal arrangement as the charge stripes are spaced a set number of Ni sites apart [48]. This is only true, to a good approximation, for $x = 1/3$[33] and $x = 1/2$ (see chapter 6) doped materials, and as the charge-ordering is spaced commensurately with the crystal structure the charge-ordering is said to be commensurate. For other values of ε the charge-ordering period varies and cannot stack in a body centred tetragonal arrangement, so Bragg reflections for the spin order occur at all integer values of l, see reference [35] for a good example. A similar trend for the charge order Bragg reflections should be expected, but studies of the charge order Bragg reflections have concentrated on the strong $l = $ odd integer reflections[42]. As the charge-ordering period varies it is said to be incommensurate charge-ordering. The system is tetragonal, so ordering also occurs at 90° to this producing a twin that is equally populated[49].

Understanding the variation of the incommensurability away from the relationship $\varepsilon = x$

is critical in understanding many of the properties of LSNO and also indicates why the

$x = 1/3$ doping level is 'special'. Figure 1.9 shows the doping variation ε for the ground

state of LSNO. The only doping level for which $\varepsilon = x$ is the $x = 1/3$ material, for $x < 1/3$

ε is slightly larger than x and for $1/3 < x < 1/2$, ε is slightly smaller than x[36, 39]. For

$x \geq 1/2$ a new charge ordered phase emerges which causes ε to saturate [38].
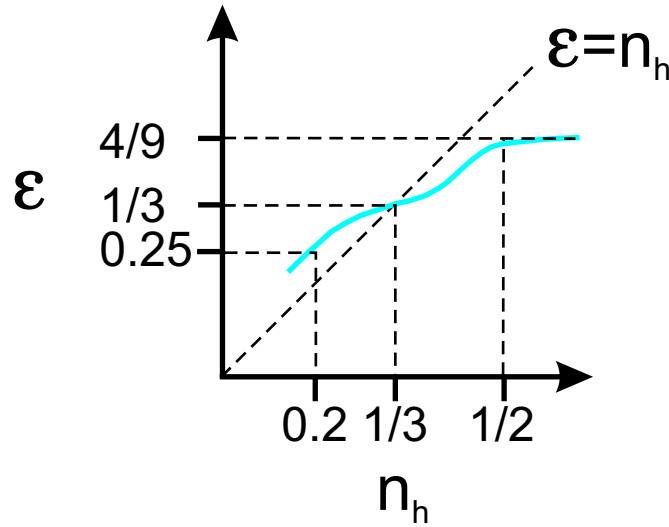
Figure 1.9: The doping variation of the incommensurability of LSNO for the ground state.

Consider the materials with $x < 1/2$. If the hole density in the charge stripes is a constant

1 hole per Ni site, then there are more holes in the charge stripes for $x < 1/3$ than are

doped into the material. To increase the hole density to a level above that caused by

doping, electrons would have to be promoted to the conduction band so that additional

holes are produced, hence the free charge carriers would be electrons. Whereas for $x > 1/3$

from doping there is an excess of holes required for producing charge stripes with 1 hole

per Ni site, so the excess holes would be the free charge carriers. By studying the Hall

coefficient T. Katsufuji *et al.*[50] established that the free charge carriers are electrons for

$x \leq 1/3$ and holes for $x > 1/3$. The reason for this variation away from $\varepsilon = x$ appears to

be that the charge-stripe order in LSNO prefers $\varepsilon = 1/3$ but the spin order prefers $\varepsilon = x$, so ε is closer to $1/3$ than $\varepsilon = x$ for $x \neq 1/3$[36, 42]. As charge-ordering is warmed out of its ground state ε is found to tend towards $\varepsilon = 1/3$ as the spin order melts[36, 39]. This tendency of $\varepsilon \to 1/3$ is more dominant for $x < 1/3$ materials than $x > 1/3$ materials, so the $x = 1/3$ compound can be regarded as a Mott insulator with an electron-hole antisymmetry around this doping level[39].

One common feature of LSNO[51] and LSCO[16] is that both compounds are known to exhibit irreversible magnetic behaviour, with magnetization measurements revealing a ZFC-FC splitting. The irreversible magnetic behaviour of LSNO is not the only glassy feature associated with the stripe ordering. Recent dielectric measurements on $La_{5/3}Sr_{1/3}NiO_4$ also shows electronic glassy behaviour[52]. It has been observed that the charge-ordering transition is not well defined with charge ordering correlations persisting to temperatures well above the ordering temperature[41, 44, 53, 54]. Similarly it has been noted that the magnetic ordering transition is slow and not well defined[33, 37, 55]. Recently neutron diffraction on $x = 1/2$ indicated a magnetic ordering temperature of $80\,\mathrm{K}$[38], but μSR measurements indicated spin ordering that persists upto $180\,\mathrm{K}$[56]. This difference is due to the different length scales probed by these techniques.[1] These results shows that the spins order at $\sim 180\,\mathrm{K}$ but long range order does not occur until $\sim 80\,\mathrm{K}$, showing the magnetic ordering is very slow in establishing itself. It is also at $T_{\mathrm{ICO}} = 180$ K that the charge ordering in the $x = 0.5$ doped material is found to undergo a transition on

---

[1]Neutron diffraction and μSR probe magnetic ordering on different timescales, with neutron scattering probing the order on the shorter timescale, therefore magnetic ordering temperatures are usual measured to be higher from neutron diffraction. In this case we observe magnetic order from μSR measurements at the higher temperature because the muon can probe local order on a length scale smaller than neutron diffraction.

cooling, from commensurate checkerboard ordering into a mixture of incommensurate charge-stripe order and commensurate checkerboard order[38].

1.3.1   Commensurate effects for $x = 1/3$

As already stated, the doping dependence of ε shows a preference for charge-ordering to have a doping level as near as possible to 1/3 [36, 39, 42], with charge-ordering being stablest in the $x = 1/3$ material, for $x < 1/2$ materials. In terms of length scale and temperature stability of the charge-ordering, the stablest charge-stripe ordering also occurs in the $x = 1/3$ material[34, 42]. Add to the stability the fact that charge-ordering can space commensurately with the crystal structure for $x = 1/3$, making the $x = 1/3$ doping level an attractive doping level to study, extensive studies of this doping level have been carried out.

Studies of certain properties of LSNO have revealed commensurate effects that only occur for $x = 1/3$. The properties that have been observed to show commensurate effects for $x = 1/3$ are:

1) Measurements of the specific heat by Ramirez *et al.*[57] in the $x = 1/3$ revealed an increase in entropy on charge-ordering not seen for other doping levels[58].

2) Ramirez *et al.* also showed a sound velocity anomaly on charge-ordering that is specific to the $x = 1/3$[57].

3) A neutron diffraction study between 11 and 300 K on $x = 0.275$ and 1/3 single crystals observed only a spin reorientation in the $x = 1/3$ material on cooling below 50 K[35].

The commensurately ordered $x = 1/3$ shows effects that are specific to that doping level due to the commensurate pinning of the charges to the lattice.

Charge order in LSNO prefers the commensurate charge order of the $x = 1/3$, and this commensurate ordering shows unique features. It is important when studying properties of charge-ordering in LSNO to determine if effects are due to commensurate charge order, or whether any effect is enhanced by commensurate charge order.

1.3.2   Checkerboard Charge-ordering for $x = 1/2$

At half doping, systems with dominant Coulomb repulsions are expected to exhibit a stable Wigner crystal state, where the charge carriers minimize Coulomb repulsion by maximizing their displacement. In the case of a two-dimensional square lattice at half doping this takes the particularly simple form of a checkerboard pattern, where every other site is part of the charge-ordered state. This type of charge order has been observed in the isostructural layered perovskites $La_{3/2}Sr_{1/2}NiO_4$[59], $La_{1/2}Sr_{3/2}MnO_4$[60], and $La_{3/2}Sr_{1/2}CoO_4$[61]. In figure 8.1 (a) I show the ideal half doped charge-ordered state of $La_{3/2}Sr_{1/2}NiO_4$, where the Ni^{2+} carrying spins $S = 1$ order antiferromagnetically between the checkerboard charge-ordered Ni^{3+} sites. In this case it is assumed that the $S = 1/2$ spins of the Ni^{3+} sites do not order, which is different to the observed ordering of $La_{1/2}Sr_{3/2}MnO_4$[60].

Interestingly, checkerboard charge order has also recently been observed at doping levels well below 0.5 in $Bi_2Sr_2CaCu_2O_{8+\delta}$[62], and $Ca_{2-x}Na_xCuO_2Cl_2$[63] with a periodicity of 4 Cu atoms. Theoretical modelling of this charge-ordered state has been carried out[64, 65], based on connecting this checkerboard charge-ordered state with incommensurate field induced magnetic order with a periodicity of 8 Cu atoms that has been observed in $La_{2-x}Sr_xCuO_4$ for $x = 0.163$[66]. Further experimental studies of simple systems with

checkerboard charge order could help explain the formation of electronically-ordered states in more complex systems.
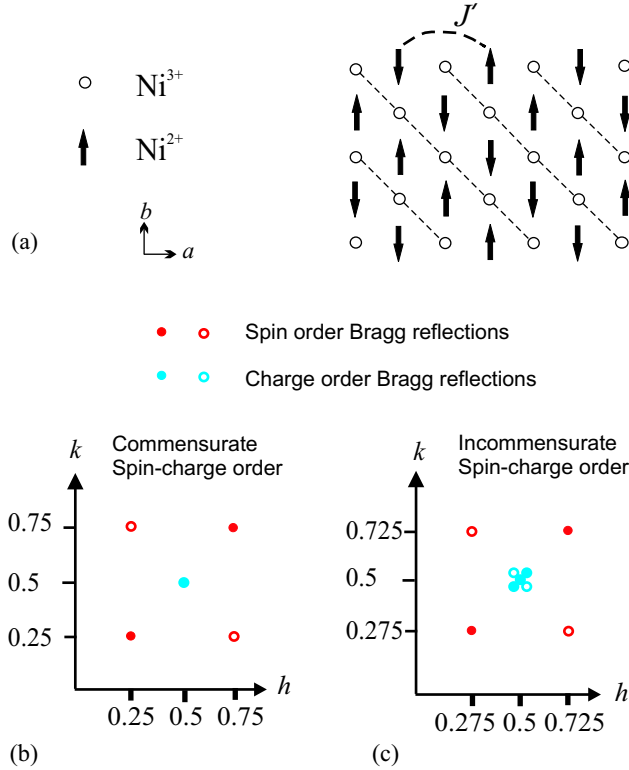
Figure 1.10: (Color online)(a) Ideal checkerboard spin–charge ordering in a NiO_2 square lattice. Circles represent Ni^{3+} holes, and solid arrows represent spins on Ni^{2+} sites. The broken lines are included to highlight that the spin pattern breaks the 2D symmetry of the checkerboard charge ordering. J' is the exchange coupling parameter of the Ni^{2+} spins across the Ni^{3+} site. This commensurate ordering is not realized in practise in $La_{3/2}Sr_{1/2}NiO_4$. (b) Diagram of part of the (h, k) plane in 2D reciprocal space showing the positions of the first-order magnetic and charge order Bragg peaks for the ideal checkerboard ordering represented in (a). The peaks from the equivalent domain in which the magnetic ordering is rotated by 90 deg relative to that in (a) are superimposed. (c) The same diagram as (b) except with the magnetic and charge order Bragg peaks observed in the incommensurate ordered phase of $La_{3/2}Sr_{1/2}NiO_4$. For simplicity we neglect the variation in the peak positions in the direction perpendicular to the NiO_2 plane.

The checkerboard charge-ordered state of $La_{3/2}Sr_{1/2}NiO_4$ was first discovered in electron

diffraction measurements by Chen *et al.*[59]. Recently a neutron diffraction study of this $x = 0.5$ LSNO material by Kajimoto *et al.* revealed a different ground state to that of the ideal checkerboard state shown in Fig. 1.10(a)[38]. The positions in reciprocal space of the corresponding Bragg peaks for the ideal checkerboard-ordered state are shown in Fig. 1.10(b). Peaks from the charge order have two-dimensional wave vectors (in units of $2\pi/a$) $(h + \frac{1}{2}, k + \frac{1}{2})$, where h and k are integers. The lack of l dependence of the charge-ordered Bragg peaks indicates a highly 2-dimensional nature of the charge-ordering. The magnetic order has double the periodicity of the charge order, so peaks from the magnetic order appear at $(h + \frac{1}{2}, k + \frac{1}{2}, l) \pm (\frac{1}{4}, \frac{1}{4})$ for $l =$ odd integer. Rotation of the ordering pattern by 90 deg generates an equivalent magnetic structure, this time with magnetic peaks at $(h + \frac{1}{2}, k + \frac{1}{2}, l) \pm (\frac{1}{4}, -\frac{1}{4})$ for $l =$ even integer. In the absence of a symmetry-breaking interaction we expect an equal population of these two domains, so the pattern of Bragg peaks will be a superposition, as shown in Fig. 1.10(b).

The measurements of Kajimoto *et al.* revealed Bragg peaks at very different positions in reciprocal space to those shown in Fig. 1.10(b). This means the actual spin–charge ordered phase of $La_{3/2}Sr_{1/2}NiO_4$ observed below T_{ICO} does not conform to the ideal structure shown in Fig. 1.10(a)[38]. Instead, in the ground state the magnetic Bragg peaks are found at the incommensurate positions $(h + \frac{1}{2}, k + \frac{1}{2}, l) \pm (\epsilon/2, \epsilon/2, 0)$ with l an odd integer, and $(h + \frac{1}{2}, k + \frac{1}{2}, l) \pm (\epsilon/2, -\epsilon/2, 0)$ with l an even integer, where $\epsilon \approx 0.44$ [38, 34]. New charge-order satellite peaks appear at $(h \pm \epsilon, k \pm \epsilon)$ in addition to the checkerboard charge order peak at $(h + \frac{1}{2}, k + \frac{1}{2})$, with little or no l dependence[38]. The significance of observing spin and charge-order peaks with $\epsilon \approx 0.44$ is that this incommensurate order retains a part 1-dimensional stripe-ordering, along with the 2-dimensional commensurate checkerboard charge-ordering. The full set of 2D magnetic

and charge order wavevectors for the incommensurate phase of $La_{3/2}Sr_{1/2}NiO_4$, including those for the 90° domain, are shown in Fig. 1.10(c). This charge-order picture has been determined to be consistent with observed symmetries of Raman, infa-red and optical measurements[67]. For $La_{3/2}Sr_{1/2}CoO_4$[61] the charge-order picture was observed to the same as $La_{3/2}Sr_{1/2}NiO_4$ but with $\epsilon \approx 0.49$, which is closer to the perfect checkerboard order of $\epsilon = 0.5$.

Kajimoto *et al.*[38] suggested that two types of charge order coexist in the incommensurate phase, one part of the system being charge-ordered in a checkerboard pattern and the other part adopting an incommensurate, stripe-like, spin-charge order. These authors developed models for the latter component based on the introduction of diagonal discommensurations in the ideal checkerboard spin-charge structure of Fig. 1.10(a). As pointed out by Kajimoto *et al.*, the stability of the incommensurate structure is probably the result of a competition between magnetic and electrostatic energy. The strong superexchange interaction favours having antiparallel spins on nearest neighbour Ni sites, whereas the Coulomb interaction tries to have a uniform charge density.

A theoretical model of the ideal charge-ordered state at $x = 0.5$ with antiferromagnetic ordering of the Ni^{3+} sites predicted the occurrence of orbital ordering in this material[68]. However, the absence of static magnetic order on the Ni^{3+} sites and the occurrence of an incommensurate magnetic ground state of the Ni^{2+} sites could have implications for this prediction.

1.3.3 Centring of Charge order in LSNO

In LSNO compounds it has yet to be uniquely determined, whether the charge-order is centred on the Ni site or on the oxygen site, respectively known as site and bond centring. Transmission electron microscope measurements on the $x = 0.275$ material revealed the charge-ordering to be preferentially residing on the Ni sites on the surface of the material[69]. NMR measurements on $\sim 1/3$ doped $La_2NiO_{4.17}$ reveal two different Ni valencies, consistent with site centred charge order[70]. While Curie-Weiss fits of magnetization measurements in the paramagnetic state for $0.2 \leq x \leq 0.55$ are again consistent with site centred charge order[71]. Studies of $La_2NiO_{4.13}$ in magnetic field supported bond centring above the spin temperature that ordering transforming into site centring below the spin ordering temperature[72]. However, X-ray absorption spectroscopy measurements on LSNO with $0 \leq x \leq 1.15$ revealed the holes to be distributed equally over the in plane and out of plane O 2p orbitals[73].
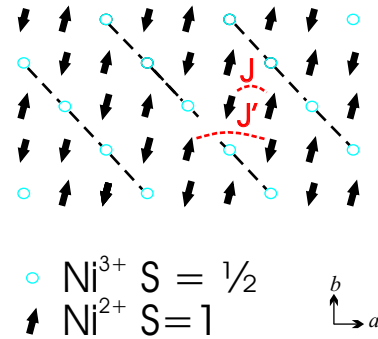
Figure 1.11: Model of the stripe order found in a ab plane of $La_{5/3}Sr_{1/3}NiO_4$. Circles represent holes residing on Ni^{3+} sites and the solid arrows represent the ordered Ni^{2+} spins. With the intrastripe and interstripe exchange interactions J, J' of nearest neighbour Ni spins are indicated.

Inelastic neutron scattering measurements of the spin wave dispersion have been carried out on single crystals of $x = 1/3$[49] and 0.31[74]. From these measurements the strengths

of magnetic interactions can be determined by modelling the structure factor of the system and comparing it to the measured structure factor of the system. In the work on the $x = 1/3$ the magnetic interactions were modelled on a spin-only model having site centred charge order. The model included nearest neighbour exchange interactions of spins within the AFM region, J, and spins across the charge stripe, J', plus an out-of-plane anisotropy. Figure 1.11 shows the Ni sites of an ab plane of the $x = 1/3$ doped material indicating the exchange interactions of nearest neighbour spins J and J'. The results of fitting this model to the observed magnon dispersion indicated values of $J = 15 \pm 1.5$ meV and $J' = 7.5 \pm 1.5$ meV. Theoretical modelling of the spin wave dispersion in charge ordered materials for a spin only model and a wider range of doping levels has also been carried out[75, 76]. Carlson *et al.* modelled the spin wave dispersion using a spin only model for several different commensurate charge ordered states, including $x = 1/3$, for both bond and site centred stripes[76]. Their calculation showed for $x = 1/3$ there was one dispersion mode for site centred charge ordering but two modes for bond centred charge ordering. For $J'/J = 0.5$ the second optic dispersion mode is close in energy to the acoustic mode and should have been observed in the measured spin wave dispersion on LSNO for $x \sim 1/3$ [49, 74]. No second mode was observed in the experiment, supporting a structure of site centred charge-ordering.

As the experimental evidence supports site centred charge ordering where the charge stripes reside on Ni sites, over bond centred charge-ordering where the charge stripes reside on O sites, I have assumed site centred charge-ordering when interpreting the results in this thesis.

1.4   Scope of this Thesis

The purpose of the experimental work of this thesis was to contribute to the existing knowledge of charge-ordering in doped antiferromagnets.

In this work the aim was to study the doping dependence of the magnetic order and magnetic excitations in $La_{2-x}Sr_xNiO_4$ for $0 \leq x \leq 0.5$, using magnetization and diffraction measurements to study the doping dependence of the ordering, while using inelastic neutron scattering to study the doping dependence of the magnetic excitations.

The study of the magnetic order is undertaken to improve the existing knowledge of the different orderings and the doping evolution of the charge-ordered state. It is hoped that from this work the effects of commensurate ordering and charge stability can be determined.

Measurements of the magnetic excitation spectrum are carried out to determine the effects of commensurate/incommensurate charge-ordering and the effect of two dimensional checkerboard charge-ordering. It is hoped from this work that both the interaction strengths of magnetic ordering and the magnetic state of the spins of the charge stripes can be determined.

Chapter 2

Magnetization measurements

Magnetization measurements provide information on the bulk magnetism of samples. By measuring the bulk magnetization of a sample, temperatures at which transitions occur can be identified. Combining magnetization measurements with a technique such as neutron scattering provides a way to characterize the ordered state of materials.

2.1   SQUID magnetometer

Magnetization measurements were carried out by the D.C. method using a Superconducting QUantum Interference Device (SQUID). The SQUID magnetometer used in this work was a Quantum Design model MPMSXL. The instrument has a sample environment of a cryostat capable of reaching a base temperature just below $2\,\mathrm{K}$ and a superconducting magnet that can produce a vertical field of up to $7\,\mathrm{T}$ in magnitude. Operation and data acquisition are controlled by computer.

To measure the magnetization of a sample a field must be applied to the sample to induce a net moment in the sample. The net moment induced in the sample induces a current

in the detector coils which are made from superconducting wire, the detector coils are connected to the SQUID and the output voltage of the SQUID is directly proportional to the current induced by the magnetization of the sample. Hence the SQUID acts as current-to-voltage convertor and magnetization is measured from the induced voltage. In figure 2.1 (a) the setup of the detection coils is shown. There are coils at the top and bottom that are wound anti-clockwise and two central coils wound clockwise. This arrangement of detection coils means that variations of the magnetic field induce opposing current in the clockwise and anti-clockwise coils which cancel each other out, thus minimizing noise in the detection circuit. The magnetization produced by the sample would not be uniform across the sample space, with the detection coils measuring the local changes in the magnetic flux density, in this way a current is induced in the detection coils by the sample's net magnetization.

Figure 2.1 (b) displays the standard way in which the samples were mounted for these measurements. The sample is mounted inside a plastic capsule, held in the central position by use of cotton wool[1]. Using plastic tape this capsule was then thickened so that the sample could be securely mounted in a central position in a plastic drinking straw. It is important for mounting purposes that the sample is mounted symmetrically in the vertical direction, as unsymmetrical sample mounting can induce a diamagnetic signal in the detection coils.

Two techniques were employed to measure the magnetization of the samples studied, the D.C. technique and the Reciprocating Sample Option (RSO) technique. In the D.C.

---

[1]Cotton wool is known to produce a small diamagnetic signal when placed in a magnetic field. In this work we measured the temperature variation of the standard mount and found there to be no temperature variation in this diamagnetic signal over the temperature range studied here.
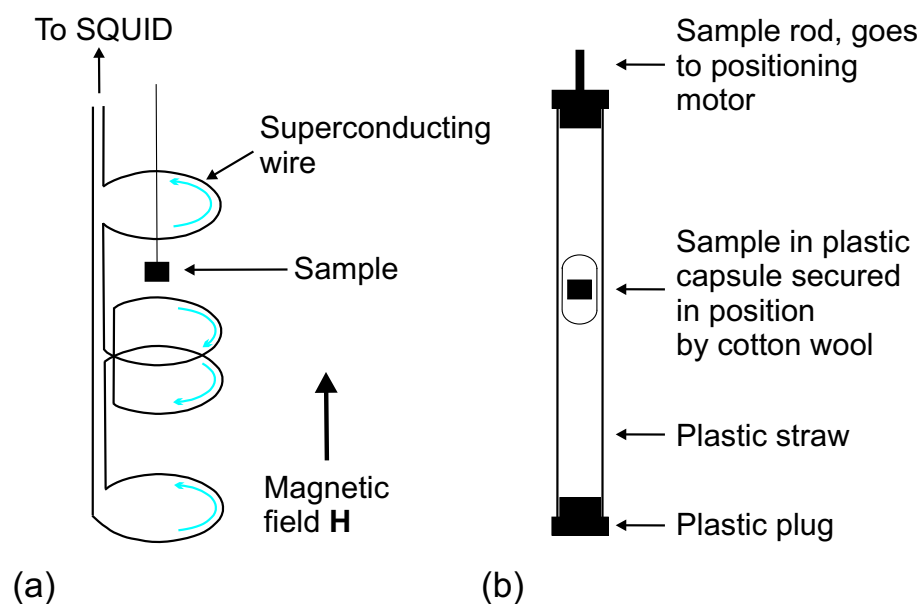
Figure 2.1: (a) The detection coils of the SQUID. (b) Sample mount employed in magnetization measurements.

technique the sample is moved through the detection coils in a point by point manner, with the magnetization induced in the detector coils being recorded for the position of each point. In the RSO technique the sample is oscillated about the central detection coils and the magnetization is recorded as a function of the sample position. In both techniques the curve produced by measuring the voltage induced across the SQUID as a function of sample position is fitted to a theoretical curve, and the amplitude of this curve is taken to be the sample magnetization. Figure 2.2 shows a curve that would typically be measured by the SQUID for both D.C. and RSO techniques.

For the majority of this work the RSO technique was used in preference to the D.C. technique, this is because of the greater sensitivity of the RSO technique. The greater sensitivity of the RSO technique is due to the frequency at which the sample is oscillated, for RSO measurements only magnetization varying with the frequency of the sample oscillation will be recorded, a measuring technique known as phase locking. This removes
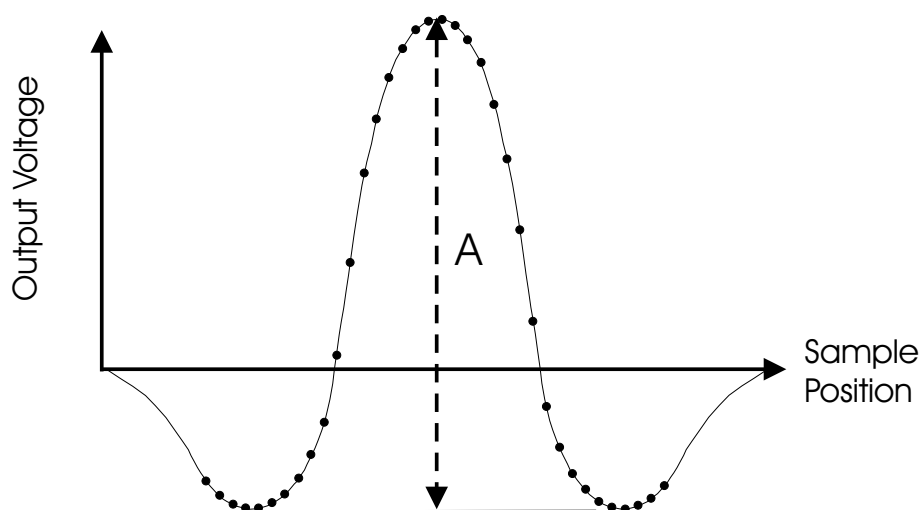
Figure 2.2: A typical output produced by moving the sample position through the detector coils. The curve mapped out by the sample passing through the detection coils is shown by the points, and the line represents the theoretical response curve of the detection coils. The amplitude of the central peak of this curve, A, is taken to be the magnetization of the sample.

additional magnetization detected by the detection coils that does not come from the sample and the sample mount, any additional magnetization would be detected by the D.C. technique. Some work was carried out using the D.C. technique because of sample mounting considerations. When using the SQUID's rotating mount to align the sample for magnetization measurements, instrumental design restricts the measuring technique to the D.C. method.

The results of the magnetization measurements in this work will be expressed in $EMUmol^{-1}$. To obtain the magnetization in $EMUmol^{-1}$ the measured magnetization is divided by the sample mass and then multiplied by the molar mass.

2.2   SQUID rotating mount

The physics of the materials studied in this work is highly two dimensional in the *ab* plane of the crystals. Important information can be yielded by studying the variation of magnetism parallel to and perpendicular to the *ab* plane of the crystals. When studying the magnetization perpendicular to the *ab* plane, misalignment of the crystal can lead to significant contribution to the magnetization from the *ab* plane. To minimize the contribution of the magnetization from the *ab* plane when measuring perpendicular to the *ab* plane a rotating plate sample mount can be utilized to align the sample.
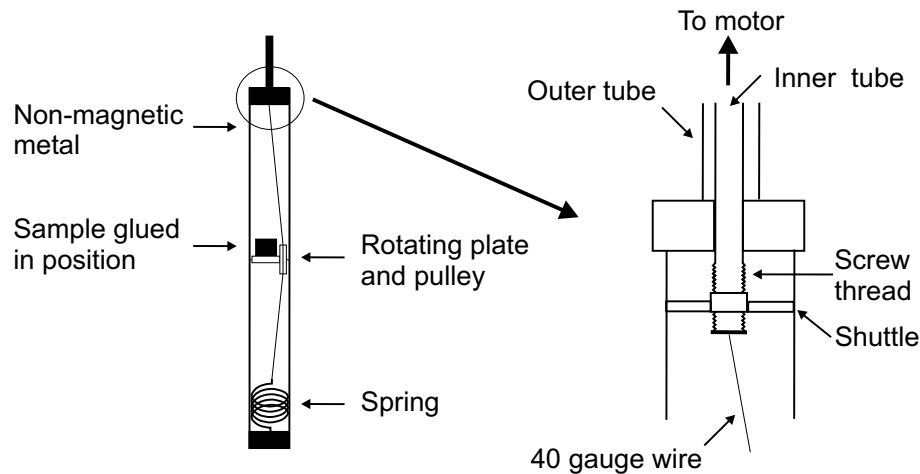
Figure 2.3: A diagram of the rotating mount. The right hand diagram is an enlargement of the encircled area of the diagram on the left hand side.

Figure 2.3 shows the design that is used for a rotating mount for the SQUID. A sample of known orientation is glued with non-magnetic varnish to the flat rotating plate. This plate is attached to a pulley, a thread attached to this pulley is then moved by means of a motor so that the pulley rotates and turns the plate and the sample. Using the anisotropy of the sample's magnetization the sample can be aligned in the desired orientation around this axis of rotation.

There is a significant background from the rotating plate mount, that is history dependent. All data taken when using the rotating mount have had this background subtracted. The size of this background amounts to $\geq 10\%$ of the measured signal.

Chapter 3

Neutron Scattering

Neutron scattering is a powerful technique that is widely used for studying systems of interest in condensed matter physics. From diffraction studies we can obtain the crystallographic and magnetic structure of materials, while inelastic neutron scattering can be used to study the excitations of materials. The ability to probe the order and dynamics of materials plays a key part in understanding the underlying physics.

X-ray scattering is a complementary technique to neutron scattering. X-rays strongly interact with materials and only penetrate millimetres of the surface of a sample, whereas neutrons interact weakly with materials, penetrating centimetres into the material enabling the study of the bulk of a sample. A neutron has an intrinsic magnetic moment that can interact with the magnetic moment of unpaired electrons in materials, in this way the magnetic order and magnetic excitations can be probed by neutron scattering. Polarized neutron scattering can be used to study both magnetic diffraction and excitations to determine the orientation of the magnetic order and the dynamic magnetic excitations in a material. In this way polarized neutron scattering provides valuable information on the system being studied. The use of neutron scattering to study the actual charge-ordering relies on the neutron scattering off the distortions of the crystal lattice

caused by the charge-ordering, which produces weak Bragg reflections. As x-rays scatter off the electrons of a material, x-ray scattering is a far more powerful technique to use when studying the charge-ordering. In fact P. Hatton *et al.* have carried an extensive study of the charge order in $La_{2-x}Sr_xNiO_{4+\delta}$ using many of the same crystals as employed here[41, 42, 43]. In this work we studied the magnetism of charge-ordered $La_{2-x}Sr_xNiO_4$, therefore we chose to use neutron scattering instead of x-ray scattering.

3.1   Neutron Sources

There are two methods employed for producing neutrons for scattering experiments; using nuclear reactors or using spallation sources. Nuclear reactors can be designed to produce an excess of neutrons not required to sustain the nuclear fission reaction, and these additional neutrons provide a constant flux of neutrons that can be used to perform neutron scattering experiments. Spallation, on the other hand, uses a pulse of highly energetic protons from a synchrotron and smashes these into a heavy metal target. The nuclei of the heavy metal target are split into smaller lighter nuclei, and excess neutrons are released. The excess neutrons are a result of the higher ratio of neutrons to protons in heavy metal nuclei compared to the ratio in the smaller product nuclei.

3.2   Neutron Scattering Theory

The formal theory of neutron scattering requires the application of quantum mechanics. Here I will cover the key concepts and quote the main formulae relevant to analysis of experimental results. A rigorous derivation of these formulae and the concepts of neutron scattering can be found in the texts by Lovesey[77] and Squires[78].

3.2.1   Neutron Scattering Cross Section

An important concept in neutron scattering is the scattering cross section. The total scattering cross section represents the probability that a neutron will be scattered. A mathematical definition of the total cross section is given by

$$\sigma_{tot} = \frac{(\text{total number of neutrons scattered per unit time})}{\Phi} \tag{3.1}$$

where Φ is the flux of the incident neutrons, the number of incident neutrons per unit time and unit area. The differential cross section is the probability a neutron will be scattered within a given solid angle, and can be defined as

$$\frac{\mathrm{d}\sigma}{\mathrm{d}\Omega} = \frac{\begin{array}{c}(\text{total number of neutrons scattered per unit}\\ \text{time into the solid angle } \mathrm{d}\Omega \text{ in the direction } \theta, \phi)\end{array}}{\Phi\,\mathrm{d}\Omega} \tag{3.2}$$

where θ, ϕ are the polar angles, with the polar axis taken as the direction of the incident neutron beam. The double differential cross section is the probability that a neutron will be scattered within a given solid angle and have an energy within a certain range. This

can be expressed as

$$\frac{\mathrm{d}\sigma^2}{\mathrm{d}\Omega\mathrm{d}E} = \frac{\begin{pmatrix} \text{total number of neutrons scattered per unit} \\ \text{time into the solid angle } \mathrm{d}\Omega \text{ in the direction} \\ \theta, \phi \text{ with energy between } E \text{ and } E + \mathrm{d}E \end{pmatrix}}{\Phi\,\mathrm{d}\Omega\,\mathrm{d}E} \tag{3.3}$$

All three of these are loosely defined as the 'scattering cross section'. The cross sections for nuclear, magnetic, inelastic and polarized neutron scattering can be obtained from first principles using quantum mechanics. This requires the knowledge of the initial and final quantum states of the system and the knowledge of the transition probability between these two states. In the following sections I will quote the results for these cross sections.

3.2.2 Nuclear Elastic Scattering Cross Section

The neutron scattering cross section for a nuclear Bragg reflection occurring with wavevector $\mathbf{Q}$ is

$$\frac{\mathrm{d}\sigma}{\mathrm{d}\Omega} = N\frac{(2\pi)^3}{V_0}|F_N(\mathbf{Q})|^2 \tag{3.4}$$

where N is the number of unit cells of the crystal, V_0 the volume of the unit cell and $F_N(\mathbf{Q})$ is the nuclear unit cell structure factor, given by

$$F_N(\mathbf{Q}) = \sum_j \bar{b}_j \exp(i\mathbf{Q}.\mathbf{r_j}) \exp(-W_j(\mathbf{Q}, T)) \tag{3.5}$$

The summation over j runs over all the individual atoms in the unit cell, $\bar{b}_j$ is the neutron scattering length of the jth atom in the the unit cell summed over all the isotopes of atom j, and $\mathbf{r_j}$ is the location of the j th atom in the unit cell. The term $\exp(-W_j(\mathbf{Q}, T))$ is the Debye-Waller factor of the the j th atom, this accounts for the displacement of the atoms from their nominal positions due to thermal motion.

For the jth atom in a cubic unit cell the Debye-Waller factor is $e^{(-W_j(\mathbf{Q},T))}$ where

$$W_j(\mathbf{Q}, T) = \frac{1}{2} \left\langle (\mathbf{Q}.\mathbf{u_j}(\mathbf{T}))^2 \right\rangle \tag{3.6}$$

where $\mathbf{u_j}(\mathbf{T})$ is the thermal displacement of the jth atom from its lattice site due to the motion of the atom.

3.2.3   Magnetic Elastic Scattering Cross Section

For unpolarized neutron scattering the magnetic scattering cross section for a magnetic Bragg reflection occurring with wavevector $\mathbf{Q}$ is

$$\frac{\mathrm{d}\sigma}{\mathrm{d}\Omega} = N_m \frac{(2\pi)^3}{V_{0m}} \left(\frac{\gamma r_0}{2} \right)^2 \sum_{\alpha\beta} \left\langle \left(\delta_{\alpha,\beta} - \hat{Q}_\alpha \hat{Q}_\beta \right) F^\alpha(\mathbf{Q}) F^{\beta*}(\mathbf{Q}) \right\rangle \tag{3.7}$$

where N_m is the number of magnetic unit cells in the crystal, V_{0m} is the volume of the magnetic unit cell, $\gamma = 1.91$ is the gyromagnetic ratio, $r_0 = 2.8 \times 10^{-15}\,\mathrm{m}$ is the classical electron radius. The summation over α, β is the summation over the cartesian co-ordinates x, y, z, with δ being the Kronecker delta, * represents the complex conjugate and $\hat{Q}_\alpha, F^\alpha(\mathbf{Q})$ are the alpha components of the scattering wavevector and the magnetic unit cell structure factor respectively. The components of the magnetic unit cell structure factor are given by

$$F^\alpha(\mathbf{Q}) = \sum_j \mu_j^\alpha f_j^\alpha(\mathbf{Q}) exp(i\mathbf{Q}.\mathbf{r_j}) \exp(-W_j(\mathbf{Q}, T)) \tag{3.8}$$

where the summation j runs over all the magnetic atoms in the unit cell, μ_j^α is the α component of the magnetic moment of the jth atom, and $f_j^\alpha(\mathbf{Q})$ is the α component of the magnetic form factor of the jth atom.

3.2.4   Magnetic Inelastic Scattering Cross Section

In the dipole approximation for unpolarized neutron scattering the inelastic magnetic scattering cross section for a magnetic ion is

$$\frac{\mathrm{d}\sigma^2}{\mathrm{d}\Omega\mathrm{d}E} = \left(\frac{\gamma r_0}{2}\right)^2 f^2(\mathbf{Q}) \ \exp(-2W(\mathbf{Q},T))\frac{k_i}{k_f}S(\mathbf{Q},\omega) \tag{3.9}$$

where k_f and k_i are the initial and final wavevectors of the scattered neutron and $\mathbf{Q}$ is the scattering wavevector. In the case of localised excitations with a sharply defined energy difference the response function is

$$S(\mathbf{Q},\omega) = \sum_{ij} \rho_i |\langle j|\hat{\mu}_\perp|i\rangle|^2 \delta(E_i - E_j - \hbar\omega) \tag{3.10}$$

where $|i\rangle$, $|j\rangle$ are the initial and final eigenfunctions of the system with eigenvalues E_i, E_j, $\hat{\mu}_\perp$ is the magnetic moment operator perpendicular to the scattering wavevector $\mathbf{Q}$, $\hbar\omega$ is the energy lost by the neutron to the system, and ρ_i is the thermal population factor of the initial state. The thermal population factor ρ_i is given by

$$\rho_i = \frac{e^{(-E_i/k_B T)}}{Z} = \frac{e^{(-E_i/k_B T)}}{\sum_i g_i e^{(-E_i/k_B T)}} \tag{3.11}$$

where g_i is the degeneracy of the state with energy E_i, and Z is known as the partition function.

3.3   Polarized Neutron Scattering

In the case of polarized neutron scattering the spin state of the neutron must also be taken into account. Here I will quote the most important results for polarized neutron scattering. This is covered in far greater detail in the paper by Moon, Riste and Koehler[79], as well as the texts by Lovesey[77] and Squires[78].

3.3.1   Polarized Neutron Scattering Cross Section

A neutron is a spin one-half fermion. In a magnetic field the neutron has its spin either parallel (up) or antiparallel (down) to the field. Hence, when a field is applied on the sample a neutron can be scattered by a sample into either an up or down spin state. This gives four possible spin scattering processes

$$
\begin{aligned}
| \uparrow \, \rangle &\rightarrow | \uparrow \, \rangle \\
| \downarrow \, \rangle &\rightarrow | \downarrow \, \rangle \\
| \uparrow \, \rangle &\rightarrow | \downarrow \, \rangle \\
| \downarrow \, \rangle &\rightarrow | \uparrow \, \rangle
\end{aligned}
\tag{3.12}
$$

where $| \uparrow \, \rangle$, $| \downarrow \, \rangle$ represent the two spin eigenfunctions of the neutron. In the first two scattering processes the neutron's spin state remains unchanged, whereas in the last two scattering processes the neutrons spin state is flipped, hence these two categories of spin interactions are commonly known as non-spin flip (NSF) and spin flip (SF) scattering processes. In longitudinal polarized neutron scattering the neutrons spin in maintained in either the up or down spin state by an application of a field for the entire scattering process. For longitudinal polarized neutron scattering the cross section is the sum of the cross section for each of these four scattering processes.

A general expression for the scattering cross section for polarized neutron scattering is

$$\frac{\mathrm{d}\sigma}{\mathrm{d}\Omega\mathrm{d}E} \propto |\langle k_f S_f\,|V|\,k_i S_i\rangle|^2 \tag{3.13}$$

where V is the scattering potential, k_i, k_f are the initial and final wavevectors of the neutron, and S_i, S_f are the initial and final spin states of the neutron. The scattering potential contains both the interaction potentials for nuclear and magnetic scattering.

Consider the case of non-magnetic coherent nuclear scattering. The matrix elements in equation 3.13 can be written as

$$\left\langle S_f\,\left|V_N^{Coh}(\mathbf{Q})\right|\,S_i\right\rangle = V_N^{Coh}(\mathbf{Q})\,\langle S_f|S_i\rangle \tag{3.14}$$

where $V_N^{Coh}(\mathbf{Q})$ is the coherent nuclear scattering potential and the scattering wavevector $\mathbf{Q}$ is

$$\mathbf{Q} = \mathbf{k_i} - \mathbf{k_f} \tag{3.15}$$

the change in wavevector of the incident and scattered neutrons. In this case $\langle S_f|S_i\rangle$ for the four different spin interactions are

$$\langle S_f|S_i\rangle = \begin{cases} 1\begin{cases} |\uparrow\rangle \to |\uparrow\rangle \\ |\downarrow\rangle \to |\downarrow\rangle \end{cases} \text{Non} - \text{spin flip} \\[2em] 0\begin{cases} |\uparrow\rangle \to |\downarrow\rangle \\ |\downarrow\rangle \to |\uparrow\rangle \end{cases} \text{Spin flip} \end{cases} \tag{3.16}$$

All coherent non-magnetic scattering is non-spin flip.

For magnetic scattering the scattering potential is

$$V_m(\mathbf{Q}) = \left(\frac{-\gamma r_0}{2}\right)\boldsymbol{\sigma}\cdot\mathbf{M}_\perp(\mathbf{Q}) = \left(\frac{-\gamma r_0}{2}\right)\sum_\alpha \sigma_\alpha.M_{\alpha\perp}(\mathbf{Q}) \tag{3.17}$$

where the summation over α is the summation over the cartesian co-ordinates $x,\ y,\ z,$ and

$$\boldsymbol{\sigma} = 2\mathbf{S_n} \tag{3.18}$$

where is $\mathbf{S_n}$ is the spin of the neutron, and $M_{\alpha\perp}(\mathbf{Q})$ are the α components of the magnetization of the neutron perpendicular to the scattering wavevector, $\mathbf{Q}$, where

$$\mathbf{M_\perp} = -2\left[\mathbf{M} - (\mathbf{M}.\hat{\mathbf{Q}})\hat{\mathbf{Q}}\right] \tag{3.19}$$

with z defined as the direction of quantization of the neutron spin. For the four spin scattering processes we find (see chapter 9.3 of reference [78]):

$$\langle S_f | V_m(\mathbf{Q}) | S_i \rangle = \left(\frac{-\gamma r_0}{2}\right) \begin{cases} M_{z\perp}(\mathbf{Q}) & |\uparrow> \to |\uparrow> \\ -M_{z\perp}(\mathbf{Q}) & |\downarrow> \to |\downarrow> \\ M_{x\perp}(\mathbf{Q}) + iM_{y\perp}(\mathbf{Q}) & |\uparrow> \to |\downarrow> \\ M_{x\perp}(\mathbf{Q}) - iM_{y\perp}(\mathbf{Q}) & |\downarrow> \to |\uparrow> \end{cases} \tag{3.20}$$

Considering equations 3.19 and 3.20, if the neutron is polarized parallel to $\mathbf{Q}$ then the component of it's spin perpendicular to $\mathbf{Q}$ is zero because z is $\parallel$ $\mathbf{Q}$. Hence, *if the neutron polarization is parallel to the scattering wavevector all magnetic scattering is spin-flip, for both elastic and inelastic neutron scattering.*

3.3.2 Polarizing Neutrons

There are several different ways of producing a beam of polarized neutrons. In the work undertaken here, polarization of the incident neutron beam was achieved by use of a Heusler (Cu_2MnAl) monochromator, therefore I restrict the discussion of producing a polarized beam of neutrons to this technique.

The elastic scattering cross section of a centrosymmetric crystal[1] for neutrons can be expressed in terms of two scattering components, the nuclear scattering and the magnetic

---

[1] A centrosymmetric crystal has real values of $F_N(\mathbf{Q})$ and $F_M(\mathbf{Q})$.

scattering

$$\frac{\mathrm{d}\sigma}{\mathrm{d}\Omega} = [AF_N(\mathbf{Q}) + BF_M(\mathbf{Q})]^2 \tag{3.21}$$

where $F_N(\mathbf{Q})$ is the nuclear scattering structure factor, $F_M(\mathbf{Q})$ is the magnetic structure factor and A, B are constants of proportionality (see sections 3.2.1 and 3.2.3). As the scattering lengths are either positive or negative the two contributions to the scattering cross section can constructively or destructively combine.
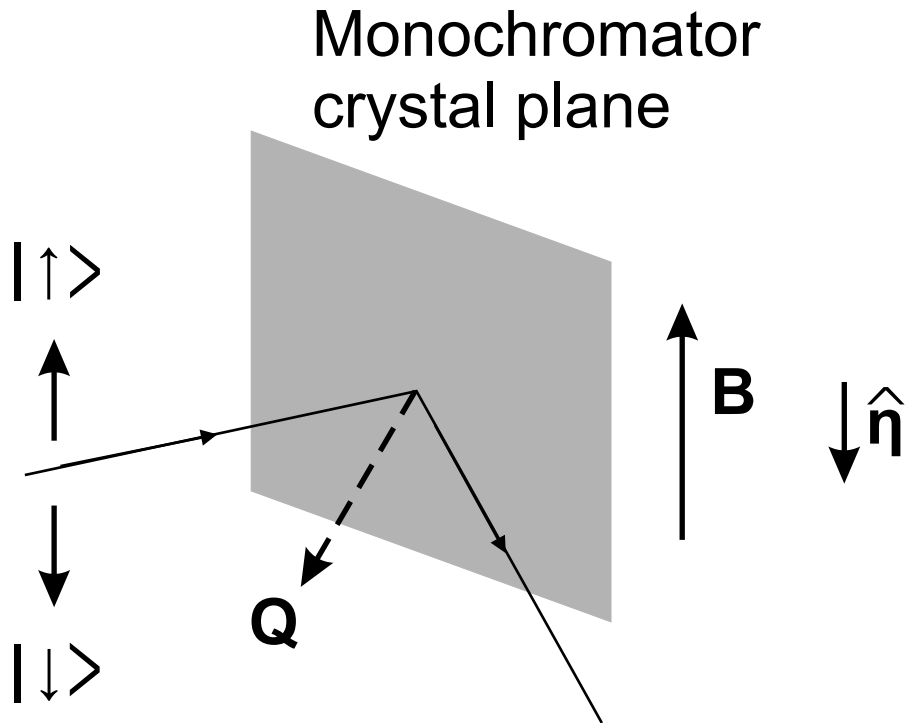
Figure 3.1: A diagram of the configuration for polarizing a neutron beam by use of a magnetic crystal monochromator.

Figure 3.1 shows a configuration that can be used to obtain a polarized neutron beam. The monochromator is magnetic with the field lying positively in the up direction. The cross section for this configuration is described by

$$\frac{\mathrm{d}\sigma}{\mathrm{d}\Omega} = (AF_N(\mathbf{Q}))^2 + 2ABF_N(\mathbf{Q})F_M(\mathbf{Q})(\mathbf{P}. - \hat{\boldsymbol{\eta}}) + (BF_M(\mathbf{Q}))^2 \tag{3.22}$$

where $\mathbf{P}$ is the polarization direction of the incident neutron and $\hat{\boldsymbol{\eta}}$ is a unit vector in the direction of the spins of the monochromator. Note that in this case $\hat{\boldsymbol{\eta}}$ refers to the spins of the crystal monochromator not the incident neutrons. For neutrons incident on the monochromator with spins up or down we have for $\mathbf{P}.-\hat{\boldsymbol{\eta}} = 1$:

$$\frac{\mathrm{d}\sigma}{\mathrm{d}\Omega} = [AF_N(\mathbf{Q}) + BF_M(\mathbf{Q})]^2 \tag{3.23}$$

Or for $\mathbf{P}.-\hat{\boldsymbol{\eta}} = -1$:

$$\frac{\mathrm{d}\sigma}{\mathrm{d}\Omega} = [AF_N(\mathbf{Q}) - BF_M(\mathbf{Q})]^2 \tag{3.24}$$

Clearly if $AF_N(\mathbf{Q}) = -BF_M(\mathbf{Q})$ the reflected beam will be fully polarized.

In practise 100% polarization of the incident neutron beam is not possible, and the data needs to be corrected for this imperfect polarization. To correct for the imperfect polarization of the incident neutrons a quantity known as the flipping ratio (f) is used. The flipping ratio can be defined in the following way, with the neutron polarization parallel to the scattering wavevector[2] and for scattering from a purely magnetic Bragg reflection:

$$f = \frac{\mathrm{SF_{obs}}}{\mathrm{NSF_{obs}}} \tag{3.25}$$

where $\mathrm{SF_{obs}}$ and $\mathrm{NSF_{obs}}$ are the observed count rates for the spin flip (SF) and non-spin flip (NSF) scattering. So the corrected counts for SF and NSF scattering are

$$\mathrm{SF} = \left(\frac{f}{f-1}\right)\mathrm{SF_{obs}} + \left(\frac{1}{f-1}\right)\mathrm{NSF_{obs}} \tag{3.26}$$

and

$$\mathrm{NSF} = \left(\frac{1}{f-1}\right)\mathrm{SF_{obs}} + \left(\frac{f}{f-1}\right)\mathrm{NSF_{obs}} \tag{3.27}$$

Although here I have defined f from scattering that is purely magnetic in origin, f can similarly be defined from scattering that is purely non-magnetic in origin.

---

[2]In this configuration all magnetic scattering is spin flip and all coherent non-magnetic scattering is non-spin flip.

3.4   Instrumentation

The large variation in neutron scattering experimentation carried out today requires an equally complex variation of instrumentation. There are different classifications of instruments, with significant variations for instruments within each class. With all these different type of instruments being computer controlled in operation and data acquisition. In this work we used two types of instruments, the triple-axis spectrometer and the time-of-flight chopper spectrometer, both of which can be used to study excitations in materials, such as phonons, or in this work magnons. I will now outline the basic concepts of these instruments and their components, without commenting on the many complex differences of individual instruments used in this work.

3.4.1   Triple-Axis Spectrometers

The triple axis spectrometer is the most commonly used type of instrument for studying excitations in materials, although they can also be used to study elastic scattering to characterize the static order.

Figure 3.2 shows a diagram of a triple axis spectrometer (TAS), with the three main components being the monochromator, the sample position and the analyser. The monochromator creates a monochromatic beam which is scattered off the oriented sample at the sample position and the analyzer is used to examine the neutrons which have been scattered off the sample in the desired manner for the scan selected. The following are brief outlines of the main components of a triple axis spectrometer

1) **Monochromator** − To make the incident beam of neutrons monochromatic a crystal
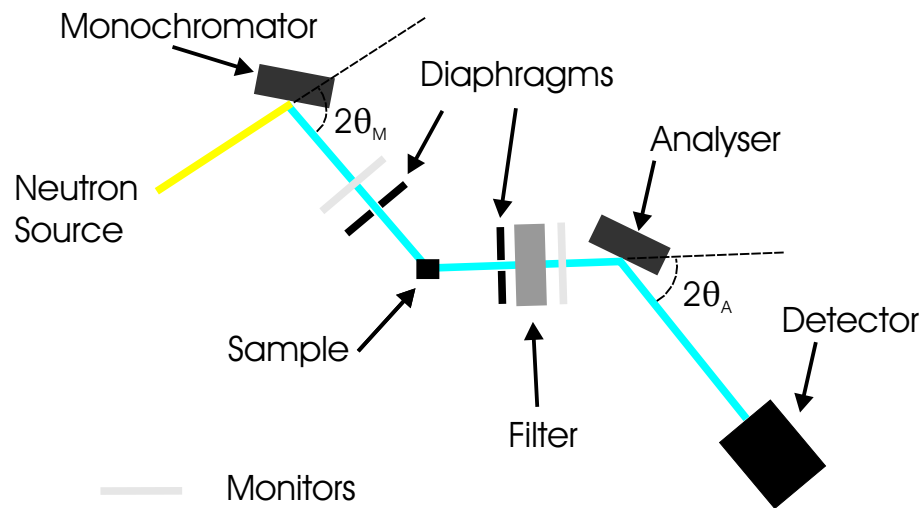
Figure 3.2: A triple axis spectrometer.

monochromator can be used. By scattering off an intense structural Bragg reflection only neutrons with the energy that corresponds to the desired Bragg condition for the monochromator will be diffracted through the angle $2\theta_M$, giving a monochromatic beam. The Bragg reflection off the monochromator selected for creating a monochromatic neutron beam must also be broad enough to ensure a high enough neutron flux. Monochromators are made from crystals of a range of different materials, in this work the instruments on which the data was taken used monochromators made from either pyrolytic graphite (PG) off the (002) reflection, silicon off the (111) reflection or for polarized neutrons a Heusler alloy crystal off the (111) reflection. The operation of a triple axis spectrometer with polarized neutrons will be discussed in section 3.4.2.

2) **Diaphragms** − The size of the incident neutron beam is typically larger than the size of the sample being studied, which means that not all of the incident neutrons scatter off the sample. These additional neutrons can scatter of other materials in the beams path, such as the cryostat that the sample is being cooled in. These additional

scattering processes can lead to spurious counts in the detector. To reduce the number of these additional neutrons diaphragms made from highly neutron absorbing materials are placed before and after the sample, these diaphragms are closed to define the beam size for the experiment.

3) **Monitors** – When performing a point by point scan we want the total number of incident neutrons for each point to be the same, and to achieve this we use a monitor. A monitor is a very inefficient detector, it detects a small fraction of the incident neutrons and allows the vast majority of neutrons to pass through. This allows us to determine the number of neutrons incident on the sample by counting to a desired number of neutrons detected by the monitor. A monitor placed after the sample can also be used to detect spurious scattering, which is often recorded as intense scattering in this monitor's counts.

4) **Sample** – The sample can be mounted in a number of different environments which depend on the conditions required for the experiment. Sample environments that are desired for experiments include high or low temperatures, high magnetic fields and high pressure. In our work on TAS instruments, cryostats were used to achieve low temperatures for our samples. The cryostat was mounted on a goniometer, which allows the sample to be orientated in the plane of the instrument enabling scans to be performed in this scattering plane.

5) **Filters** – The monochromator uses a Bragg reflection to create a monochromatic beam, however neutrons with wavelengths that are a whole fraction of the selected wavelength also satisfy this Bragg condition, and are called higher order harmonics.

These additional harmonics result in scattering that occur at wavevectors a half, a third, etc. of the positions expected from the selected wavelength. To suppress this higher harmonic scattering filters are used. One type of filter is a PG filter, which works by having a high transmission for the first harmonic at 2.662 Å^{-1} and a low transmission for higher order harmonics. For scattering carried out at lower energies a different type of filter made from beryllium or beryllium oxide can be employed. The filter is made of polycrystalline beryllium randomly aligned, so any neutrons with a wavelength shorter than the maximum spacing of the planes in beryllium will be scattered. The higher order harmonic scattering off the monochromator has a shorter wavelength than the first harmonic, so the higher harmonics are scattered out of the neutron beam by the beryllium filter but the first harmonic has too long a wavelength to scatter from any of the planes in the beryllium, and passes through the filter.

6) **Analyser** − In the same way that the monochromator uses a Bragg reflection to select the wavevector and energy of the incident neutrons the analyser also uses a Bragg reflection to select the scattered neutrons. By changing the Bragg reflection conditions at the analyser we have the ability to select the energy as well as the wavevector of the scattered neutrons we desire to study. Analysers are made from the same materials as the monochromators.

7) **Detector** − Most TAS use a single detector to record the scattered neutrons. Instead of a single detector a position sensitive detector (PSD) can be used. The advantage of using a PSD is that this allows you to define the area of the detector that is used for obtaining the counts of the scattered neutrons. This allows you the ability

to remove areas of the detector which receive no scattering from the sample but count
additional background counts.

These are the main features common to the majority of triple axis spectrometers.
Additional equipment needs to be added to this basic design for carrying out some
specialised experiments, e.g. polarized neutron scattering.
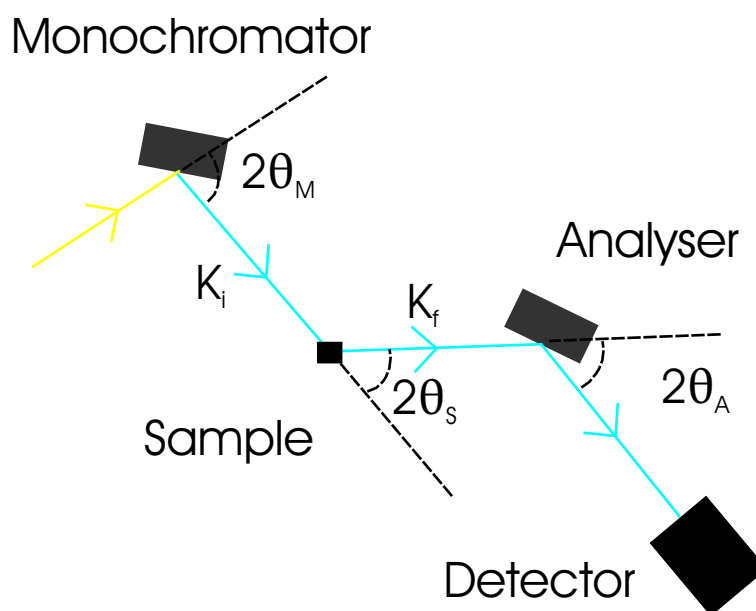
Figure 3.3: A diagram showing the incident and scattered wavevectors and
the scattering angles the neutron is scattered through for a scat-
tering event the scatters a neutron onto the detector of a triple
axis spectrometer.

In operation a triple axis spectrometer uses a continuous source of neutrons working at
either a fixed incident wavevector k_i or, a fixed final wavevector k_f. Figure 3.3 labels these
quantities and the angles a neutron has to be scattered through to reach the detector. If
the instrument is working with a fixed incident wavevector the sample position will remain
at a fixed position with respect to the monochromator and the analyzer and detector needs
to rotate about the sample to collect the scattered neutrons. Working with a fixed final

wavevector requires the whole of the spectrometer to move around the monochromator to select the necessary incident wavevector of the neutrons.

Out of these two configurations the one with fixed final energy is most commonly used for the following reasons. The most general form of the neutron scattering inelastic cross section can be expressed as

$$\frac{\mathrm{d}^2\sigma}{\mathrm{d}\Omega\mathrm{d}E} \propto \frac{k_f}{k_i} S(\mathbf{Q},\omega) \tag{3.28}$$

Where k_i and k_f are the incident and scattered neutron wavevectors respectively and $S(\mathbf{Q},\omega)$ is known as the response function. The measured cross section for inelastic neutron scattering is the number of neutrons scattered as counted by the detector, divided by the number of incident neutrons detected by the monitor of incident beam. The efficiency of this monitor is $\propto 1/k_i$, so the actual measured cross section for inelastic neutron scattering is

$$\frac{\mathrm{d}^2\sigma}{\mathrm{d}\Omega\mathrm{d}E} \propto \frac{detector\ counts}{k_i \times\ monitor\ counts} \propto \frac{k_f}{k_i} S(\mathbf{Q},\omega) \tag{3.29}$$

The factors of k_i between the expressions for the theoretical and measured cross sections cancel out. Hence, for constant k_f the ratio of detector counts to monitor counts is directly proportional to the response function $S(\mathbf{Q},\omega)$. To obtain from the measured inelastic cross section the response function in absolute units is difficult, as the measured cross section is dependent on quantities such as the reflectivity of the analyser. It is usual therefore to express the intensities obtained from the inelastic neutron cross section in relative intensities. In this thesis all measurements from experiments on TAS were taken with a fixed final energy, so that the measured inelastic cross sections are proportional to the response function.

3.4.2   Triple Axis Spectrometer with Polarized neutron analysis
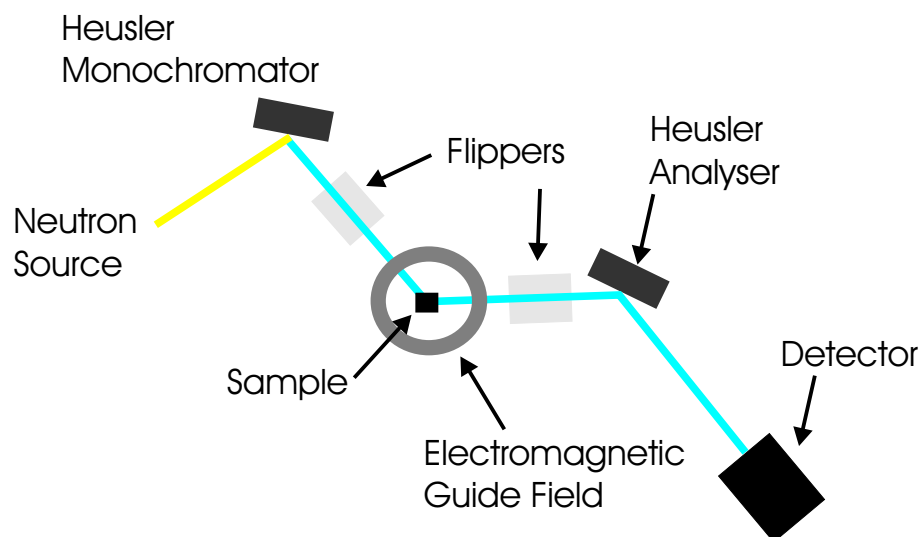
Figure 3.4: A diagram of the main components of a triple axis spectrometer
with polarized neutron analysis

When used for polarized neutron scattering the design of a TAS instrument is slightly altered from that of a TAS used for unpolarized neutron scattering. Figure 3.4 shows the main components of a TAS instrument with polarization anaylsis, where the incident neutron beam has been polarized by use of a Heusler monochromator (see section 3.3.2). The main change of components of the TAS instrument when working with polarized neutrons are the addition of two flippers, an electromagnetic guide field at the sample position and a Heusler analyser. The electromagnetic guide field is used to maintain the direction of the neutrons polarization with respect to the scattering wavevector. As with the Heusler monochromator the Heusler analyser only diffracts neutrons with one of the possible two spin configurations, in this way the Heusler analyser provides polarization analysis. Without the use of flippers before and after the sample only one of the four spin scattering cross sections could be examined, the flippers are added to change the polarization state of the incident and scattered neutrons. If both flippers are off then the

$| \uparrow \rangle \rightarrow | \uparrow \rangle$ scattering cross section is observed, whereas if the first flipper is off but the second flipper is on then the $| \uparrow \rangle \rightarrow | \downarrow \rangle$ scattering cross section is observed. In this way all four of the scattering cross sections can be studied.

3.4.3   Time of flight chopper spectrometer

Time of flight chopper spectrometers can be found at continuous neutron sources or pulsed neutron sources. The work we carried out on time of flight chopper spectrometers was all performed on the instrument MAPS at the pulsed neutron spallation source ISIS, therefore I will restrict my description of these instruments to the design for pulsed neutron sources.

Unlike triple axis spectrometers (TAS) scans are not collected in a point by point manner by a single detector, but the scattered neutrons are detected in large detector arrays. By knowing the time at which the scattered neutrons hit the detectors and the initial energy of the neutron it is possible to determine by time of flight analysis the energy transferred to the system. MAPS also employs position sensitive detectors that as well as detecting when the neutron hits the detector also detect where it hits the detector, thus enabling detailed mapping of reciprocal space in 3 dimensions, a 2-D spatial surface and energy transferred to the system. In this way one scan lasting ~ 2 days on an instrument such as MAPS is the equivalent to performing a very large number of scans on a TAS instrument. This has the advantage of mapping out large areas of reciprocal space and more readily revealing additional excitation modes, whereas TAS instruments allow you to perform scans with larger neutron flux at positions of interest in reciprocal space.

In figure 3.5 a schematic diagram of a time of flight chopper spectrometer is shown. A pulse of neutrons is created by spallation and these neutrons are reduced in energy by a
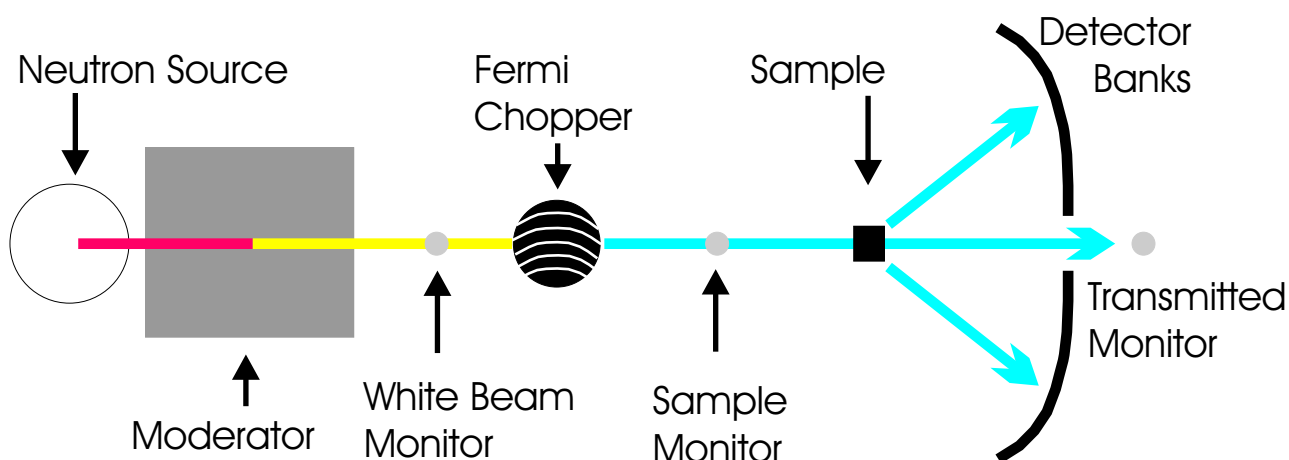
Figure 3.5: A time of flight chopper spectrometer for a pulsed neutron source.

moderator to energies useful for examining magnetic excitations. The energy bandwidth of the incident neutrons is then selected by use of a Fermi chopper. A Fermi chopper is a rotating drum that is synchronized to the neutron pulses, made from alternating curved strips of a material that is transparent to neutrons (e.g. aluminium) and strips which are strong neutron absorbers (e.g. boron) that lie in the plane of the neutron beam. The phase of the chopper relative to the neutron pulse is chosen so that neutrons with the desired energy pass through the chopper but slower or faster neutrons hit the absorbing strips. The energy width of the neutrons selected by the Fermi chopper is determined by the frequency of rotation of the chopper, the higher the frequency the narrower the energy width. This monochromatic neutron beam is then scattered off the sample into large detector arrays designed to collect scattering over a wide angle. An advantage of a chopper spectrometer at spallation source is that certain background processes, e.g. due to fast neutrons, only affect a small fraction of the time channels, so the background is generally lower.

3.5   Time of Flight Analysis

Time of flight analysis uses the knowledge of when a neutron was produced and the path length the neutron travels to determine how the neutron was scattered. From this analysis the energy and wavevector of the excitation caused by the scattered neutron can be determined. With pulsed sources the time of the production of the neutrons is well defined, so time of flight analysis is ideally suited for this type of source. Although nuclear reactors produce a continuous source of neutrons, choppers can be used to provide pulses of neutrons.

In any scattering process a neutron undergoes, energy is conserved

$$E = \hbar\omega_{\mathbf{q}} = E_i - E_f \tag{3.30}$$

where ω is the angular frequency of the excitation of wavevector $\mathbf{q}$ created by the neutron, E_i is the neutron's initial energy, E_f is the neutron's final energy and $\hbar$ is the planck constant divided by 2π. The final energy of the neutron can be expressed as

$$E_f = \frac{1}{2}mv^2 \tag{3.31}$$

where m is the mass of the neutron and v is the velocity of the neutron. By knowing how far from the sample the neutron was detected, d, and when it was detected, t, the neutron velocity can be determined as

$$v = \frac{d}{t} \tag{3.32}$$

Which leads to the energy transferred to the system being

$$E = \hbar w_q = E_i - \frac{md^2}{2t^2} \tag{3.33}$$

From $v = d/t$ we know the speed of the neutron, which can be converted into the de Broglie wavelength;

$$\lambda = \frac{h}{mv} = \frac{ht}{md} \tag{3.34}$$

From this wavelength the magnitude of the wavevector of the excitation can be determined. As $\mathbf{k_i}$ and $\mathbf{Q}$ are determined from the sample orientation, and $\mathbf{k_f}$ can be determined by the position and time the scattered neutron was detected, the direction of the excitation's wavevector can be determined by conservation of momentum

$$\mathbf{k_i} - \mathbf{k_f} = \mathbf{q} + \boldsymbol{\tau} \tag{3.35}$$

where $\mathbf{k_i}$ and $\mathbf{k_f}$ are the incident and scattered wavevectors of the neutron, $\mathbf{q}$ is the wavevector of the excitation and $\boldsymbol{\tau}$ a reciprocal lattice wavevector that maps $\mathbf{q}$ back into the first Brillioun zone. This allows us to map out the intensities of the scattered neutrons in terms of the wavevector and energy transferred to the system.

In practise, for the measurements I performed on the time of flight chopper spectrometer MAPS the scattered neutron intensities are measured in detector-position-time binning which is converted into $(\mathbf{Q}, \omega)$ space. The data is then converted into absolute units by normalizing the data to white beam scattering from a standard vanadium sample, which corrects variations in detector sensitivity. This is achieved on MAPS using the programme HOMER. The normalized data set corresponds to;

$$S(\mathbf{Q}, \omega) = \frac{k_i}{k_f} \frac{d^2\sigma}{d\Omega_f dE_f} \tag{3.36}$$

with units of mbarn/(sterdian meV formula-unit). In this way from the measured double differential cross section the response function is gained in absolute units.

3.6 Measuring Dispersion Relationships

Inelastic neutron scattering can be used to measure the the dispersion of excitations such as phonons and spin waves. Data obtained from using triple axis spectrometers and time of flight chopper spectrometers with position sensitive detectors can be used to map out dispersion curves.

The most common technique for measuring dispersion curves is to measure a series of scans of the energy at a constant $\mathbf{Q}$ through the dispersion across the entire Brillioun zone, this is known as a constant $\mathbf{Q}$ scan. In this work however, we chose to measure the dispersion by carrying out a series scans of $\mathbf{Q}$ across the entire Brillioun zone for constant energies, known as a constant energy scan. One reason for our choice in mapping out the spin wave dispersion is that the incommensurate nature of the spin order leads to excitations that are sharp in constant energy scans but broad in constant $\mathbf{Q}$ scans, hence the spin wave excitations are more readily mapped out by performing constant constant energy scans (or cuts in the case the time of flight data). A second reason is that in constant energy scans phonon excitations tend to have relatively flat dispersions[80], making it possible to separate out the spin wave excitations from the phonon excitations in constant energy scans. Figure 3.6 gives examples of the these two types of scans, the constant $\mathbf{Q}$ scans scan where $\mathbf{k_f}$ and $\mathbf{Q}$ are kept constant while $\mathbf{k_i}$ is varied and a constant energy scan where $\mathbf{k_f}$ and E are kept constant while $\mathbf{Q}$ is varied.

In either type of scan peaks are observed in the scattered neutron intensity when the scan crosses the dispersion curves. By mapping out the centres of these peaks the dispersion relation for the material can be determined. The scattering must obey energy and
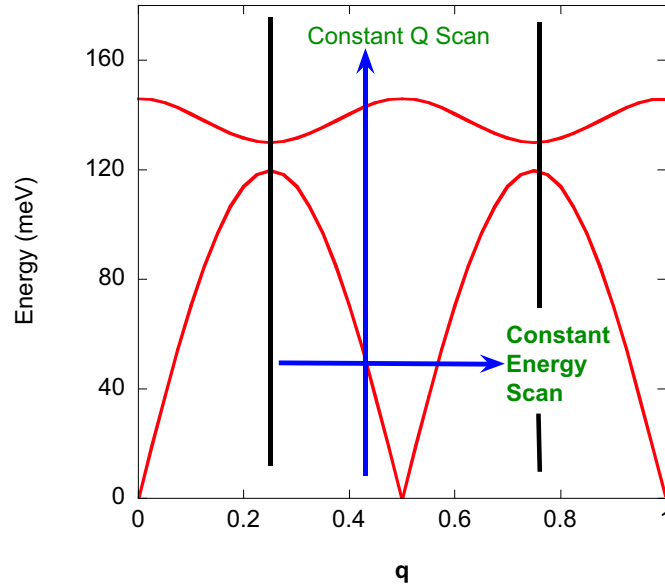
Figure 3.6: A diagram showing the two ways to map out a dispersion curve,
a constant energy scan or a constant **Q** scan. The two solid
vertical lines represent the zone boundaries of Brillioun zone for
this dispersion relation.

momentum conversation. The condition for momentum conservation can be expressed as

$$\mathbf{k_i} - \mathbf{k_f} = \mathbf{q} + \boldsymbol{\tau} \tag{3.37}$$

where $\mathbf{k_i}$ and $\mathbf{k_f}$ are the incident and scattered wavevectors of the neutron, $\mathbf{q}$ is the
wavevector of the excitation and $\boldsymbol{\tau}$ a reciprocal lattice wavevector that maps $\mathbf{q}$ back into
the first Brillouin zone.

Important information can be obtained from the scattering intensity variation with E. As
the neutron flux varies with incident energy it is important to ensure that the number of
incident neutrons is the same for different energies, this is achieved by use of a monitor in
the incident beam (see section 3.4.1). It should be noted that the efficiency of monitors
on different instruments varies, so direct comparisons between intensities on different
instruments can not easily be achieved.

Chapter 4

Sample Growth

The samples used in this work are single crystals of $La_{2-x}Sr_xNiO_{4+\delta}$ that were grown by the floating zone technique. The majority of the crystals used in this work were grown by D. Prabhakaran via the following technique (description taken from the reference [81] by D. Prabhakaran *et al.* on growth of large single crystals of $La_{2-x}Sr_xNiO_4$). Stoichmetric proportions of $La_{2-x}Sr_xNiO_4$ were prepared by mixing the starting materials of La_2O_3, $SrCO_3$ and NiO. This mixture was fired at $1200 - 1300°C$ for 72h. After intermittent regrinding this process was repeated until the material was a single phase. This material was then hydraulically pressed into feed rods of typically $12\,mm$ diameter and $100\,mm$ in length. To make the feed rods dense and straight they were sintered in a vertical furnace at $1500°C$ for $6-12h$. Crystal growth was achieved by using a a floating zone mirror furnace (Crystal Systems Inc.) with a $5-7$ atmosphere of Ar mixed with a small concentration of oxygen.

The oxygen content of the crystals produced by D. Prabhakaran was determined destructively by thermogravimetric analysis (TGA). For a TGA measurement a single crystal sample is ground into a polycrystalline sample. The polycrystalline sample is then broken down by the application of heat into the constituent metal oxides and elements that
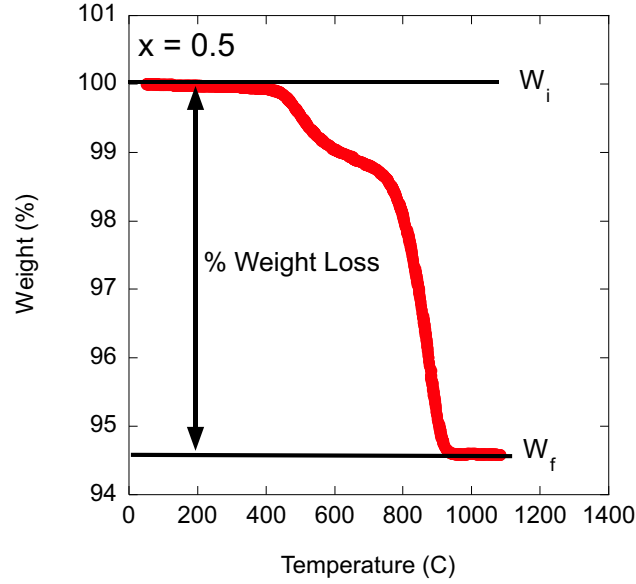
Figure 4.1: A TGA measurement on a x = 0.5 sample. The graph records the variation of the weight of the sample with temperature relative to the initial sample weight.

make up the sample, with the weight of the sample being recorded during this process. From the difference in weight of the end material to starting material the oxygen content of the sample can be deduced. In the TGA measurements carried out in this work the sample was heated at a rate of $10\,\mathrm{K/min}$ in an atmosphere of $98\,\%$ Ar and $2\,\%$ H_2. The $La_{2-x}Sr_xNiO_{4+\delta}$ sample decomposes in the following way

$$La_{2-x}Sr_xNiO_{4+\delta} + H_2 \rightarrow \left(\frac{2-x}{x}\right)La_2O_3 + x.SrO + Ni + (1+\delta+0.5x).H_2O \quad (4.1)$$
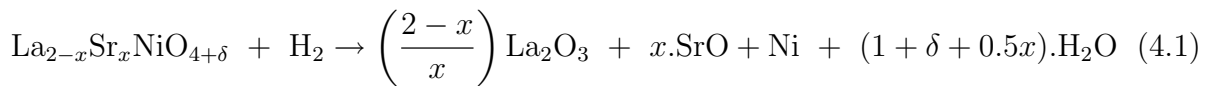
With initial and final weights of the sample in this reaction being

$$W_i = n.MW(La_{2-x}Sr_xNiO_{4+\delta}) \quad (4.2)$$

and

$$W_f = n.\left[\left(\frac{2-x}{x}\right)MW(La_2O) + x.MW(SrO) + MW(Ni)\right] \quad (4.3)$$

where MW is the molar weight and n is the number of mols. Hence, by recording the initial and final mass of the sample the molecular weight of the starting sample can be determined, and from this the oxygen content can be deduced.

Figure 4.1 shows TGA results for a $x = 1/2$ sample. On heating the sample's weight is constant below 400°C above this temperature the weight slowly drops by 1% between 400-600°C, followed by significant weight loss between 800-950°C and above this temperature the sample's weight remains constant. The weight loss between 400-600°C is due to partial loss of oxygen from $La_{2-x}Sr_xNiO_{4+\delta}$, i.e. the value δ changes. The weight loss seen between 800-950°C corresponds to the sample decomposing into its constituent parts. So the reaction shown in equation 4.1 corresponds to the total weight loss seen between 400-950°C. Table 4.1 shows the δ content of the different doping levels studied in this thesis.

Sr	0	0.1	0.2	0.225	0.25	0.275	0.3	1/3	0.4	1/2
δ	0.11	0.075	0.01	0.07	0.06	0.02	0.01	0.015	0.005	0.02
n_h	0.22	0..25	0.22	0.365	0.37	0.315	0.32	0.36	0.41	0.54

Table 4.1: Oxygen content, δ, and hole content, n_h, for our samples, determined by TGA measurements. The standard error in δ is 0.01.

No TGA measurements have been carried on a crystal of the $x = 0.37$ composition, but the ordering temperatures of this sample are in good agreement with previous work on samples of similar doping[34, 38].

The $x = 0.275$ sample used for the MAPS experiment was an array of four crystals coaligned by x-ray diffraction (see chapter 7.2), which were grown at Kyoto University. A

crystal similar to these samples was studied by neutron diffraction in reference [35], with

the crystal being found to be stoichmetrically doped.

Chapter 5

Magnetization Measurements of La$_{2-x}$Sr$_x$NiO$_4$

In this chapter I present magnetization measurements on single crystals of La$_{2-x}$Sr$_x$NiO$_{4+\delta}$[82]. This study was undertaken to characterize the nature of the ground state of LSNO over a wide range of doping levels. The investigation highlights differences between the commensurately ordered compositions ($x = 1/3$ and $1/2$), compared to the incommensurately ordered compositions. The work complements the recent high temperature magnetization work carried out by Winkler*et al.*[71]. Winkler*et al.* concentrated on the paramagnetic magnetization, whereas this work concentrates on the magnetism below charge-ordering.

Figure 5.1 shows a set of typical results for the magnetization of a LSNO compound, obtained from a sample with $x = 0.275$ with a measuring field of 500 Oe applied parallel to the ab plane. For the field-cooled (FC) data, on cooling we observe the charges to order at $T_{\mathrm{CO}} \approx 170\,\mathrm{K}$ and then the spins order at $T_{\mathrm{SO}} \approx 110\,\mathrm{K}$. The zero-field-cooled (ZFC) data shows splitting from the FC data that is characteristic of a freezing of spins, like a spin glass. During field cooling randomly aligned spins or spin domains are ordered by
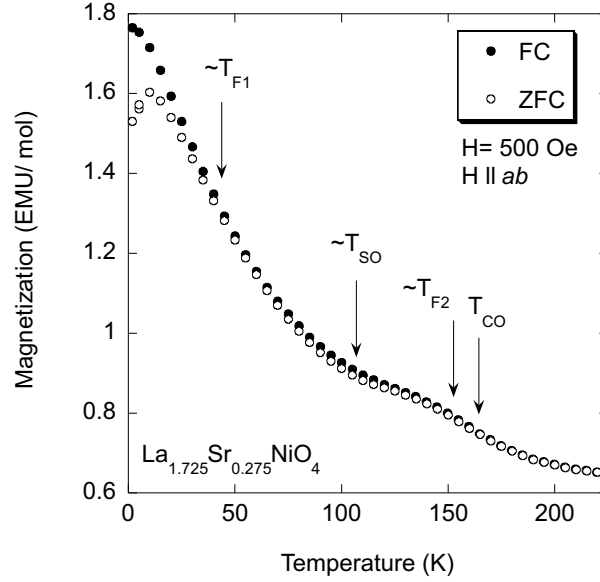
Figure 5.1: A typical set of ZFC and FC data for a LSNO material, show-
ing the convergence of the FC and ZFC magnetization between
T_{SO} and T_{CO}. The charge ordering, T_{CO}, (as confirmed by x-
ray scattering[42]) spin ordering T_{SO}, (as confirmed from neu-
tron diffraction) and spin glass temperatures, T_{F1} and T_{F2}, are
indicated.

the application of a magnetic field, which causes an increase in the bulk magnetization
of the sample, whereas in zero field cooled measurements the spins or spin domains have
not been aligned by the field so the bulk magnetization is less than that of the FC. The
ZFC-FC splitting is large below $T_{F1} \approx 40\,\mathrm{K}$ in the case of $x = 0.275$, with a smaller
ZFC-FC splitting that persists to a much higher temperature T_{F2} (where there is no ZFC-
FC splitting). I define T_{F1} as the temperature at which the ZFC-FC splitting becomes
constant with temperature. Below T_{F1} the ZFC-FC splitting widens, although in many
cases it only becomes large at the temperature of the ZFC peak. The ZFC peak is not
used as the definition of the spin freezing temperature as 'memory' effects observed in
these materials are found to be more closely correlated with T_{F1}. I define T_{F2} as simply
the temperature above which the ZFC magnetization matches the FC magnetization.

The measurements indicate that the ground state for all doping levels shows highly 2-dimensional irreversible magnetic behaviour in the ab plane. The irreversible magnetic behaviour has two components, a large low temperature component typically below $T_{\mathrm{F1}} \sim 50\,K$ and a much smaller component that survives to approximately the charge ordering temperature. In the $x = 1/3$ sample the low temperature component of the irreversible magnetization is found to be greatly enhanced compared to that in other doping levels.

For fields applied parallel to the ab plane the magnetization shows a 'memory' effect in the magnetic field – temperature history. This effect is found across the entire doping range of LSNO studied, but it was found to be suppressed in the low temperature spin orientation of $x = 1/3, 0.275$ and 0.37 (see chapter 6). The existence of this 'memory' effect was found to be correlated with the magnetic irreversibility.

5.1 Experimental detail

Single crystals of La$_{2-x}$Sr$_x$NiO$_{4+\delta}$ used in this work were grown in Oxford by the floating-zone technique[81]. Details of the sample preparation can be found in chapter 4. Typical dimensions of these crystals are $\sim 5 \times 5 \times 2\,\text{mm}^3$, with masses typically in excess of 50 mg. The oxygen excess (δ) as determined by thermogravimetric analysis (TGA), see chapter 4, and are displayed in table 4.1. Although no TGA measurements have been carried on the $x = 0.37$ composition, we have fully characterized a larger as-grown $x = 0.37$ sample, by neutron diffraction, see chapter 6.2. The temperature dependence of the magnetic and charge order of as grown crystals have been characterized for most x concentrations by neutron diffraction (see chapter 6.2) and x-ray diffraction[42].

The magnetization measurements were made by using a SQUID magnetometer (Quantum Design). Measurements were taken by the $d.c.$ method. Scans were performed with either the magnetic field parallel to the ab plane ($H \parallel ab$) or parallel to the crystal c axis ($H \parallel c$). For measurements parallel to the c axis it was necessary to use a rotating plate sample mount to align the sample's orientation, using the anisotropy of the magnetization to align the crystal, see chapter 2.2. For measurements taken when using the rotating mount a significant background from the mount device has been subtracted from the data, and hence any measurements where the rotating mount was used will be indicated.

We performed the majority of scans via two techniques, (i) by cooling in an applied field whilst measuring (FC) ,and (ii) by cooling in zero field and measuring while warming in a field (ZFC), typically using a measuring field of 500 Oe. Remnant magnetic fields were measured by applying a field for 5 minutes at a fixed temperature, then setting the field to zero and measuring the time dependence of any signal seen, taking t $= 0$ to be when

the field reaches zero. Other scans we employed will be explained alongside the results

off the scans.

5.2 Magnetization measurements $0 \leq x \leq 0.5$
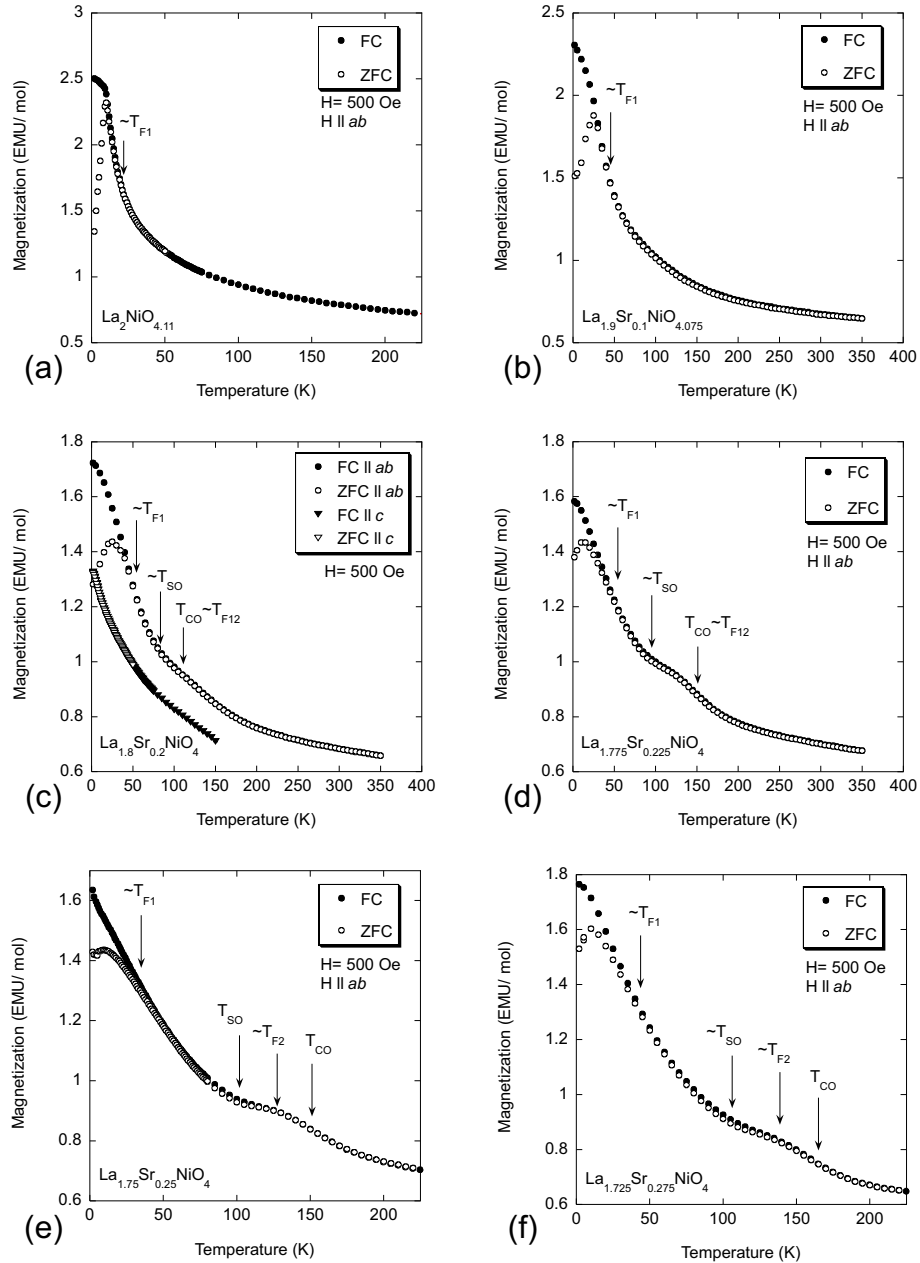
Figure 5.2: Zero field cooled (ZFC) and field cooled (FC) magnetization data for different compositions of La$_{2-x}$Sr$_x$NiO$_{4+\delta}$ for $0 \leq x \leq 0.275$.

We carried out magnetization measurements on eleven samples of La$_{2-x}$Sr$_x$NiO$_{4+\delta}$ for $0 \leq x \leq 0.5$. Magnetization readings determine the temperatures at which transitions occur, but do not determine the nature of the transition. The nature of the transition
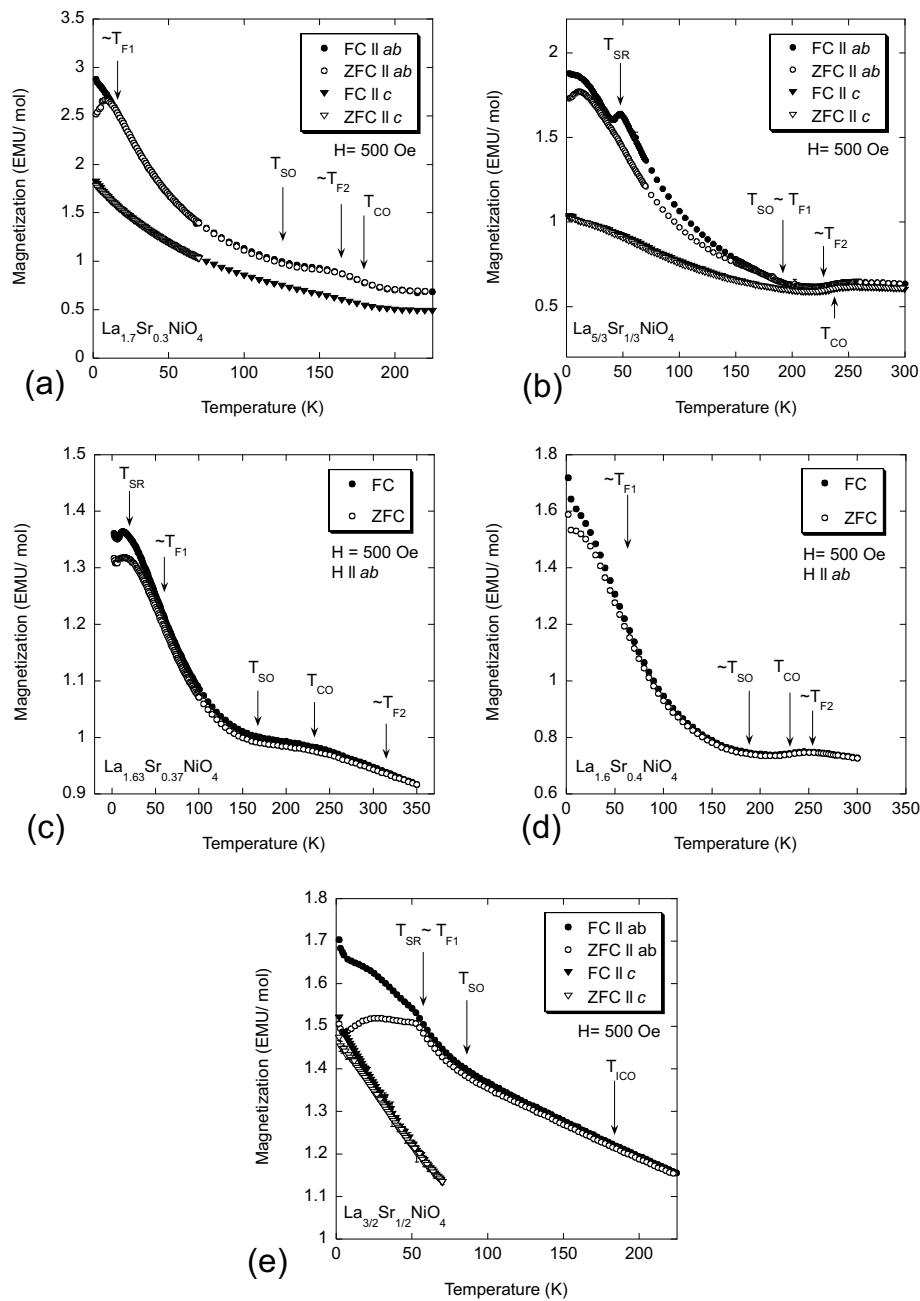
Figure 5.3: Zero field cooled (ZFC) and field cooled (FC) magnetization data for different compositions of La$_{2-x}$Sr$_x$NiO$_{4+\delta}$ for $0.3 \leq x \leq 0.5$. The rotating mount was employed for measurements $\parallel c$ in the $x = 1/3$ material.

needs to be determined from other techniques, such as neutron and x-ray diffraction. The work in chapter 6 is a neutron diffraction study of several different doping levels of LSNO. Hence, by comparing the magnetization data to our neutron diffraction study, we

can determine the nature of the transitions we observe in the magnetization work of this chapter.

Examples of several FC and ZFC measurements with $H \parallel ab$ can be seen in figure 5.2 and figure 5.3. We observe from these results that for all doping levels studied a ZFC-FC splitting exists with $H \parallel ab$, a ZFC-FC splitting is characteristic of irreversible magnetic behaviour. This splitting has two regimes, on warming there is a large ZFC-FC splitting at low temperatures below $T_{F1} \sim 50$ K [1], followed by a second smaller gap that widens around the spin ordering temperature and persists to approximately the charge ordering temperature, $T_{F2} \sim T_{CO}$. For $x = 0.37$ and 0.4 we observe the transition temperature of T_{F2} to be higher than T_{CO}. For $x = 1/2$ the spin ordering temperature (T_{SO}) is much lower than the charge ordering temperature, see figure 5.3(e). In the $x = 1/2$ sample no opening of ZFC-FC splitting occurs around the spin ordering temperature. For the $x = 0.2, 0.3, 1/3$ and $1/2$ samples data has also been taken with $\mathbf{H} \parallel c$. This data is also shown in Fig.5.2 and Fig.5.3, and clearly showing the $2-$D nature of the magnetic irreversibility with no significant ZFC-FC splitting with H parallel to the crystal c-axis. In the $x = 1/3$ material T_{F1} is observed to extend to ~ 195 K$\sim T_{SO}$, a further example of how the commensurate charge-stripe order in the $x = 1/3$ material leads to an enhancement of the material's properties (see Fig.5.3(c)).

In figure 5.4 the charge ordering temperatures are displayed versus x. For comparison we include in the figure the ordering parameters available on LSNO in literature. Previous phase diagrams display hole concentration $n_h = x + 2\delta$, not x, but as can be seen in the inset of figure 5.4 a plot against n_h from our samples show no coherent pattern. This result is in agreement with the μSR study by Jestädt *et al.*[83]. No data on La$_2$NiO$_{4+\delta}$

---

[1]I define T_{F1} as the temperature at which the ZFC-FC splitting becomes constant with temperature.
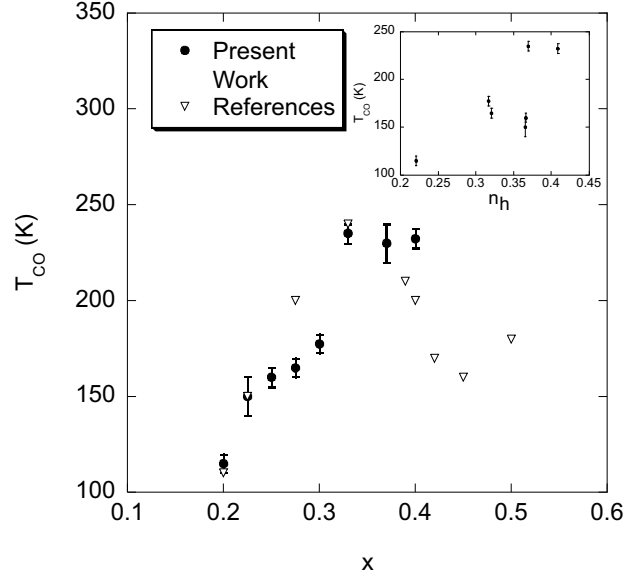
Figure 5.4: The charge ordering temperatures of LSNO versus Sr doping x.
The inset to a) shows the charge-ordering temperatures versus
n_h, which shows no trend. The points included from references
are taken from references [32, 33, 34, 35, 38, 36].

(LNO) compounds is included, as the excess oxygen in LNO forms an ordered supercell
structure that the charge-ordering locks into[48], unlike any ordering we are aware of for
LSNO.

No charge or spin ordering was observed by us in the magnetization data for $x = 0$
or 0.1, and neither of the crystals have been examined by diffraction techniques. However,
literature reports suggest the excess oxygen level in the $x = 0$ sample may cause the
material to charge order[84, 85, 86, 87], and given the total hole doping for $x = 0.1$,
charge ordering could also be expected to occur in the $x = 0.1$.

In figure 5.5 we record the temperature of the magnetization peak in ZFC measurements
shown in Fig.5.2 and Fig.5.3. This peak temperature is seen to occur at $\sim 10\,\mathrm{K}$ for most
doping levels apart from the $x = 0.1, 0.2$ and $1/2$ compounds.
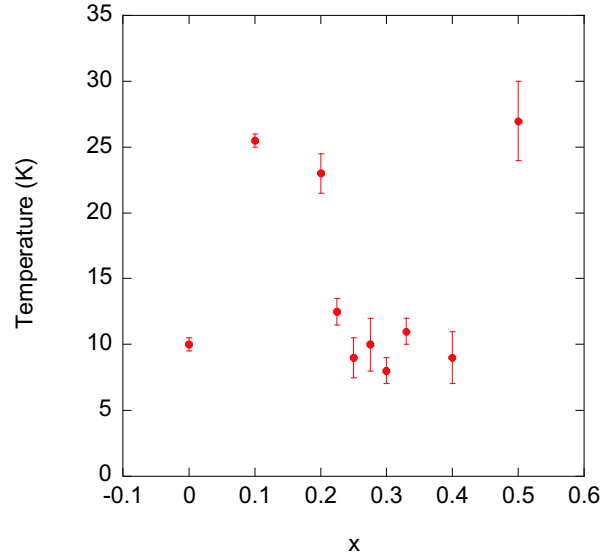
Figure 5.5: The doping dependence of the peak temperature of the ZFC magnetization in $H = 500$ Oe, with H $\parallel ab$.

Attempts to fit our magnetization data in the paramagnetic state with the Curie-Weiss law are in good agreement with the high temperature work of Winkler et $al.$[71]. Curie temperatures thus obtained were of the order of -600 K, indicating antiferromagnetic ordering, which is far larger than the typical measured value of $T_{\text{SO}} \sim 150$ K.

Remnant magnetic signals were induced by application of a field of 500 Oe at a fixed temperature for 5 minutes, then switching the applied field off and measuring the time variation of the induced signal. We chose the temperature at which the field was applied to be below T_{F1}, as this is the temperature range where the largest magnetic irreversibility exists. Figure 5.6 shows the time variation of the remnant signal induced in the $x = 1/3$ compound at 2 K: the signal is observed to initially decay relatively quickly before slowing down to a much slower decay rate. In Fig. 5.6 we have indicated with two straight lines these two different regimes. A decaying magnetic signal is observed when the field was applied $\parallel ab$ plane, but no significant induced signal is observed when the field was applied

$\parallel c$ (not shown). We carried out fits of the remnant signals with a standard stretched exponential $M(t) = Mexp(-\alpha t^{(1-n)})$. These data fits are found to be unsatisfactory, and could not accurately be used to determine n for comparison with the theoretical value of 2/3 expected for a spin glass[88]. A good fit of the data could be achieved with two stretched exponentials, but no information could be obtained from this fit due to the large errors in the fitted variables.
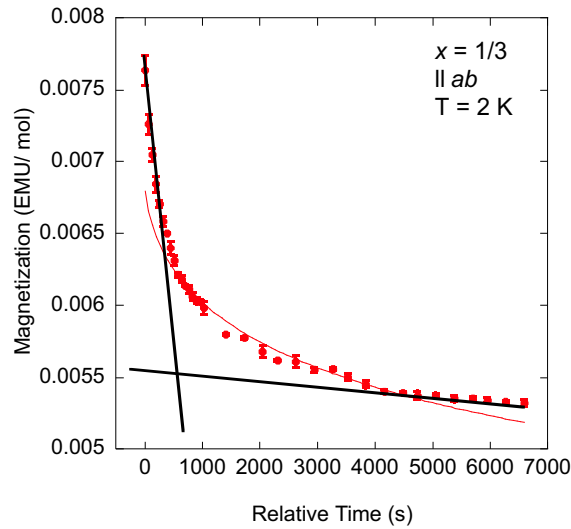
Figure 5.6: The time dependence of the signal in $x = 1/3$ induced by application of $H = 500\,\text{Oe} \parallel ab$ for 5 minutes at $T = 2\,\text{K}$. With the relative time being the time after setting $H = 0$. The red curve is a fit of a stretched exponential to the data and the two black lines indicate the two different decay regimes of the induced signal.

5.3 'Memory' Effects

In our initial work several interesting features were observed in measurements performed with $H \parallel ab$ plane, namely the slow relaxation in the magnetization, and the significantly higher value of T_{F1} for $x = 1/3$. In this section I show how the relaxation in the remnant magnetization leads to a novel 'memory' effect when the temperature is varied. I carried out this study by performing the following method:

Inducing a signal by FCing: Cool the sample from $300\,\mathrm{K}$ to T_0 in a field of $500\,\mathrm{Oe}$ $\parallel ab$, remove the field, cool to $2\,\mathrm{K}$, and then measure in zero field while warming.

Figure 5.7 shows the variation with T_0 of the signal induced by this method in the $x = 1/3$ material. These measurements indicate that a magnetic signal can be induced for $T < T_{\mathrm{F1}}$, ($T_{\mathrm{F1}} \approx T_{\mathrm{SO}} \approx 190\,\mathrm{K}$).

At $T_{\mathrm{SR}} \approx 50K$ a known spin reorientation occurs[35], and this spin reorientation is observed to dramatically affect the the signal induced by the FCing method. For $T_0 > 50K$ the trend on heating from $2\,\mathrm{K}$ is for the induced magnetization to be a relatively weak constant magnitude at low temperatures, rising sharply in magnitude just below T_{SR}. Then above T_{SR} the induced magnetization decreases with increasing temperature, with a decrease of the temperature gradient at T_0, which is illustrated prominently in the $T_0 = 140\,\mathrm{K}$ data. The induced magnetization then levels off to a near constant value at $\sim 190\,\mathrm{K} \sim T_{\mathrm{SO}} \approx T_{\mathrm{F1}}$. The lower T_0 is, the larger the induced magnetization is. This is true across the entire temperature range of the measurements.

For the case of the $x = 1/3$ when $T_0 < 50\,\mathrm{K}$, the induced magnetization is approximately constant on warming from $2\,\mathrm{K}$ to T_0. Above T_0 it then falls, before gaining strength when heated through the spin reorientation. Further increasing the temperature causes

Figure 5.7: The variation of the signal induced by field-cooling $H = 500$ Oe $\parallel ab$ to T_0 (indicated in the key). Then cooling to 2 K in zero field, and measuring while warming in zero field. The measurement are for the $x = 1/3$ material.

the signal to decay in strength until T_{F1}, where it finally levels off to a constant value. Overall the lower the value of T_0 the larger the induced magnetization is.

We investigated the dependence of the induced magnetization on the size of the inducing field for $T_0 = 70$ K, and found that the induced magnetization increased in size with the inducing field, with little indication of the induced signal saturating for inducing fields up to 5 T in magnitude (not shown). The signal was also found to be highly time stable up to 2 hours. We also determined that the magnitude of the induced signal was the same for field cooling at a rate of 10 K/min or 3 K/min (not shown).

Figure 5.8 shows the results for different doping levels of the magnetization induced by field cooling in $H = 500$ Oe $\parallel ab$ to $T_0 = 10$ K, and measuring in zero field while warming, we

include data for $x = 1/3$ with $T_0 = 70$ K for comparison purposes. In the low temperature

spin orientation for $x = 0.275$ and 0.4 (see chapter 6) no suppression of the induced

magnetization is seen, unlike the behaviour of the $x = 1/3$. In the low temperature spin

phase of $x = 0.37$ the induced magnetization is suppressed in a fashion similar to, but less

dramatic than, the $x = 1/3$. For the low temperature spin phase of $x = 1/2$ there is no

'suppression' of the induced magnetization, however at the spin reorientation temperature

$T_{SR} = 57$ K ($\simeq T_{F1}$), there is a sharp change in gradient of the induced magnetization. The

trend for doping levels other than $x = 0.37, 1/3$ or $1/2$, is a constant magnitude induced

signal observed up to T_0, above which the induced magnetization decays in strength and

levels off to a near constant value at around T_{F1}. In the O doped material and the $x = 0.2$

this induced magnetization was seen to be significantly larger than for the other doping

levels, with the induced signal in the O doped material decaying rapidly with increasing

temperature.

With the stripe-ordering in $x = 0.275$ being incommensurate with the crystal lattice and

there being no coincident ordering temperatures, we chose to investigate the memory

effects in this material further. In figure 5.9 we can see the results of inducing a signal

by the standard field cooling method, which involves cooling in $H = 500$ Oe applied $\parallel ab$

to T_0 followed by, cooling to 2 K in zero field and measuring the remnant magnetization

while warming in zero field, for different values of T_0. On warming, the induced signal

shows signs of a small increase below ~ 10 K. Above ~ 10 K the signal slightly decreases,

before decaying away in an exponential fashion on heating through T_0. Again, the lower

T_0 is, the larger the induced signal is. For $T_0 > T_{F1}$ we still observe a decaying signal

above T_0, which changes into an almost linear decay at $\sim T_{CO}$, at this temperature there

is still a significant non-background signal. The size of the induced magnetization for
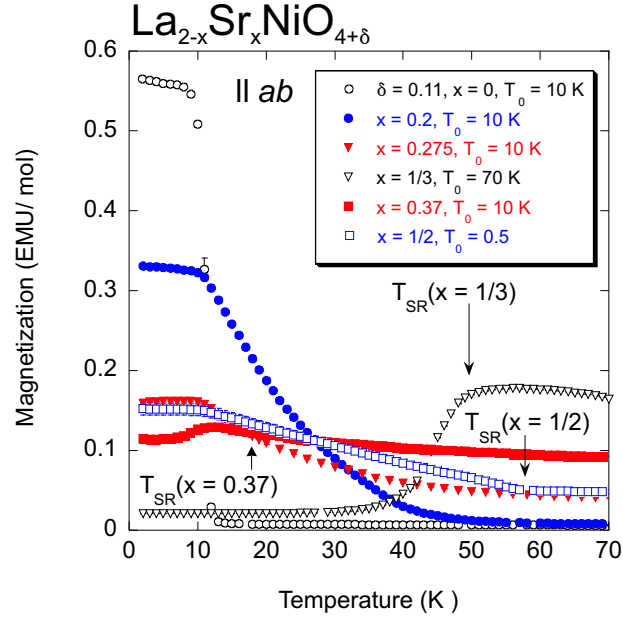
Figure 5.8: The signal induced by field-cooling in $H = 500\,\mathrm{Oe} \parallel ab$ to T_0 (indicated in the key) then cooling to $2\,\mathrm{K}$ in zero field and measuring while warming in zero field. The spin-reorientation temperatures, T_{SR}, of the $x = 1/3, 0.37$ and $x = 1/2$ samples are indicated.

$x = 0.275$ and $T_0 = 10\,\mathrm{K}$ also increases with strength of the inducing field (not shown).

Several compositions ($x = 0.2, 0.3, 1/3, 1/2$) were examined to see if a signal could be induced by FCing $\parallel c$. In Figure 5.10 the results of inducing a signal by FCing $\parallel ab$ or $\parallel c$ for $x = 0.2$ and $1/3$ are shown. In all compositions tested any induced signal $\parallel c$ could be explained by a small sample misalignment of the order $\sim 2°$. I also show the result of inducing a signal by FCing $\parallel ab$ and $\parallel c$ in the other commensurately doped composition, $x = 1/2$, in figure 5.11. As with the other compositions a signal is induced $\parallel ab$ but not $\parallel c$.
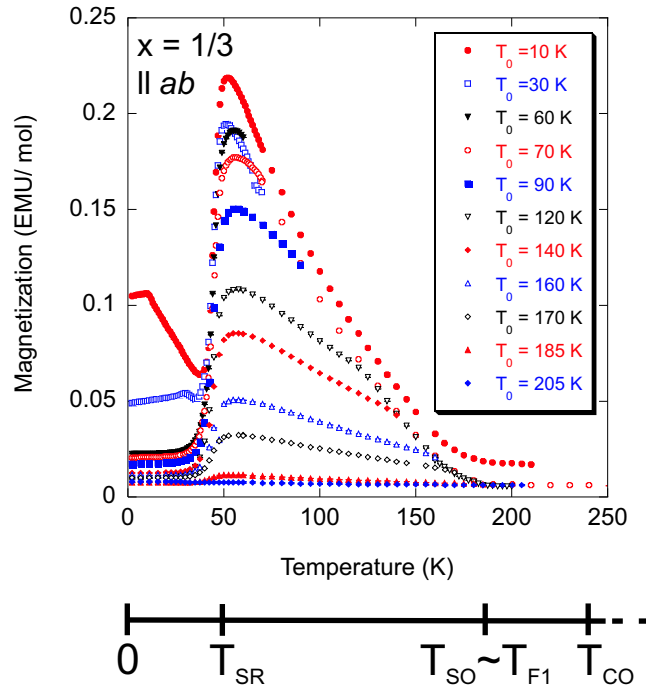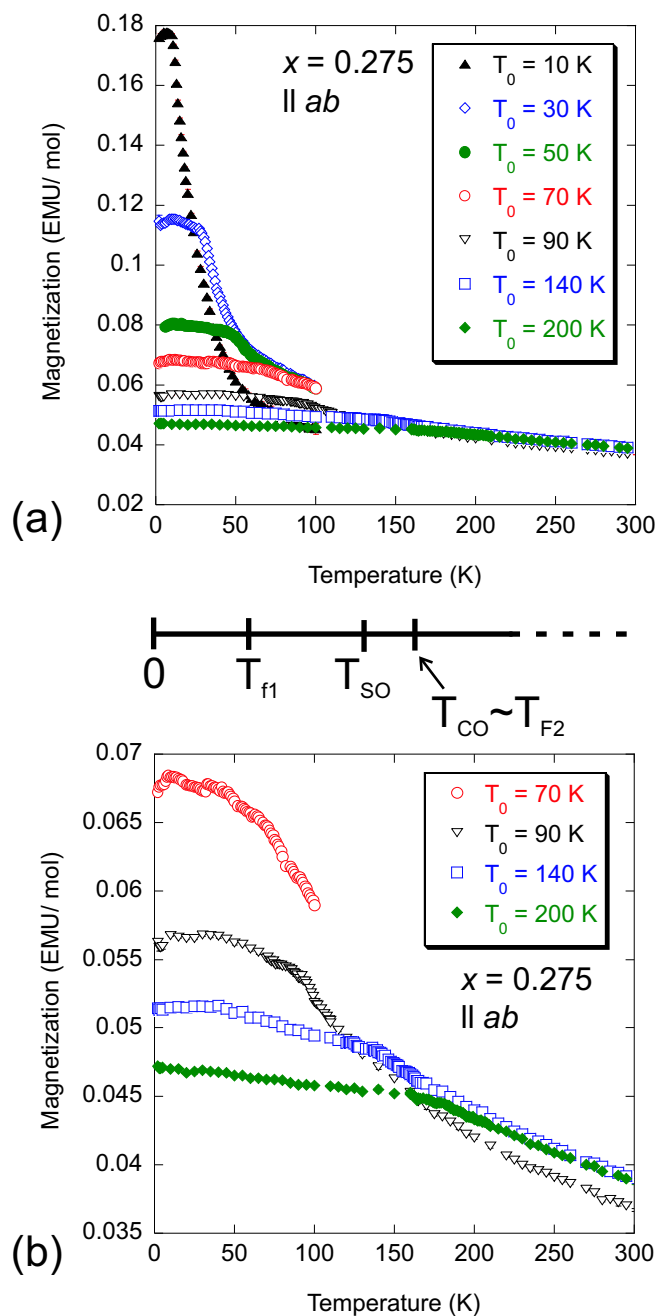
Figure 5.9: (a) The variation of the signal induced by field-cooling $H = 500\,\text{Oe} \parallel ab$ to T_0, indicated in the key, then cooling to $2\,\text{K}$ in zero field, and measuring while warming in zero field. All measurements are for $x = 0.275$. (b) shows the same data as shown in (a), but only contains data with $T_0 \geq 70\,\text{K}$.
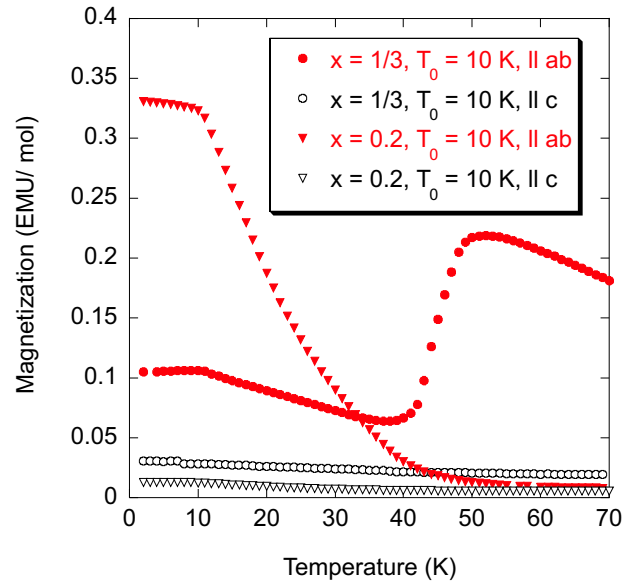
Figure 5.10: The signal induced by field-cooling up to $T_0 = 10\,\mathrm{K}$ in $H = 500\,\mathrm{Oe} \parallel ab$ and $\parallel c$ then cooling to $2\,\mathrm{K}$ in zero field and measuring while warming in zero field, for $x = 0.2$ and $1/3$. The rotating mount was used to obtain data $\parallel c$ for the $x = 1/3$.
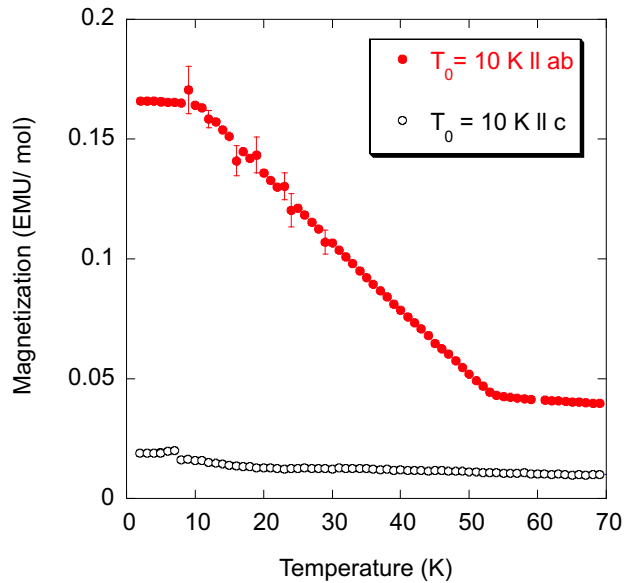
Figure 5.11: The signal induced in the $x = 1/2$ by field-cooling in $H = 500\,\mathrm{Oe}$ $\parallel ab$ or $\parallel c$ to $T_0 = 10\,\mathrm{K}$, setting $H = 0$, then cooling to $2\,\mathrm{K}$ in zero field and measuring while warming. The rotating mount was used to obtain data $\parallel c$.

5.4 Discussion

A common feature of all the La$_{2-x}$Sr$_x$NiO$_{4+\delta}$ compounds we have studied here is the 2-D magnetic irreversibility, with a large irreversibility at low temperatures, $< T_{F1}$, and a small irreversibility that persists until $T_{F2} \sim T_{CO}$ (see Fig.5.2 and Fig.5.3). The data show slight, but possibly important variations from this simple trend. First of all for the $x = 1/3$ compound $T_{F1}(1/3) \sim T_{SO}$, which is significantly larger than in any other compound, an enhancement perhaps due to the pinning effect of commensurate charge-ordering to the crystal lattice[34, 36, 39, 50, 57]. Above T_{F1} the magnetic irreversibility in the $x = 0.37$ sample is notably larger than in any other compound. This does not appear to be due to this composition being close to the commensurate $x = 1/3$ doping level, as the $x = 0.3$ does not have as large a magnetic irreversibility above T_{F1}. For materials with long range charge order $0.2 < x \leq 0.4$[34, 45, 42], we observe a trend in T_{F2} relative to T_{CO}. For the two compounds $x = 0.4, 0.37$ we observe $T_{F2} > T_{CO}$, but in the other materials $T_{F2} < T_{CO}$. This could be linked to the crossover behaviour observed in La$_{2-x}$Sr$_x$NiO$_4$ when the material is doped $x \leq 1/3$ or when doped $x > 1/3$[34, 36, 39, 50]. I also note that in the ZFC-FC measurements of Fig. 5.3 (e) for the $x = 1/2$ the large magnetic irreversibility temperature phase coincides with the spin reorientation transition (see chapter 6). The second high temperature stage of the magnetic irreversibility in $x = 1/2$ shows no variation on warming through T_{SO}, but does reduce in size on warming through T_{ICO}. This at first glance suggests magnetic ordering of Ni^{2+} spins has no effect on the magnetic irreversibility we have observed. However the recent μSR measurements by S. Blundell et $al.$[56] indicate that short range magnetic ordering of Ni^{2+} sites occurs below T_{ICO}, therefore magnetic ordering may significantly effect the observed magnetic irreversibility.

In figure 5.5 we recorded the peak temperatures of the ZFC magnetization to be $\sim$ 10 K for $\delta = 0.11$ and $0.225 \leq x \leq 0.4$ samples, but the peak temperature is higher for the $x = 0.1, 0.2$ and 1/2 samples. For the $x = 0.2$[42] and 1/2[38, 89] the ordering differs from other compositions by being relatively short ranged. These differences could be connected. Lack of knowledge on the ordering of the $x = 0.1$ prevents any discussion on this material.

Our work does raise an important question: what causes the 2-D magnetic irreversibility in La$_{2-x}$Sr$_x$NiO$_{4+\delta}$? Anomalously the charge ordering correlation lengths are known to be shorter than the spin ordering correlation lengths in LSNO, see for example reference [34]. In theoretical work by Schmalian and Wolynes[90] it was shown that stripe systems with competing interactions on different length scales inevitably lead to a transition to a stripe glass phase. This stripe glass state would have metastable states which would lead to slow relaxation rates, just like the remanent magnetization signal we observe in Fig. 5.6. To visualize one possibility as to why different length scales could cause a glassy state, consider the finite length of the charge stripes[42]: the spins order over a longer range than the charges, so the spin order extends beyond the ending of the charge stripe. Remembering that the charge stripes are spin antiphase domain walls, we have beyond the end of the charge stripe two antiphase spin domains meeting, and the competition between the two domains will lead to spin frustration, i.e. glassy behaviour. This offers an explanation as to why the second part of the magnetic irreversibility persists to approximately the charge-ordering temperature.

There are other possibilities for the cause of the magnetic irreversibility. The spins of the Ni^{2+} are ordered at low temperatures and as such seem unlikely to cause the magnetic irreversibility observed, but the spin domains are finite in size. So the magnetic

irreversibility could be due to reorientation of differently aligned spin domains. Alternatively, the spins of the holes in the charge stripes have not been observed to order, so the magnetic irreversibility could be a 'spin glass' freezing of the Ni^{3+} spins in the charge stripes. Theoretical modelling of these spins as a 'spin glass' would need to take account of i) the strong interaction strength between ordered Ni^{2+} sites that occurs across the charge stripes [49], and ii) the spins of the charge stripes showing one dimensional antiferromagnetic correlations with the spin direction pointing preferentially out of the ab plane, see chapter 7.

I have stated the magnetic irreversibility to be spin glass like, but paramagnetic materials and ferromagnetic materials with small domain sizes also display magnetic irreversibility. However, LSNO is well known not to show remnant magnetization in magnetic hysteresis loops, indicating a lack of ferromagnetism. If these materials were spin glasses, a.c. susceptibility measurements would show a frequency dependence of the imaginary part of the susceptibility, but in these materials a.c. susceptibility measurements show no frequency dependence (not shown). Clearly the magnetic irreversibility in LSNO has certain properties that do not behave in the same manner as spin glasses.

In discussing the 'memory' effects I choose first of all to deal with the general trends, then to discuss the unusual trends of the $\delta = 0.11$, $x = 1/2$ and then the very unusual $x = 1/3$. To aid the description of the data I will refer to the induced signals being caused by the alignment of 'spins'. As I make no assumption on the origins of these 'spins' my interpretation of the induced signals is not in any way biased. This qualitative description of the general trends I base on a very recent theoretical paper by P. Sibani and H. J. Jensen on how a spin glass remembers[91].

In Fig. 5.6 I have shown the remnant signal induced by application of a field at a fixed temperature in the $x = 1/3$, this remnant signal is typical of all the LSNO materials studied here. After the field is switched off the induced signal decays as thermal fluctuations perturb the system. The thermal fluctuations 'quake' the spins out of their induced metastable states into metastable states of lower energy and magnetization. In the lower metastable state the population of spins grows and the energy barrier for the state is larger as the state has a lower energy. To quake the system out of the new state a more energetic thermal fluctuation has to overcome the larger energy barrier for more spins, such a fluctuation occurs far less than the fluctuations which decayed the spins into this state. In this way each new stable state needs a larger quake to be excited out of its present metastable state into another metastable state with lower energy. The likelihood of thermal fluctuations causing such a quake exponentially decreases with increasing energy required for that quake, so the induced magnetization decays exponentially with time. This explains the relatively fast decaying signal at early times. At later times the thermal fluctuations are not large enough to quake the system out of the induced old age metastable state, so the signal practically stops decaying.

More thermal energy is required to 'quake' the system out of the old age metastable state back into the true ground state; more energy can be provide by heating the sample. The behaviour of the memory effects in Fig. 5.8 for the general doping level can be explained in this way. After the field is switched off at $T_0 = 10\,\mathrm{K}$ the induced signal rapidly decays into the old age metastable state by quakes from the thermal fluctuations, in the manner shown in Fig. 5.6. Cooling the sample to $2\,\mathrm{K}$ reduces the thermal energy of the system, freezing the induced magnetization. On heating up to $10\,\mathrm{K}$ the sample still has less thermal energy, so no quakes are large enough to reduce the induced magnetization.

However, on heating above $10\,\mathrm{K}$ the thermal energy increases and the systems rapidly receives quakes that reduce the induced magnetization to the old age metastable state for the new temperature. In this way the small increases in temperature act to cause an exponential decrease of the induced magnetization. This type of induced signal is called Thermo Remnant Magnetization (TRM). In Fig. 5.9 for the $x = 0.275$, apart from the small increase in strength below $10\,\mathrm{K}$ the TRM signal is observed to be near constant until T_0, where it decays away in the same manner as $T_0 = 10\,\mathrm{K}$ for the general doping level. The fact that the lower T_0 is the larger the TRM is, is not surprising, as when T_0 is lower the thermal energy and hence fluctuations at T_0 are smaller, so the TRM can stabilize in an energetically higher metastable state as the thermal fluctuations cannot quake the system to a lower energy ground state. The fact that the larger the field used to induce a signal by field cooling the larger the induced signal is, suggests that a larger field produces metastable states with larger energy barriers. To a rough approximation we observe a large TRM for $T_0 < T_{\mathrm{F1}}$ and a small TRM for $T_0 > T_{\mathrm{F1}}$, until $\sim T_0 > T_{\mathrm{F2}}$. This is a good indication that the cause of the TRM is the same as that of the irreversible magnetization.

The behaviour of the $\delta = 0.11$ compound in Fig. 5.8 is unusual in that the TRM decays rapidly over a small temperature range of no more than $5\,\mathrm{K}$. This could be an indication of an as yet unknown transition occurring at $\sim 15\,\mathrm{K}$ and should be investigated by other techniques. For the $x = 1/2$ the behaviour is typical of the other doping levels apart from at the spin reorientation $T_{\mathrm{SR}} = T_{\mathrm{F1}} \approx 57\,\mathrm{K}$. At the temperature of the spin reorientation the decay of the TRM shows an abrupt change: in some way this transition causes a striking change to the memory of this material. Although the $\delta = 0.11$ and $x = 1/2$ show variations from the normal trend, in both materials an increase in energy leads to a loss

of the TRM of the material.

In the $x = 1/3$ we observe a very different behaviour to the other materials (see Fig. 5.7). On warming through the spin reorientation at $50\,\text{K}$ the TRM is observed to dramatically increase by an order of magnitude in the case of $T_0 = 60 - 90\,\text{K}$. For TRM effects, increases in temperature should cause loss of magnitude in the induced magnetization. Complex magnetization effects have been observed in interacting magnetic nanoparticles[92], but the observation of complex memory behaviour in those systems have been shown to be relatively simple in origin and can come from a paramagnetic ground state[93]. Hence, when dealing with unusual memory effects in magnetic materials it is best to be cautious about their origin. In the $x = 1/3$ sample studied here the TRM seems to be suppressed in the low temperature spin orientation (LTSO): the material appears to freeze a memory of the temperature – field history in the high temperature spin orientation (HTSO). How this is achieved is unclear, the memory of the TRM in the HTSO must be stored elsewhere in the LTSO.

The suppression of the induced signal in the LTSO is not restricted to the $x = 1/3$. In Fig. 5.8 the $x = 0.37$ shows a small increase in the TRM on warming to $10\,\text{K}$, as does the $x = 0.275$ (Fig. 5.9). Again this suppression seems to be linked to the spin reorientations in these materials (see chapter 6). The increases of the TRM signal with temperature in the $x = 0.275$ and 0.37 are far smaller than in the $x = 1/3$, possibly indicating commensurate enhancement in the $x = 1/3$. This makes the behaviour of the TRM in the LTSO of the $x = 1/2$ unusual; in the $x = 1/2$ there is no suppression of the TRM in the LTSO.

To summarize, magnetization measurements of La$_{2-x}$Sr$_x$NiO$_{4+\delta}$ for $0 \leq x \leq 1/2$

exhibit charge and spin ordering features, with the exception of the $\delta = 0.11$ and $x = 0.1$ samples. All doping levels studied show a two component ZFC-FC splitting when the field is in the ab plane, with a large splitting at low temperatures and a small splitting that persists to approximately the charge-ordering temperature. This ZFC-FC splitting is characteristic of magnetic irreversibility. The large low temperature ZFC-FC splitting was observed to persist up to the spin ordering temperature in the $x = 1/3$. Thermo Remnant Magnetization (TRM) signals were observed for all the doping levels when $H \parallel ab$, and the onset temperature of the TRM is observed to correlate with the magnetic irreversibility. Anomalously, this TRM signal is observed to be heavily suppressed in the low temperature spin orientation of the $x = 1/3$ crystal and to a lesser extent in the $x = 0.275, 0.37$ samples.

Chapter 6

Spin reorientation transition in La$_{2-x}$Sr$_x$NiO$_{4+\delta}$

In this chapter I present neutron diffraction experiments on La$_{2-x}$Sr$_x$NiO$_{4+\delta}$[89, 94]. I will first highlight results from our magnetization study of single crystals of La$_{2-x}$Sr$_x$NiO$_4$, which showed a previously unidentified transition in the $x = 1/2$ and 0.37 doping levels. The discovery of this unidentified transition instigated a full characterization of the magnetic order of single crystals of $x = 1/2$ and 0.37 by neutron diffraction.

The temperature dependence of the magnetic order Bragg peaks suggested that the unidentified magnetic transition was a spin reorientation in the ab pane of the crystals, where on cooling the spins rotate away from the charge-stripe direction. We confirmed this interpretation by employing polarized-neutron diffraction to determine the temperature variation of the spin orientation in the $x = 1/2$ and 0.37.

Having determined the existence of a spin orientation in the $x = 1/2, 0.37$ and with knowledge of the existence of a previously observed spin reorientation in a $x = 1/3$ doped sample[35], we investigated the possible existence of a spin reorientation in other doping

levels. We achieved this by studying the magnetic order of single crystals of $x = 0.275$ and 0.4 by unpolarized-neutron diffraction. From the temperature dependence of the magnetic order peaks we inferred that a spin reorientation does occur in the $x = 0.275$ and 0.4 in the same manner as in the $x = 0.5, 0.37$. This investigation leads us to the conclusion that all doping levels for $0.275 \leq x \leq 0.5$ undergo on a spin reorientation at $\sim 15\,\text{K}$ or at $\sim 50\,\text{K}$ for the commensurately doped $x = 1/3$ and $x = 1/2$, with the spin reorientation being significantly larger in the $x = 1/2$.

6.1   Magnetization Measurements

Magnetization data were collected with a superconducting quantum interference device (SQUID) magnetometer (Quantum Design), with the field applied parallel to the ab plane of the crystal. The crystals used for the magnetization measurements had typical dimensions $\sim 5 \times 5 \times 2\,mm^3$. The oxygen content of the $x = 0.275, 0.37$ and $1/2$ crystals was determined by thermogravimetric analysis to be close to stoichiometric, i.e. $\delta \approx 0$ (see chapter 4). We carried out d.c. measurements either by cooling the sample in an applied field of 500 Oe (FC), or by cooling in zero field then measuring while warming in a field of 500 Oe (ZFC).
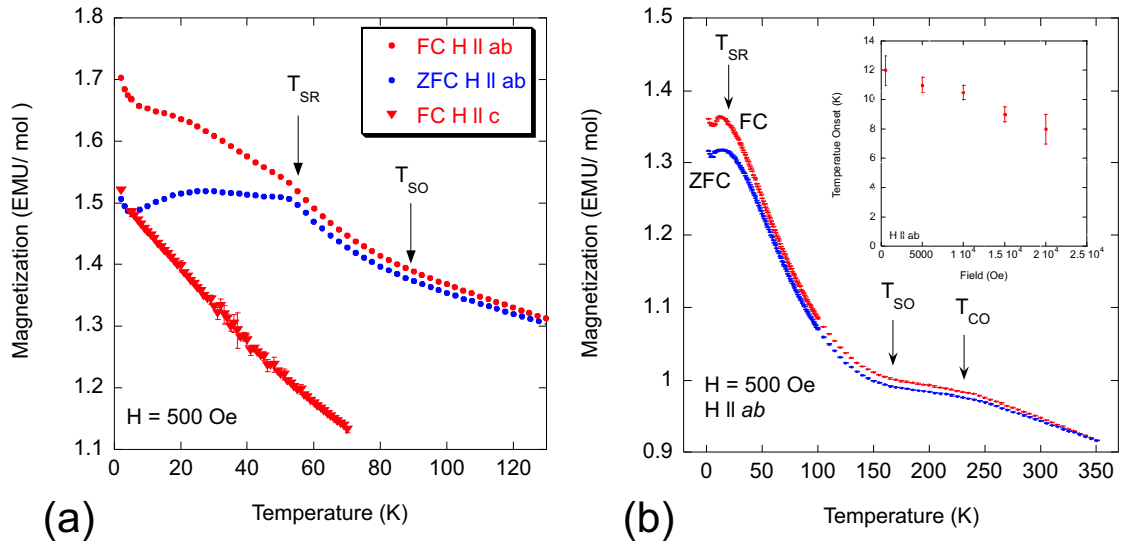
Figure 6.1: FC and ZFC magnetization data for (a) $La_{3/2}Sr_{1/2}NiO_4$ and (b) $La_{1.63}Sr_{0.37}NiO_4$. Arrows indicate the charge-ordering temperature, T_{CO}, spin-ordering temperature, T_{SO}, and the spin-reorientation temperature, T_{SR}, determined separately by neutron diffraction. The inset of (b) shows the field dependence of the onset temperature of the anomaly in the magnetization data for $x = 0.37$.

Figure 6.1(a) shows the temperature variation of the FC and ZFC magnetization $\parallel ab$ and FC $\parallel c$ for a $x = 1/2$ sample. A small change in slope at $90 \pm 5\,K$ marks the spin

ordering temperature, in agreement with previous observations[34]. A clearer anomaly is seen at $T_{\mathrm{SR}} = 57\,\mathrm{K}$, where the FC and ZFC curves sharply separate. Below $5\,\mathrm{K}$ both the FC and ZFC curves begin to rise for reasons that are not yet understood, but could be due to a small amount of paramagnetic impurity in the crystal. We measured the FC magnetization parallel to the crystal c direction and found no anomaly around T_{SR}, thus indicating that the transition involves the in-plane components of the spins. In figure 6.1(b) we show the variation of the FC and ZFC magnetization for $x = 0.37$. A subtle change of slope at $T_{\mathrm{CO}} = 230 \pm 10\,\mathrm{K}$, marks the charge-ordering temperature, with a more pronounced gradient change at $T_{\mathrm{SO}} = 170 \pm 10\,\mathrm{K}$ marking the spin-ordering temperature (defined later from neutron diffraction). In the $x = 0.37$ material there is a large FC–ZFC difference below $\sim 50\,\mathrm{K}$ and a much smaller difference that persists to T_{CO} with a slight widening around T_{SO} (see chapter 5.2). We observe a small but sharp drop in the FC magnetization below $\sim 12\,\mathrm{K}$, indicating an unidentified transition. The inset of figure 6.1(b) shows the field dependence of this feature, which can be seen to decrease when increasing the applied field. As I will show, this feature along with the anomaly at $T_{\mathrm{SR}} = 57\,\mathrm{K}$ in the $x = 1/2$ material correspond to a spin reorientation transition.

Figure 6.2 shows the variation of FC and ZFC magnetization for the $x = 0.275$ and $x = 0.4$. Like $x = 0.37$ and $1/2$, both these materials are observed to have irreversible magnetic behaviour. The ZFC magnetization of the $x = 0.275$ crystal has a rounded maximum at $\sim 10\,\mathrm{K}$. For $x = 0.4$ there is no maximum, but the increase in magnetization with decreasing temperature first slows down and then begins to rise sharply below $5\,\mathrm{K}$. The increase below $5\,\mathrm{K}$ could be due to a small amount of paramagnetic impurity in the crystal.
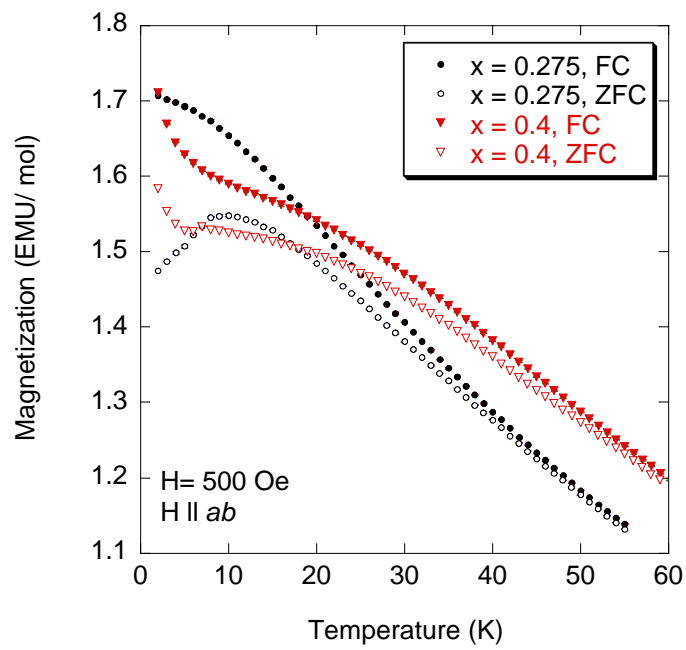
Figure 6.2: FC and ZFC magnetization data for La$_{2-x}$Sr$_x$NiO$_4$ $x = 0.275$ and 0.4.

6.2   Neutron Diffraction Measurements

The polarized neutron experiments were performed on the triple-axis spectrometer IN20 at the Institut Laue-Langevin. The energies of the incident and elastically scattered neutrons were selected by Bragg reflection from an array of Heusler alloy crystals. The data were obtained with initial and final neutron wavevectors of $2.66\,\text{Å}^{-1}$. A PG filter was present between the sample and the analyzer to suppress scattering of higher-order harmonics. Some additional measurements on the $x = 1/2$ crystal were carried out with the initial and final neutron wavevectors of $3.54\,\text{Å}^{-1}$. For a $k_f = 2.66\,\text{Å}^{-1}$ the wavevector resolution in the scattering plane was $0.03\,\text{Å}^{-1}$ and the out of plane resolution was $0.13\,\text{Å}^{-1}$, whereas for a $k_f = 3.54\,\text{Å}^{-1}$ the resolution in the scattering plane was $0.04\,\text{Å}^{-1}$ and the out of plane resolution was $0.11\,\text{Å}^{-1}$. The unpolarized neutron experiments were performed on the triple-axis spectrometer RITA-II at SINQ at the Paul Scherrer Institut. The energies of the incident and elastically scattered neutrons were selected by Bragg reflection from a PG crystal. The data were obtained with initial and final neutron wavevectors of $1.55\,\text{Å}^{-1}$, and a Be filter operating at $77\,\text{K}$ was present between the sample and the analyzer to suppress scattering of higher-order harmonics. For the measurements on RITA II the in plane wavevector resolution was $0.02\,\text{Å}^{-1}$.

For $x = 0.275, 0.37, 1/2$ single crystal rods of 7–$8\,\text{mm}$ diameter and $\sim 40\,\text{mm}$ in length were used, and for $x = 0.4$ the crystal was a slab of dimensions $\sim 15 \times 10 \times 4\,\text{mm}^3$. In this work we describe the structural properties of LSNO with reference to a tetragonal unit cell, with unit cell parameters $a \approx 3.8\,\text{Å}$, $c \approx 12.7\,\text{Å}$. The samples were mounted with the [001] and [110] crystal directions in the horizontal scattering plane. Scans were performed in reciprocal space either parallel to the $(h,\,h,\,0)$ direction at constant l, or parallel to

the $(0, 0, l)$ direction at constant h.

Our elastic neutron scattering study began by examining the $x = 0.37, 1/2$ doping levels by polarized-neutron diffraction. Initially, the neutron polarization $\mathbf{P}$ was arranged to be parallel to the scattering vector $\mathbf{Q}$, maintained by an adjustable guide field of a few mT at the sample position. In this configuration a neutron's spin is flipped during an interaction with electronic magnetic moments, but remains unchanged when scattered by a non-magnetic process, e.g. a lattice distortion. Thus by measuring the spin-flip (SF) and non-spin-flip (NSF) channels one can identify whether observed scattering is magnetic or not in origin.

In the $x = 0.37$ material magnetic order Bragg peaks were observed at $(h + 1/2 \pm \varepsilon/2, h + 1/2 \pm \varepsilon/2, l)$ positions for all integer l. This can be seen in figure 6.3(a), which shows the SF scattering for a scan parallel to $(h, h, 0)$ for $l = 5$ at $T = 2\,\mathrm{K}$. The peak position corresponds to $\varepsilon = 0.3554 \pm 0.0002$, consistent with previous measurements [34].

Figure 6.3(b) shows the NSF scattering from $x = 0.37$ for the same scan as Fig. 6.3(a). The scan contains 2 weak peaks, one at $h = 0.646 \pm 0.001$ corresponding to charge ordering with an incommensurability of $\varepsilon = 0.354 \pm 0.001$, and the other at $h = 0.678$ corresponding to magnetic ordering. The latter appears in the NSF channel due to imperfect polarization of the neutron beam. We searched for the charge order peak at other equivalent $(0.646, 0.646, l)$ positions, but only at $l = 3$ and 5 was there a measurable peak. From the temperature dependence of the charge peak in Fig. 6.3(b) we found $T_{\mathrm{CO}} \approx 230\mathrm{K}$. By performing scans parallel to $(h, h, 0)$ we were able to obtain the in-plane charge-order correlation length perpendicular to the stripe direction of $70 \pm 6\,\text{Å}$. This compares with a correlation length of $49 \pm 5\,\text{Å}$ along the c axis. These results show
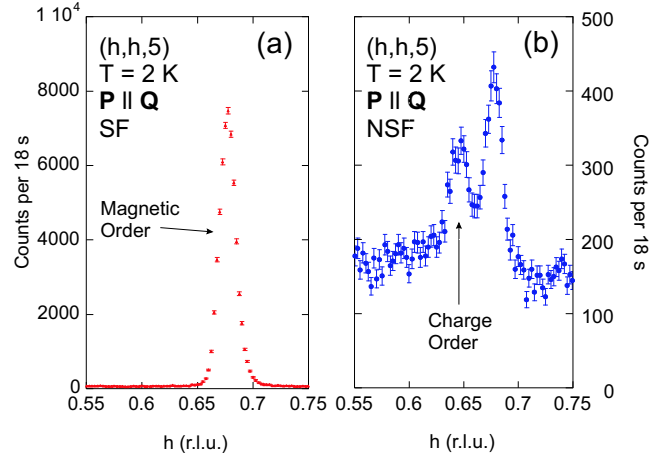
Figure 6.3: (a) The spin flip (SF) diffraction channel for a scan parallel to $(h, h, 0)$ for $l = 5$ for La$_{1.63}$Sr$_{0.37}$NiO$_4$ at $T = 2$ K. This peak corresponds to the magnetic order peak, and is centred at $h = 0.678$. (b) The non-spin flip diffraction for the same scan. The arrow indicates the charge-order Bragg peak. The second peak is diffraction from the magnetic order peak observed in the NSF channel due to the imperfect spin polarization of the neutron beam.

that the charge order is relatively three-dimensional.

For the $x = 1/2$ sample we observed spin-order diffraction peaks at $(h+1/2\pm\varepsilon/2, h+1/2\pm\varepsilon/2, l)$ positions with l odd and $\varepsilon = 0.445 \pm 0.005$. Figure 6.4 shows a scan parallel to $(0, 0, l)$ for both SF and NSF scattering. The widths of the magnetic peaks in the SF scan convert to a correlation length along the c axis of 16.4 ± 0.3 Å. For comparison, the in-plane correlation length in the direction perpendicular to the stripes is 78.3 ± 1.3 Å. There were no peaks at $l =$ even positions, as can be seen in figure 6.4. There were also no spin-order peaks at $(h\pm1/4, h\pm1/4, l)$ positions, confirming the lack of any commensurate Fourier component in the spin ordering, in agreement with the observations of Kajimoto et al.[38].

We observed charge-order diffraction in the vicinity of the $(1.5, 1.5, l)$ line in reciprocal space for the $x = 1/2$ compound. At $T = 10$ K the peak shape observed in $(h, h, 0)$ scans
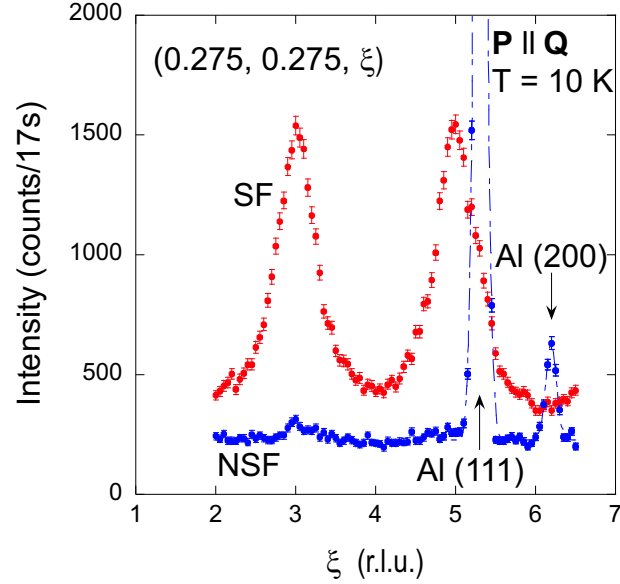
Figure 6.4: Spin-flip (SF) and non-spin-flip (NSF) diffraction from La$_{3/2}$Sr$_{1/2}$NiO$_4$ at $T = 10$ K. The scan is parallel to $(0, 0, l)$ and passes through the magnetic order peak $(0.275, 0.275, 1)$. No correction has been made for the imperfect polarization of the neutron beam. The sharp peaks in the NSF channel at $l \approx 5.3$ and 6.2 are due to diffraction from the Al sample mount.

was consistent with that observed by Kajimoto *et al.*, with a central peak at $h = 1.5$ and two satellites at $h \approx 1.45$ and 1.55. We observed no variation of this scattering with l over a single Brillouin zone, showing that both the commensurate and incommensurate components of charge ordering are completely two-dimensional.

Figure 6.5 shows a scan performed on the $x = 0.37$ parallel to $(0, 0, l)$ through the magnetic order peaks, this is similar to the scan on the $x = 1/2$ that is shown in Fig. 6.4. As with the $x = 1/2$ sample the widths of the peaks in this scan relate to the correlation length along the c-axis, however we observed that the correlation lengths for even and odd l differ by a factor ≈ 2. That is, for even l we obtain a correlation length of $53.2 \pm 1.4\,$Å and for odd l we obtain a correlation length $108 \pm 2\,$Å . We performed scans parallel to $(h, h, 0)$ on odd l peaks, for which we obtained an in-plane correlation length
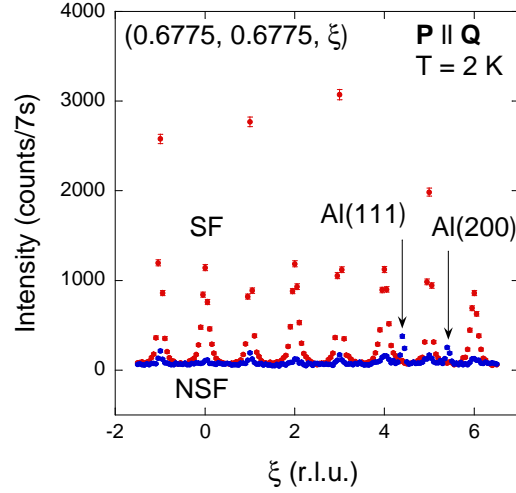
Figure 6.5: Spin-flip (SF) and non-spin-flip (NSF) diffraction from La$_{1.63}$Sr$_{0.37}$NiO$_4$ at $T = 2$ K. The scan is parallel to (0, 0, l) and passes through the magnetic-order peak (0.6775, 0.6775, 1). No correction has been made for the imperfect polarization of the neutron beam. The additional peaks in the NSF channel at $l \approx$ 4.4 and 5.4 are due to diffraction from the Al sample mount.

perpendicular to charge stripe direction of 112.6 ± 1.1 Å .

The intensities of the even and odd l magnetic peaks were discussed in work on La$_2$NiO$_{4+\delta}$, by P. Wochner et $al.$[48]. For a commensurate stripe spin-ordering, such as $\varepsilon = 1/3$, the stripes stack in a body centred arrangement and only the odd l magnetic peaks are observed, with the systematic absence of the $l =$ even peaks. However, for incommensurate spin-ordering with the stripes either pinned to the Ni or O sites[69], perfect body-centred stacking cannot be achieved. The disorder thus created, along with the additional disorder introduced due to differing Coulomb interactions between the ab layers, result in the presence of $l =$ even peaks. Hence, $l =$ odd peaks have a long correlation length as they come from the ideal long range body-centred stacking, whereas $l =$ even peaks are a result of the disorder created on the smaller length scale of the non-ideal stacking.

In figure 6.6(a) I show the ideal checkerboard charge-ordered arrangement for the $x = 1/2$,
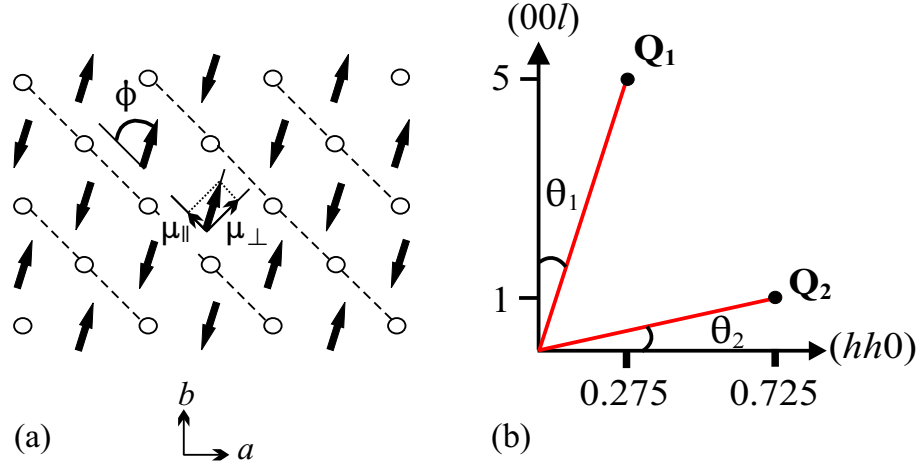
Figure 6.6: (a) Ideal checkerboard 2-D charge ordering in the ab plane. Circles represent holes residing on Ni sites, while the solid arrows represent the spins of the Ni^{2+} sites. Dashed lines indicate the charge domain walls common to both checkerboard and stripe ordering. The commensurate spin ordering shown here is not realized in practise in La$_{3/2}$Sr$_{1/2}$NiO$_{4+\delta}$. The observed spin order in La$_{3/2}$Sr$_{1/2}$NiO$_{4+\delta}$ is similar to that shown, but is actually incommensurate in the direction perpendicular to the stripes. The components of the ordered moment parallel ($\mu_\parallel$) and perpendicular ($\mu_\perp$) to the stripe direction are shown, and ϕ denotes the angle between the spin axis and the stripe direction. (b) Diagram of the (h, h, l) plane in reciprocal space. $\mathbf{Q}_1$ and $\mathbf{Q}_2$ are the scattering vectors of the two magnetic peaks investigated in this work.

showing the spin components parallel to ($\mu_\parallel$) and perpendicular to the stripe direction ($\mu_\perp$), along with the angle ϕ between the spins and the charge stripes. In practise this arrangement is not achieved. The charges order in the ideal checkerboard arrangement at $\sim$480 K but below $T_{\mathrm{ICO}}\sim$ 180 K an incommensurate charge-stripe ordering phase coexists with the checkerboard ordering[38]. Figure 6.7(a) shows the temperature dependence of the integrated intensity of two magnetic reflections for $x = 1/2$, $\mathbf{Q}_1 = (0.275,0.275,5)$ and $\mathbf{Q}_2 = (0725,0.725,1)$, measured in scans parallel to $(h,h,0)$. The spin ordering transition is seen to be rather sluggish, but a sharpening of the peaks below $T_{\mathrm{SO}} \simeq 80$ K (not shown) suggests that this is where long-range ordering extending over many unit cells sets in.

However short-range correlations persist above $100\,\mathrm{K}$. On cooling below T_{SO}, the peak at $\mathbf{Q}_1$ increases monotonically, while that at $\mathbf{Q}_2$ first increases, then reaches a maximum at $\sim 60\,\mathrm{K}$, then decreases again. This anomalous behaviour correlates with the transition observed in the magnetization, Fig. 6.1(a). To understand this behaviour we must recall that magnetic neutron diffraction is sensitive to spin components perpendicular to $\mathbf{Q}$. As shown in figure 6.6(b), $\mathbf{Q}_1$ is approximately parallel to $(0, 0, l)$ while $\mathbf{Q}_2$ is approximately parallel to $(h, h, 0)$. Therefore, to a good approximation, the scattering at $\mathbf{Q}_1$ is from the total in-plane spin moment, irrespective of its direction, while that at $\mathbf{Q}_2$ comes mainly from the spin components parallel to the stripes and along the c axis. The data in fig. 6.7(a) therefore imply that below $\sim 57\,\mathrm{K}$ the spins rotate away from the stripe direction.

To fully analyze the direction of the spins over this temperature range in the $x = 0.5$, we varied the direction of the neutron polarization $\mathbf{P}$ relative to the scattering vector $\mathbf{Q}$. Three configuration were used: 1) $\mathbf{P} \parallel \mathbf{Q}$, 2) $\mathbf{P} \perp \mathbf{Q}$ but in the scattering plane, and 3) $\mathbf{P} \perp \mathbf{Q}$ but out of the scattering plane. (Recall that [110] and [001] are the crystal directions in the scattering plane.) As mentioned before, neutrons scatter via magnetic interactions from spin components perpendicular to $\mathbf{Q}$, and SF scattering is due to spin components perpendicular to $\mathbf{P}$. Therefore, analysis of configurations 1), 2) and 3) leads to the direction of the ordered moment[1]. Table 6.1 summarizes the relations between the observed intensities at $\mathbf{Q}_1$ and $\mathbf{Q}_2$ and the ordered spin components parallel ($\mu_{\parallel}$) and perpendicular ($\mu_{\perp}$) to the stripe direction (see figure 6.6(a)), and parallel to the c axis (μ_c) .

We corrected the data to take into account the different background count rates in the SF and the NSF channels, and to correct for the imperfect spin polarization of neutron beam.

---

[1]Actually, 2 out of the 3 configurations are sufficient.
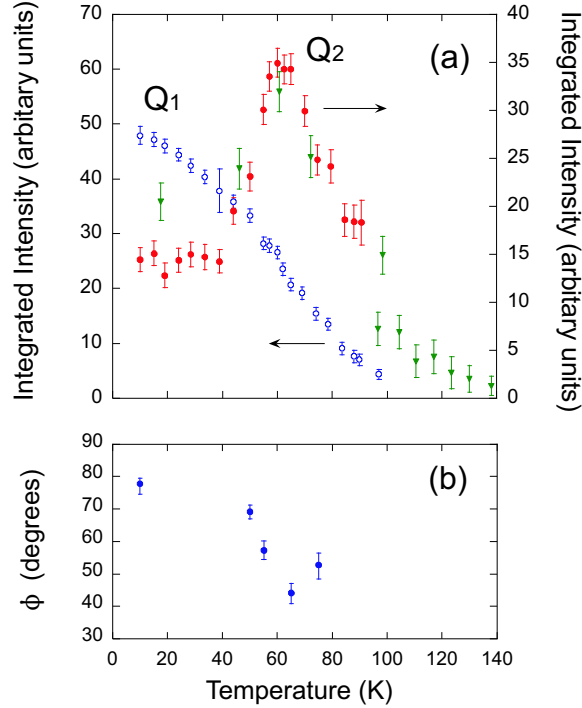
Figure 6.7: (a) The peak intensities for $x = 1/2$ of the spin peaks $\mathbf{Q}_1 = (0.275, 0.275, 5)$ and $\mathbf{Q}_2 = (0.725, 0.725, 1)$ — see figure 1(b). Circle symbols represent data taken with a neutron wavevector of $3.54\,\text{\AA}^{-1}$ and triangles represent $2.66\,\text{\AA}^{-1}$. Filled symbols are data taken at $\mathbf{Q}_2$ and unfilled symbols at $\mathbf{Q}_1$, with the arrows indicating the relevant scales for each $\mathbf{Q}$. (b) The temperature dependence of the angle ϕ between the spin axis and the stripe direction obtained from polarized-neutron analysis.

The latter was calculated from the flipping ratio 18.5 ± 1.8 measured on a magnetic Bragg peak (see chapter 3.3.2).

A full analysis of the intensities at the $\mathbf{Q}_1$ and $\mathbf{Q}_2$ points determined the spin orientations at $T = 10\,\text{K}$ and $T = 65\,\text{K}$. These analysis showed that the non-magnetic (NM) and μ_c count rates were zero, to within error for both temperatures. Thus, it is reasonable to assume that the spins lie within the ab plane over the whole temperature range, consistent with the lack of any anomaly observed at T_{SR} in the magnetization data measured with $\mathbf{H} \parallel c$. At the other temperatures we deduced the spin orientation within the ab plane

	P configuration		**Q**$_1$	**Q**$_2$
1)	**P** $\parallel$ **Q**	SF	$\mu_\perp^2 \cos^2\theta_1 + \mu_\parallel^2 + \mu_C^2 \sin^2\theta_1$	$\mu_\perp^2 \sin^2\theta_2 + \mu_\parallel^2 + \mu_C^2 \cos^2\theta_2$
		NSF	NM	NM
2)	**P** $\perp$ **Q**	SF	$\mu_\parallel^2$	$\mu_\parallel^2$
	(**P** in horiz plane)	NSF	$\mu_\perp^2 \cos^2\theta_1 + \mu_C^2 \sin^2\theta_1 +$NM	$\mu_\perp^2 \sin^2\theta_2 + \mu_C^2 \cos^2\theta_2 +$NM
3)	**P** $\perp$ **Q**	SF	$\mu_\perp^2 \cos^2\theta_1 + \mu_C^2 \sin^2\theta_1$	$\mu_\perp^2 \sin^2\theta_2 + \mu_C^2 \cos^2\theta_1$
	(**P** vertical)	NSF	$\mu_\parallel^2 +$NM	$\mu_\parallel^2 +$NM

Table 6.1: Expressions for the intensity of SF and NSF scattering for different orientations of the neutron polarization **P** relative to the scattering vector **Q** (NM is the non-magnetic scattering).

from one **Q** position ($T = 55$ K from **Q**$_1$, $T = 50$ and 75 K from **Q**$_2$.) From these data we find that the spins reorientate from an angle of $52 \pm 4°$ to the stripe direction at $T = 75$ K, to $78 \pm 3°$ at $T = 10$ K, as shown in figure 4(b). The transition is seen to occur quite rapidly between 50 and 65 K, although the reorientation is not complete at 50 K. This spin reorientation is similar to the spin reorientation seen below 50 K for $x = 1/3$[35].

For the $x = 0.37$ we considered the two magnetic Bragg reflections **Q**$_1$ = (0.3225,0.3225,3) and **Q**$_2$ = (0.6775,0.6775,1). As in the $x = 1/2$ sample the scattering at **Q**$_1$ arises mainly from the total in-plane spin moment, while that at **Q**$_2$ comes mainly from the spin components parallel to the stripe direction and along the c axis. Hence, we performed scans in the $x = 0.37$ parallel to (h, h, 0) that pass through **Q**$_2$ at different temperatures to give a first indication as to whether there exists an in-plane spin reorientation like that observed for $x = 1/3$ and $1/2$. Figure 6.8(a) shows the temperature dependence of the magnetic reflection **Q**$_2$. The magnetic ordering transition can be seen to occur at $T_{SO} \simeq$ 170 K. On cooling below T_{SO} the intensity of **Q**$_2$ can be seen to increase monotonically

Figure 6.8: (a) $x = 0.37$ the temperature dependence of the intensity of the magnetic Bragg peak at $\mathbf{Q}_2 = (0.6775, 0.6775, 1)$ — see figure 1(b). (b) The temperature dependence of the angle ϕ between the spin axis and the stripe direction obtained from polarized-neutron analysis.

until it reaches a maximum at $\simeq 20\,\mathrm{K}$, then it is seen to decrease in intensity continuously to our base temperature. This anomalous behaviour correlates well with the transition observed in the magnetization data, Fig. 6.1, and indicates a spin reorientation below $\simeq$ $20\,\mathrm{K}$.

We carried out polarization analysis to determine the temperature dependence of the orientation of the spins in the same way as carried out for the $x = 1/2$ sample. The equations shown in table 6.1 are still valid for $x = 0.37$ and the data was corrected for the slightly non-ideal performance of the polarization elements of the instrument from a flipping ratio of 18 ± 1 measured on the magnetic Bragg peaks.

Polarization analysis of both the $\mathbf{Q}_1$ and the $\mathbf{Q}_2$ Bragg peaks revealed that the moment

lies in the ab plane to within $1°$ in the temperature range $2-71$ K. Having established this, we subsequently assumed the c-axis component to be zero and analyzed the polarization at $\mathbf{Q}_1$ to determine the in-plane moment. From this analysis we determined that the spins rotated from an angle of $37.7 \pm 0.3°$ to the stripe direction at $T = 71$ K to $52.3 \pm 0.2°$ at $T = 2$ K, as shown in Fig. 8.7(b). The transition occurs mainly between 10 and 20 K, but slowly develops from below ~ 50 K.

We performed unpolarized neutron diffraction at equivalent $\mathbf{Q}_1$ and $\mathbf{Q}_2$ positions on the single crystals with $x = 0.275$ and $x = 0.4$, using the instrument RITA-II at SINQ. Figure 6.9 shows the temperature dependence of the $\mathbf{Q}_2$ positions for the $x = 0.275$ and $x = 0.4$ crystals. We found a similar behaviour to the $x = 0.37$ results just described. In particular, the temperature dependence of the $\mathbf{Q}_2 = (0.645, 0.645, 0)$ magnetic Bragg peak for $x = 0.275$, and of the $\mathbf{Q}_2 = (0.685, 0.685, 1)$ magnetic Bragg peak for $x = 0.4$, both have a maximum similar to that shown in Fig. 6.8(a) for $x = 0.37$. By contrast, the intensities of the $\mathbf{Q}_1$ Bragg peaks are almost constant below 20 K. The temperature dependence of the $\mathbf{Q}_2$ intensity is shown on Fig. 6.9 for both $x = 0.275$ and $x = 0.4$. The drop in $\mathbf{Q}_2$ intensity at low temperature implies a spin reorientation in $x = 0.4$ and $x = 0.275$ similar in nature to that in $x = 0.37$.

Unpolarized neutron diffraction cannot accurately determine ϕ without a detailed analysis of the intensities of many diffraction peaks, but we can estimate $\Delta\phi$ from the drop in intensity of the $\mathbf{Q}_2$ peak below $T_{\text{SR}} \sim 15$ K and the value of ϕ for $T > T_{\text{SR}}$, assuming the ordered moment remains in the ab plane and fixed in magnitude in this temperature range. Taking $\phi = 27°$ above T_{SR} for $x = 0.275$[35], and using $\phi = 38°$ for $x = 0.4$ (based on the observations for $x = 0.37$ at 71 K). We find $\Delta\phi \approx 10-15°$ for both $x = 0.275$ and $x = 0.4$, similar to $x = 0.37$.

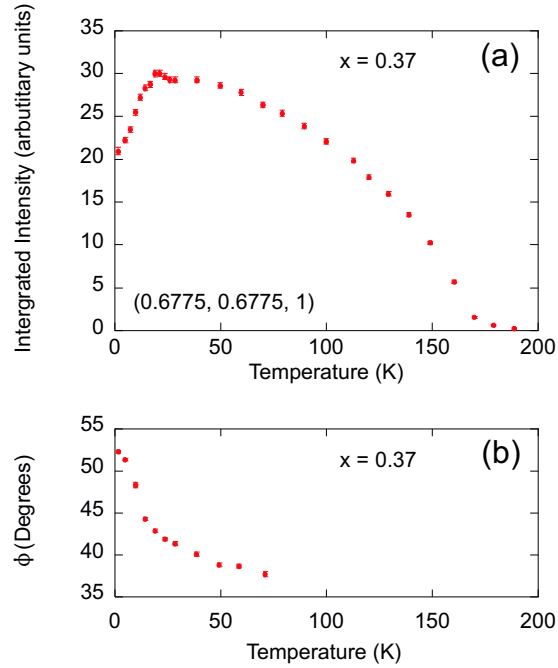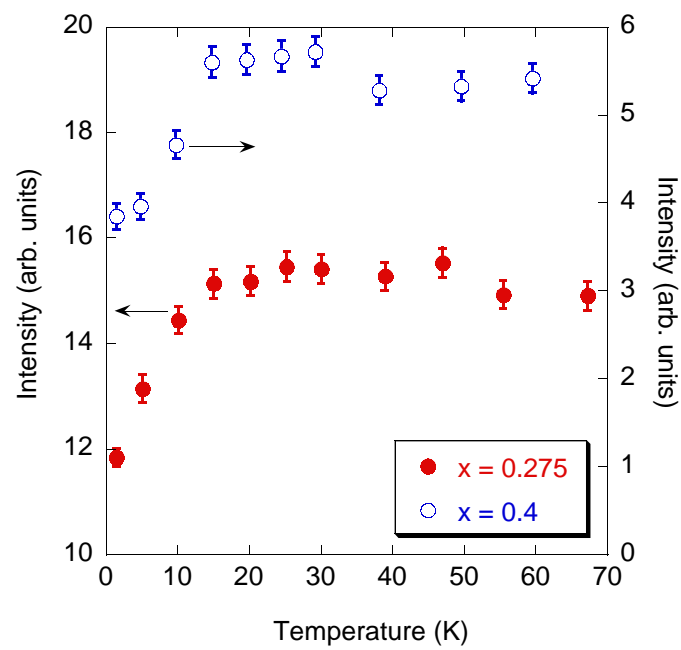Figure 6.9: The temperature dependence of the intensity of the magnetic Bragg peak at $\mathbf{Q}_2 = (0.645, 0.645, 0)$ for $x = 0.275$, and at $\mathbf{Q}_2 = (0.685, 0.685, 1)$ for $x = 0.4$.

6.3 Discussion

To aid the discussion of our results we refer to table 6.2, which summarizes the ordering values for each doping level. There are differences and similarities between the spin reorientations that occur for $x = 0.275$, 0.37 and 0.4 and those that occur for $x = 1/3$,[35] and $x = 1/2$. In each case the spins rotate in the same sense, away from the stripe direction on cooling. The size of the reorientation in $x = 0.37$ ($\Delta\phi \simeq 14.6°$), and more approximately in $x = 0.275$ and 0.4, is similar to that in $x = 1/3$ ($\Delta\phi \simeq 13°$), but smaller than in $x = 1/2$ ($\Delta\phi \simeq 26°$). However, in $x = 0.37, 0.275$ and 0.4 the spin reorientation occurs at a much lower temperature, $T_{\rm SR} \simeq 15\,{\rm K}$, compared with $T_{\rm SR} \simeq 50\,{\rm K}$ for $x = 1/3$ and $T_{\rm SR} \simeq 57\,{\rm K}$ for $x = 1/2$. Figure 6.10 summarizes the variation of $T_{\rm SR}$ with x that has so far been established for the doping range $0.275 \leq x \leq 0.5$. The results indicate that for general doping levels the spin reorientation occurs around $15\,{\rm K}$, but the particular compositions $x = 1/3$ and $x = 1/2$ are exceptional in having $T_{\rm SR} \simeq 50\,{\rm K}$.

There is also evidence of a trend in the direction of the ordered moment. The base temperature spin orientations are $53°$ for $x = 1/3$, $52°$ for $x = 0.37$, and $78°$ for $x = 1/2$, with charge ordering temperatures of $\sim 240\,{\rm K}$, $\sim 230\,{\rm K}$, $\sim 480\,{\rm K}$ respectively. We can add to this list an estimate of $41 \pm 8°$ for $x = 0.275$, (charge ordering temperature $\sim 160\,K$) based on the angle of $27 \pm 7°$ at 11 K found by Lee *et al.* [35], with an additional $10 - 15°$ due to the spin reorientation on cooling to $2\,{\rm K}$. Hence, there seems to be a correlation between the spin orientation angle ϕ and the charge-ordering temperature. Further measurements on samples with doping levels between $x = 0.4$ and 0.5 would be useful to confirm this trend.

x	T_{CO}	T_{SO}	ε	T_{SR}	$\phi(2\,\mathrm{K})$	$\Delta\phi$
	(K)	(K)		(K)	(deg.)	(deg.)
0.275	160±10	130±10	0.296±0.001	12.5±2.5	41 ± 8	10−15
1/3	240±5	200±5	0.333±0.001	50±5	53±2.5	13±4
0.37	230±10	170±5	0.354±0.001	19±1.5	52.3±0.2	14.6±0.4
0.4	180±20	150±10	0.371±0.001	15±2.5	−	10−15
1/2	480±30	80±10	0.443±0.001	57±2	78±3	26±5

Table 6.2: A summary of the characteristic ordering parameters of La$_{2-x}$Sr$_x$NiO$_4$. The charge-ordering temperature for the $x = 0.275$ was taken from reference [42], while the charge ordering temperatures for the $x = 0.4$ and 1/2 were taken from reference [38], and the data on $x = 1/3$ was taken from reference [35].
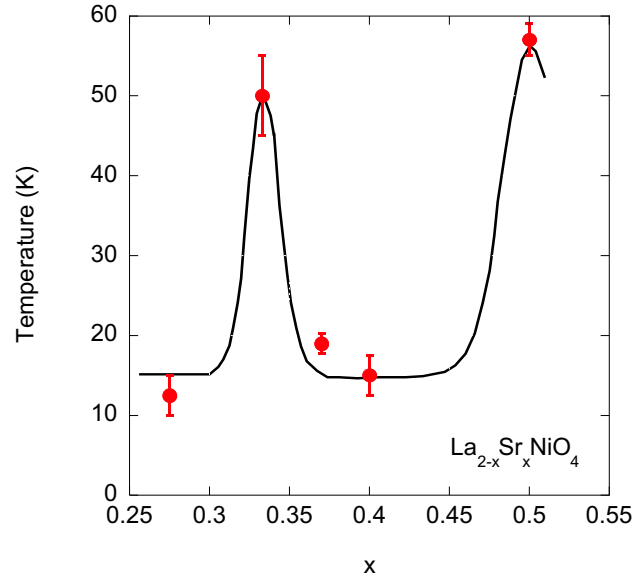
Figure 6.10: Variation with doping level, x, of the spin reorientation temperature, T_{SR}, defined as the temperature at which the $\mathbf{Q}_2$ Bragg peak starts to lose intensity on cooling. The line is a guide to the eye indicating the possible trend, the value for $x = 1/3$ is taken from reference [35].

The work by Lee *et al.* [35] showed that in the commensurately ordered $x = 1/3$ material the spins reorientate. Our neutron diffraction study of the $x = 1/2$ material establishes the existence of a spin reorientation in this material, and shows that a commensurate spin-stripe order is not required for a spin reorientation to occur in LSNO[89]. Results on $x = 0.275$, 0.37 and 0.4 further show that not even commensurate doping is required for a spin reorientation in LSNO[94]. It is likely that LSNO at all doping levels in the range $0.275 \leq x \leq 0.5$ undergo a spin reorientation, but that T_{SR} is larger at the commensurate doping compositions.

We are unaware of any model that explains the spin reorientation in La$_{2-x}$Sr$_x$NiO$_4$. Such a model needs to predict the three important properties we have identified in this work, i) the spin reorientation occurs for all doping levels in the range $0.275 \leq x \leq 0.5$, ii) T_{SR} is particular high in the $x = 1/3$ and $x = 1/2$ compounds and iii) the spin reorientation temperature can be reduced by application of a magnetic field.

Chapter 7

Spin Dynamics of Charge-stripe Ordered La$_{2-x}$Sr$_x$NiO$_4$

In this chapter I present unpolarized- and polarized-neutron inelastic scattering measurements taken on single crystals of La$_{2-x}$Sr$_x$NiO$_4$. The measured spin wave dispersion of the $x = 0.275$ and $1/3$ doped materials are very similar, indicating that the interaction strengths in the x = 0.275 are similar to those previously determined for the $x = 1/3$[49]. For energies above $30\,\text{meV}$ the excitations of the $x = 0.275$ are found to have a larger intrinsic width than the excitations in the $x = 1/3$[95].

Polarized neutron inelastic scattering measurements were performed on single crystals of $x = 0.275, 1/3$ and 0.37. In all these materials a suppression of the magnetic excitations was seen to occur between 10 and $25\,\text{meV}$, more prominently in the $x = 1/3$ doped material. Polarized neutron analysis revealed that this dip structure is not due to a spin anisotropy gap, suggesting instead that this feature is due to a coupling of the spin excitations to a collective motion of the stripe domain walls [49, 96].

At low energies we observed a diffuse component of the magnetic excitation spectrum in

the $x = 0.275$ and $1/3$[97]. This scattering forms a square pattern parallel and perpendicular to the stripe directions, and is found to be dispersive, with a maximum energy of ~ 10 meV. Polarization analysis at 2.5 meV in the $x = 1/3$ revealed that the dynamic susceptibility is a factor of 2 larger out of the ab plane than in the ab plane. We interpret this scattering as dynamic quasi-one-dimensional antiferromagnetic correlations among the spins of the stripe electrons.

7.1   Experimental detail

In this chapter I describe measurements on single crystals of La$_{2-x}$Sr$_x$NiO$_4$ grown by the floating-zone method[81] (see chapter 4), using the techniques of polarized-neutron diffraction ($x = 0.275, 1/3, 0.37$) and unpolarized-neutron diffraction ($x = 0.275, 1/3$). The $x = 0.275$ sample used for the MAPS experiment was an array of four crystals coaligned by x-ray diffraction, these crystals were grown at Kyoto University. A crystal similar to the $x = 0.275$ samples studied in the MAPS experiment was studied by neutron diffraction in reference [35], with that crystal being found to be stoichmetrically doped.

The spin wave excitations of the $x = 0.275$ and $1/3$ were mapped out by unpolarized-neutron scattering measurements performed on the time-of-flight chopper spectrometer MAPS at the ISIS Facility. The crystals were mounted in a closed-cycle refrigerator and aligned with the c axis parallel to the incident beam direction. A Fermi chopper was used to select the incident neutron energy. Incident energies of 60 and 160 meV were used. The intensity was normalized and converted to units of scattering cross-section (mb sr^{-1} meV^{-1} [f.u.]$^{-1}$) by comparison with measurements from a standard vanadium sample. Scattered neutrons were recorded in large banks of position-sensitive detectors. The spin dispersion was found to be highly two dimensional. Hence, we analyzed the data by making a series of constant energy slices and projecting the intensities onto the (h, k) two-dimensional reciprocal lattice plane. For an incident energy of 60 meV the resolution was typically 2.5 meV in energy and 0.05 Å^{-1} in wavevector, whereas for an incident energy of 160 meV the resolution was typically 6.9 meV in energy and 0.09 Å^{-1} in wavevector.

Further unpolarized- and polarized-neutron measurements were performed on the triple-

axis spectrometers (TAS) IN8, IN20 and IN22 at the Institut Laue-Langevin. The energies of the incident and scattered neutrons were selected by Bragg reflections from a double-focusing bent Si crystal monochromator and pyrolytic graphite (PG) crystal analyzer on IN8, PG crystals on IN22 and arrays of Heusler alloy crystals on IN20. On all three instruments the data were obtained with a final neutron wavevector of $2.66\,\text{Å}^{-1}$, and a PG (pyrolytic graphite) filter was placed between the sample and analyzer to suppress higher-order harmonic scattering. For polarized-neutron scattering on IN20 the spin polarization, $\mathbf{P}$, was maintained in a specified orientation with respect to the neutron wavevector, $\mathbf{Q}$, by an adjustable guide field of a few mT at the sample position. For the experiment on IN8 the crystal was orientated with the [100] and [010] crystal directions in the horizontal scattering plane, so that $(h,\,k,\,0)$ positions in reciprocal space could be accessed. On IN22 and IN20, we mounted the crystal with the [001] and [110] crystal directions in the horizontal scattering plane, so that $(h,\,h,\,l)$ positions in reciprocal space could be accessed. The resolution of IN22 was typically $0.6\,\text{meV}$ in energy, $0.04\,\text{Å}^{-1}$ in wavevector in the scattering plane and $0.13\,\text{Å}^{-1}$ in wavevector out of the scattering plane. For the constant $\mathbf{Q}$ scans performed on IN20 the typical resolution was $2.0\,\text{meV}$ in energy, $0.06\,\text{Å}^{-1}$ in wavevector in the scattering plane and $0.15\,\text{Å}^{-1}$ in wavevector out of the scattering plane. For constant energy scans on IN20 the typical resolution was $1.0\,\text{meV}$ in energy, $0.04\,\text{Å}^{-1}$ in wavevector in the scattering plane and $0.13\,\text{Å}^{-1}$ in wavevector out of the scattering plane.

The low energy excitation spectrum was additionally studied by unpolarized-neutron scattering measurements on the $x = 0.275$ and $1/3$ performed on the cold neutron triple axis spectrometer RITA-II at SINQ, at the Paul Scherrer Institut. The energies of the incident and scattered neutrons were selected by Bragg reflections from PG crystals. The data

were obtained with a final neutron wavevectors of $1.55\,\text{Å}^{-1}$, and a Be filter operating at $77\,\text{K}$ was present between the sample and the analyzer to suppress scattering of higher-order harmonics. The $x = 0.275$ crystal was mounted with the $[001]$ and $[110]$ directions in the scattering plane, so that $(h,\, h,\, l)$ positions in reciprocal space could be accessed. The energy resolution of these measurements was $0.3\,\text{meV}$ and the wavevector resolution was $0.02\,\mathring{A}^{-1}$.

7.2 Spin Wave Dispersion of the Ordered Moments in La$_{2-x}$Sr$_x$NiO$_4$

In figure 7.1 I again show the Ni sites of an *ab* plane of La$_{5/3}$Sr$_{1/3}$NiO$_4$. By measuring the spin wave dispersion via inelastic neutron scattering and comparing the measured dispersion to a theoretical model, it is possible to determine the intrastripe (J) and interstripe (J') exchange interactions of nearest neighbour Ni^{2+} spins. Previous work had measured the spin wave dispersion in the $x = 1/3$ along high symmetry directions and found the dispersion to be consistent with a linear spin wave model with $J = 15 \pm 1.5$ meV and $J' = 7.5 \pm 1.5$ meV[49]. By performing inelastic neutron scattering on the time flight direct geometry chopper spectrometer MAPS we were able to record the two dimensional spin wave dispersion, not just the spin wave dispersion along high symmetry directions. As previous studies have shown little or no spin wave dispersion variation with $\mathbf{Q_z}$ [49, 98], I will label the data with the two dimensional wavevector $\mathbf{Q} = (Q_x, Q_y)$. This notation ignores the variation of $\mathbf{Q_z}$ across the detectors, which needs to be accounted for when studying the intensity variation[1].

Figure 7.2(a) shows the spin wave dispersion along the (h,h) direction for the $x = 1/3$ at $T = 10$ K. In this data magnetic excitations can be seen to disperse out of the magnetic

---

[1]On a time-of-flight spectrometer with the incident neutron beam parallel to the c axis the out-of-plane wavevector component l varies with the excitation energy and the incident neutron energy. Although the magnetic excitation spectrum of La$_{2-x}$Sr$_x$NiO$_4$ is highly two-dimensional, the scattering intensity does vary with l. The variation is smooth, and depends partly on the magnetic form factor and partly on the direction of $\mathbf{Q}$, since neutrons scatter from spin fluctuations perpendicular to $\mathbf{Q}$. The ordered moment in La$_{2-x}$Sr$_x$NiO$_4$ lies in the ab plane, so the scattering becomes less sensitive to magnetic fluctuations parallel to the c axis as l increases.
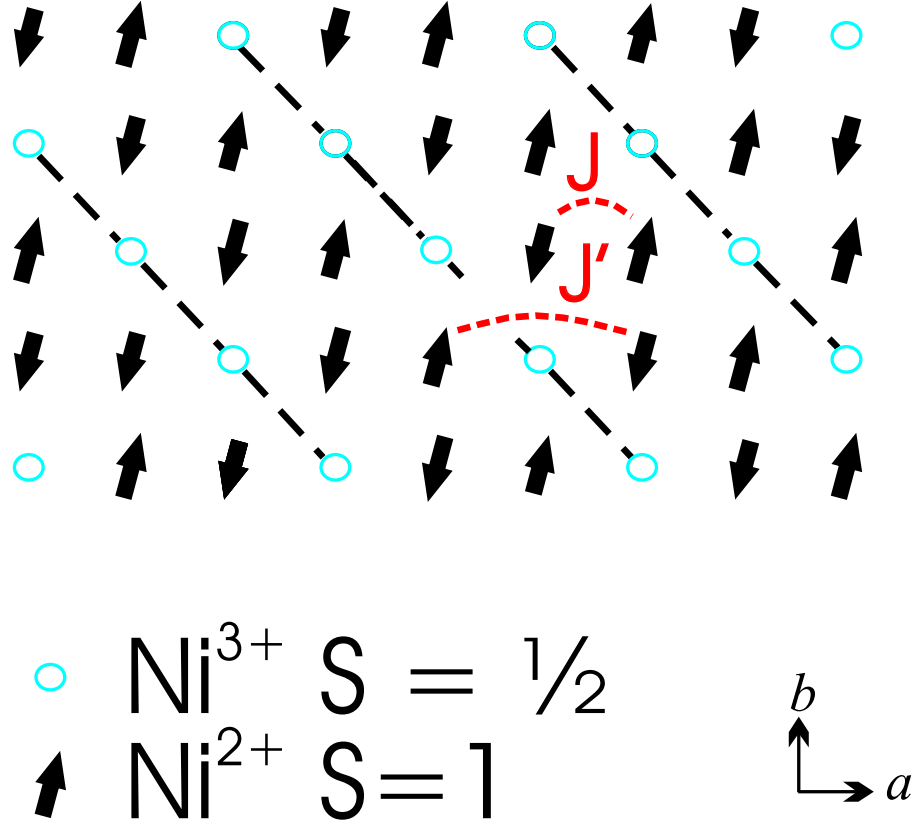
Figure 7.1: A model of the stripe order found in a ab plane of La$_{5/3}$Sr$_{1/3}$NiO$_4$. Circles represent holes residing on Ni^{3+} sites and the solid arrows represent the ordered Ni^{2+} spins. Where the nearest neighbour intrastripe (J) and interstripe (J') exchange interactions of the Ni spins are indicated.

zone centres (1/3, 1/3), (2/3, 2/3) and $(1,1)$ up to energies of $\sim 80 - 85$ meV. To aid the visualization of the data shown in Fig. 7.2(a) I have re-plotted the same data in Fig. 7.2(b) with a solid line guide to the eye over the spin wave excitations. Below 60 meV comparison of the spin wave dispersion parallel to the stripes along the $(-h, h)$ direction and perpendicular to the stripes along the (h, h) direction showed little anisotropy within the experimental accuracy. Above 60 meV the spin wave dispersion off the $[1, 1]$ and $[-1, 1]$ domains combine to hinder the study of the anisotropy of the spin wave dispersion, but the measurements appear to show a small spin wave anisotropy consistent with the work on $x = 0.31$[74]. The spin wave dispersion recorded in Fig. 7.2(a) was observed to be

highly consistent with the previous work on $x = 1/3$[49].
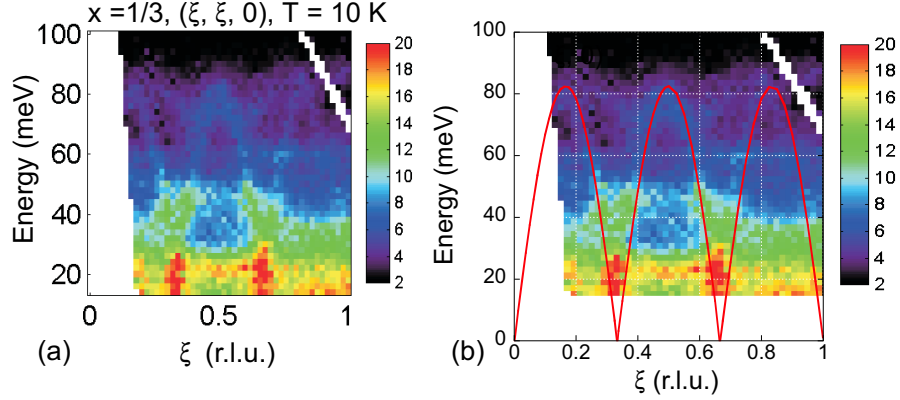
Figure 7.2: (a) Inelastic neutron scattering measurements taken on MAPS showing a data slice of Energy versus **Q** along the (h, h) direction in reciprocal space for the $x = 1/3$ at 10 K. (b) The same slice overplotted with a guide to the eye to highlight the spin wave dispersion. For the scattering around $75 - 85$ meV additional excitations between the dispersion modes can be observed, this extra scattering is due to the excitations from the twin domain.
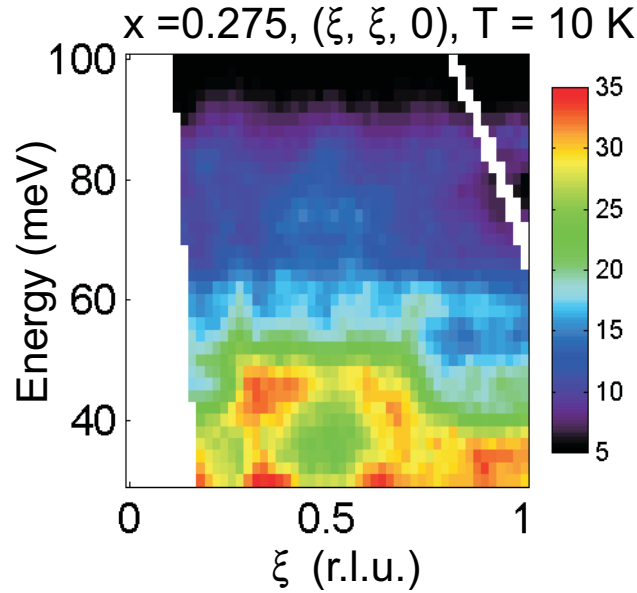
Figure 7.3: A data slice showing Energy versus **Q** along the (h, h) direction in reciprocal space for the $x = 0.275$ at 10 K, taken on MAPS.

The spin wave dispersion of the array of $x = 0.275$ crystals was studied under the same conditions as the $x = 1/3$ material. In Fig. 7.3 I plot a data slice of the spin wave

dispersion in $x = 0.275$, equivalent to the data slice of Fig. 7.2(a) for the $x = 1/3$. In this data magnetic excitations can be seen to disperse out of the magnetic zone centres (0.35, 0.35), (0.65, 0.65) and (1, 1) up to energies of $\sim 80 - 85$ meV, the same energy as that of the $x = 1/3$. Although the spin wave excitations disperse up to the same energy the excitations appear to be more diffuse in the $x = 0.275$ than in the $x = 1/3$. As the excitations in the $x = 0.275$ appear to be broad in $\mathbf{Q}$, I plot in figure 7.4 constant energy slices of the equivalent $x = 0.275$ and $x = 1/3$ data, where the data has been integrated over an energy range of 5 meV. In Fig. 7.4(a) data taken at $35-40$ meV for $x = 0.275$ shows four dispersion rings emerging out of the magnetic zone centres symmetrically spaced around (0.5, 0.5). Figure 7.4(b) shows the equivalent slice for $x = 1/3$ again showing dispersion coming out of the four magnetic zone centres and the scattering appears to be sharper than in the $x = 0.275$ data of Fig. 7.4(a). By $50-55$ meV the spin wave excitations have dispersed to produce the larger dispersion rings of Fig. 7.4(c) for $x = 0.275$ and the narrower dispersion rings of Fig. 7.4(d) for $x = 1/3$. At higher energies the spin wave dispersion from the two domains one with stripes running parallel to $[1, 1]$ and the other with stripes running parallel to $[-1, 1]$, begin to merge. Figure 7.4(e) shows this occurring at $75 - 80$ meV in the $x = 0.275$. The dispersion rings of the two domains have merged creating intense scattering at (0.5, 0.5) and diffuse scattering around (0.5, 0.5) forming a " + " shape of excitations. In Figure 7.4(f) I show the excitations in the $x = 1/3$ for $75 - 80$ meV. For this energy in the $x = 1/3$ the excitations appear sharper and show more detail of the dispersion surface than the excitations of the $x = 0.275$, the excitations resemble an excitation peak at (0.5, 0.5) with four satellite peaks in a cross orientation. In the $x = 0.275$ the excitations at $75 - 80$ meV are too broad to observe this detail of the dispersion surface.
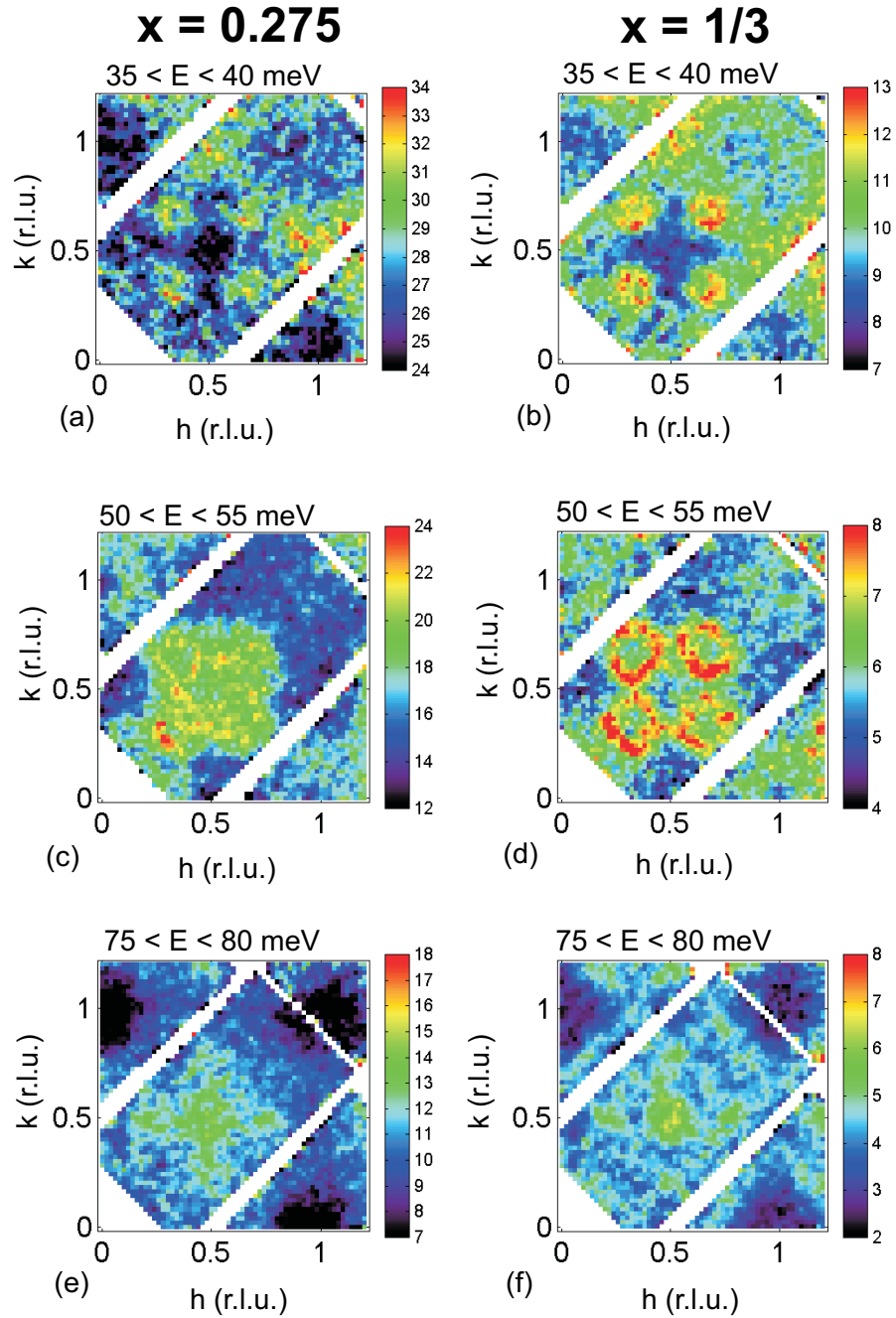
Figure 7.4: Neutron scattering measurements from $x = 0.275$ and $x = 1/3$ measured on MAPS at $T = 10$ K. $(a) - (f)$ are constant-energy slices showing the variation of the intensity in the (h, k) plane at different energies, the slices (a),(c),(e) are of the $x = 0.275$ and the slices (b),(d),(f) are of the $x = 1/3$. The energies of the slices are (a)&(b) $35 \leq E \leq 40$ meV, (c)&(d) $50 \leq E \leq 55$ meV and (e)&(f) $75 \leq E \leq 80$ meV. Data from four equivalent Brillouin zones have been averaged.

To confirm the observation that the magnetic excitations in the $x = 0.275$ are broader than in the $x = 1/3$ cuts were made through the data slices along the $(1,1)$ direction in reciprocal space for both materials. Figure 7.5 shows the spin wave excitations for $35 \leq E \leq 40\,\text{meV}$ in (a) $x = 0.275$ and (b) $x = 1/3$. The cuts in Fig. 7.5 show broadening of the spin wave excitations in the $x = 0.275$ that is typically observed in the measured spin wave dispersion on MAPS for $E > 10\,\text{meV}$.
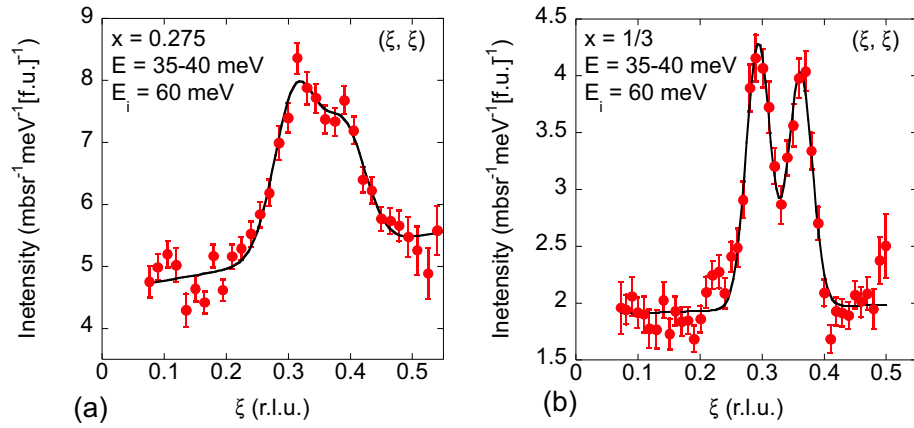
Figure 7.5: Cuts of the MAPS data at $T = 10\,\text{K}$ taken along the the $(1,1)$ direction in reciprocal space for $35 \leq E \leq 40\,\text{meV}$ on (a) $x = 0.275$ and (b) $x = 1/3$. The solid curves in (a) and (b) are the result of fitting the data with two gaussians on a sloping background.

Figure 7.6 shows the dispersion of the spin excitations for both $x = 0.275$ and $1/3$ parallel to the $(\xi,\ \xi)$ direction in reciprocal space. The data points were obtained from Gaussian fits to the peaks observed in cuts such as those displayed in Fig. 7.5. The points in Fig. 7.6 are the fitted peak centres corrected for the effect of the non-zero width of the cut perpendicular to the cut direction. The measured spin wave dispersion of Fig. 7.6 for the $x = 1/3$ is consistent with the spin wave dispersion of the $x = 1/3$ previously measured on a triple axis spectrometer[49]. Where the exchange energies were calculated from linear spin wave theory to be $J = 15 \pm 1.5\,\text{meV}$ and $J' = 7.5 \pm 1.5\,\text{meV}$. Apart

from incommensurate centring of the spin wave dispersion, the spin wave dispersion of the $x = 0.275$ shows little variation form that of the $x = 1/3$, therefore the exchange interactions of the $x = 0.275$ will be close to the values obtained for the $x = 1/3$. The only significant difference between the excitations of the $x = 0.275$ and $x = 1/3$ is the excitations in the $x = 0.275$ are borader than in the $x = 1/3$.

Figure 7.6: Dispersion of the magnetic excitations in $x = 0.275$ and $x = 1/3$ parallel to the (ξ, ξ) direction. The points are the results of fits to cuts such as those shown in Fig. 7.5.

Below 30 meV there is strong scattering from phonons in these materials. In this energy range to separate the magnetic and non-magnetic scattering it is necessary to use polarized neutron scattering. We performed polarized neutron scattering on single crystals of $x = 0.275$, 0.33 and 0.37 on the triple axis spectrometer IN20 at the ILL. We mounted each crystal with the [001] and [110] directions in the horizontal scattering plane, so that (h, h, l) positions in reciprocal space could be accessed. Initial measurements were carried out with the neutron polarization $\mathbf{P}$ aligned parallel to the scattering vector $\mathbf{Q}$ so that the spin-flip (SF) channel would contain purely magnetic scattering.
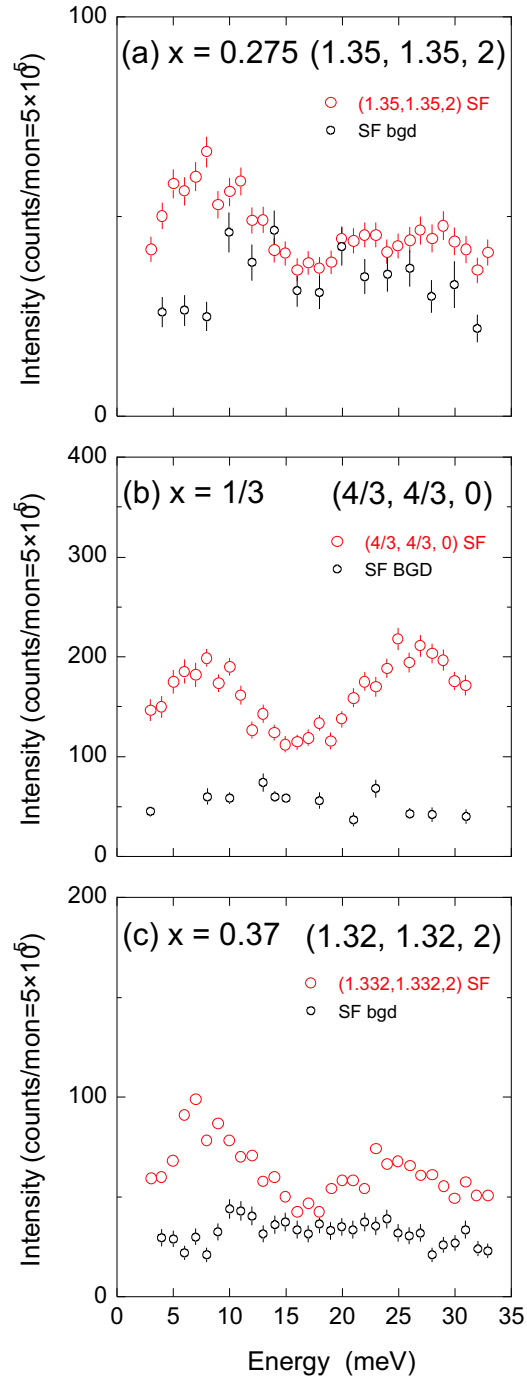
Figure 7.7: Polarized neutron scattering measurements on (a) $x = 0.275$, (b) 1/3, and (c) 0.37. The plots show energy scans performed at the magnetic ordering wavevector appropriate to each material. These spin flip measurements were performed with $\mathbf{P} \parallel \mathbf{Q}$ and the SF background is estimated from scans centred away from the magnetic excitation peak. The data was taken at $T = 2\,\mathrm{K}$ on the $x = 0.275$, 0.37 and at $T = 13\,\mathrm{K}$ on the $x = 1/3$.

Figure 7.7 shows energy scans of the magnetic ordering wavevector appropriate to each material studied ($\mathbf{Q_m}$). Below 7 meV in all three compositions we observed a reduction of the scattering intensity, but this reduction was not present in scans made with the equivalent $\mathbf{Q_m}$ wavevectors with a large component along the c axis. As neutrons scatter from spin fluctuations perpendicular to $\mathbf{Q}$ these measurements suggest the origin of the reduction of intensity below 7 meV is due to the freezing out of the c component of the spin fluctuations. We therefore deduce that the origin of the reduction is an out-of-plane single ion anisotropy gap. The more interesting feature is the dip in intensity of the spin wave excitations centred around $15 - 20$ meV. This is most clearly defined in the results of the $x = 1/3$ in Fig. 7.7(b), for increasing energy the intensity increases to a maximum at 7 meV before decreasing to a minimum between $15 - 20$ meV, then the intensity increases up to a second maximum at ~ 25 meV and finally the intensity begins to decrease for higher energies. In Fig. 7.7(a) on the $x = 0.275$ the data only weakly shows this structure, possibly due to the broadening of the spin wave excitations observed in this material (see figure 7.5). Further analysis of the MAPS data on the $x = 0.275$ indicated that the integrated intensity of the spin wave excitations behave in the same manner for both the $x = 0.275$ and 1/3 [99].

Polarization analysis can be used to identify spin anistropy gaps in a way that is similar to the determination of the orientation of the ordered spin direction, see chapter 6.2. We performed the polarization analysis on the $x = 1/3$ at $\mathbf{Q_m} = (1.33,\ 1.33,\ l)$ for $E = 3$ meV at $l = 1$ and for $E = 10, 15, 26$ meV at $l = 0$. By varying the orientation of the spin polarization $\mathbf{P}$ with respect to the scattering wavevector $\mathbf{Q_m}$ we can determine the ratio of the dynamic spin fluctuations out of the ab plane, $S_c(\omega)$, to the dynamic spin fluctuations parallel to the stripe direction, $S_\parallel(\omega)$. The three measuring configurations
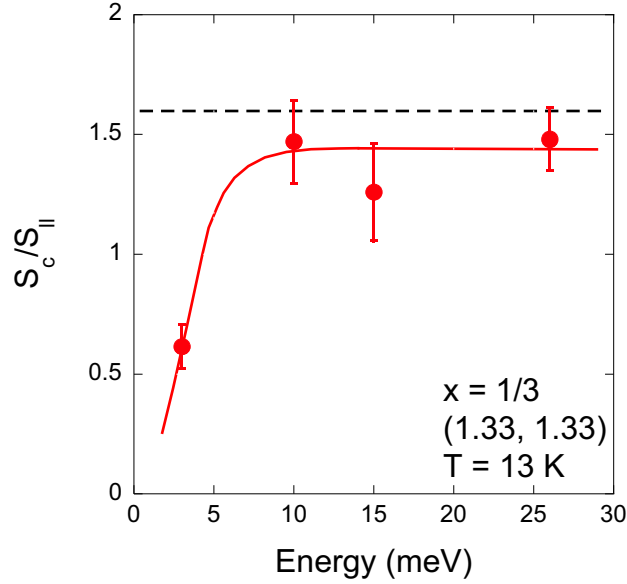
Figure 7.8: The variation with energy of the ratio of the magnetic response along the crystal c axis (S_c) and parallel to the stripe direction ($S_\parallel$), for the $x = 1/3$. These polarization analysis measurements were performed at the 2-D magnetic zone centre $\mathbf{Q_m} = (1.33, 1.33)$. For isotropic spin wave oscillations about an ordered moment 53° away from the stripe direction[35], the calculated ratio of $S_c/S_\parallel$ is that indicated by the broken line. At low energies the ratio of $S_c/S_\parallel$ is reduced due to the freezing of the out-of-plane spin fluctuations below the 7 meV gap, which is shown in figure 7.7. The solid line is a guide to the eye.

that are used for these measurements are (1) $\mathbf{P} \parallel \mathbf{Q}$, (2) $\mathbf{P} \perp \mathbf{Q}$ in the scattering plane, and (3) $\mathbf{P} \perp \mathbf{Q}$ with $\mathbf{P}$ vertically out of the scattering plane, with the measured scattering intensities respectively being I_1, I_2, I_3. The scattering intensities for these configurations are shown in table 7.1. For $l = 0$ we obtain;

$$\frac{I_1 - I_2}{I_1 - I_3} = \frac{S_c}{S_\parallel} \tag{7.1}$$

The spin wave excitations at 3 meV show a slight modulation of intensity with l due to weak interlayer correlations that produce stronger excitations at $l = $ odd[49]. So measurements at 3 meV were carried out at $l = 1$, the small angular difference of 9° of $l = 1$ and 0 means that equation 7.1 is still a good approximation to the correct result.

	P configuration	Components of spin fluctuations
I$_1$	**P** $\parallel$ **Q**	$S_c(\omega) + S_\parallel(\omega) + $ Bgd
I$_2$	**P** $\perp$ **Q**(**P** in horiz plane)	$S_\parallel(\omega) + $ Bgd
I$_3$	**P** $\perp$ **Q**(**P** vertical)	$S_c(\omega) + $ Bgd

Table 7.1: Expressions for the intensity of SF inelastic scattering for different orientations of the neutron polarization **P** relative to the scattering vector **Q**. Where $S_c(\omega)$ are the spin fluctuations parallel crystal c axis, $S_\parallel(\omega)$ are the spin fluctuations parallel to the stripe direction and Bgd is the background scattering.

Figure 7.8 shows the results of the polarization analysis on the spin fluctuations in the $x = 1/3$ crystal. The ratio of $S_c/S_\parallel$ is observed to be near constant for $E = 10, 15$, and $26\,\text{meV}$ but much smaller for $E = 3\,\text{meV}$. At the base temperature the spins of the ordered moments are orientated at 53° to the stripe direction[35]. For isotropic spin fluctuations around the ordered moment the spin fluctuations are in the plane that the ordered spin is normal to. If the spin fluctuations are isotropic around the ordered moment we therefore would expect to measure $S_c/S_\parallel = 1/\sin^2(53) = 1.57$, as the spins are orientated 53° away from stripe direction. This is approximately the value obtained for the polarization analysis at $E = 10, 15$ and $26\,\text{meV}$. The ratio of $S_c/S_\parallel$ for $E = 3\,\text{meV}$ is observed to be significantly lower than this value, confirming that at low energies the out-of-plane spin fluctuations are frozen out and the spins only fluctuate in the ab plane.

7.2.1 Discussion

Despite the differences in the ordering parameters of the $x = 0.275$ and $1/3$ [35], we observed the spin wave dispersion in Fig. 7.6 of these two materials to be remarkably similar. This implies that the interaction strengths in the $x = 0.275$ are approximately

equal to those obtained on the $x = 1/3$, an intrastripe interaction of strength $J = 15 \pm$ 1.5 meV and interstripe interaction of strength $J' = 7.5 \pm 1.5$ meV[49]. The one significant difference, despite the long range static order exhibited by both materials, is the large intrinsic widths of the excitations in $x = 0.275$ compared to the $x = 1/3$ (shown in Fig. 7.5). The main difference between the ordering of the two materials is that the order in the $x = 0.275$ is incommensurate with the crystal structure, suggesting that the variation of the charge-order periodicity in the $x = 0.275$ acts to dampen the spin wave excitations.

In linear spin wave theory the spin wave dispersion of commensurately charge-stripe ordered materials has been calculated[75, 76]. For site centred charge-stripes (stripes residing on the Ni site) with charge-stripes spaced three Ni sites apart there is one excitation mode, but when the charge stripes are four Ni sites apart each antiferromagnetic domain has a net ferromagnetic moment and there is an additional optic dispersion mode. The $x = 0.275$ material studied here has an incommensurate charge-stripe structure with a periodicity in real space that lies between charge-stripes separated by three or four Ni sites. One proposed model of the charge-stripe ordering in an incommensurately ordered material is that the ordering varies between commensurately spaced charge stripes spaced either 2,3 or 4 Ni sites apart, and the average period of different commensurate spacings leads to an incommensurate charge-stripe ordering period. In this model the $x = 0.275$ has charge stripes that vary between 3 or 4 Ni sites apart, therefore in the spin excitations of the $x = 0.275$ we may expect to observe the optic mode of a commensurate charge-stripe ordering with charge-stripes four Ni sites apart. We measured the spin wave excitations up to 145 meV in the $x = 0.275$ but did not observe an acoustic mode. This implies one of two things, 1) the optic mode is at higher energies or 2) there is no optic mode. The gap between the expected optic mode and the main spin wave dispersion is

governed by the value of J'/J, this was calculated to be $1/2$ in the $x = 1/3$[49]. For LSNO

with charge-stripes spaced four Ni sites apart and $J'/J = 1/2$ the optic mode should be

observable in the spin excitation spectrum below $145\,\mathrm{meV}$. There could be an optic spin

mode at higher energies but such a mode would be at far higher energies than predicted

by linear spin wave theory. If there is not an optic mode in $x = 0.275$ that would suggest

that the simple description of the incommensurate period of charge-ordering in $x = 0.275$

is a result of the charge-stripe period varying between different commensurate spacings

is an inadequate description of incommensurate charge-ordering. These results are not

evidence of charge-stripes residing on the O sites (bond centred) in $x = 0.275$, as lin-

ear spin wave theory predicts bond centred charge-ordering to have additional excitation

modes[76].

At $E < 30\,\mathrm{meV}$ we had to study the excitations using polarized neutron scattering due

to the strong phonon interactions in this energy range. In the polarized neutron scans of

Fig. 7.7 we observed that below $7\,\mathrm{meV}$ a reduction of the intensity occurs in the spin wave

fluctuations for $x = 0.275, 1/3$ and 0.37 materials. The l dependence of this reduction

and the polarization analysis on $x = 1/3$ at $3\,\mathrm{meV}$ (see Fig. 7.8) confirm this reduction

to be due to an out-of-plane single ion anisotropy gap. In undoped La$_2$NiO$_4$ the out-

of-plane anisotropy gap is $16\,\mathrm{meV}$[98]. From these measurements the out-of-plane single

ion anistropy energy (K_c) has been determined to be $K_c = 0.52\,\mathrm{meV}$ in La$_2$NiO$_4$[98] and

$K_c = 0.07\,\mathrm{meV}$ in the $x = 1/3$[49], hence we expect $K_c \approx 0.07\,\mathrm{meV}$ in the $x = 0.275, 0.37$.

The cause of this reduction of K_c in the doped compounds is unknown.

The second feature revealed by polarized neutron scattering was a dip in the scattering

intensity of the spin wave fluctuations centred on $\sim 15 - 20\,\mathrm{meV}$. From the polarization

analysis on $x = 1/3$ (Fig. 7.8), we determined that the spin fluctuations at $E = 10, 15$, and

26 meV are consistent with isotropic fluctuations about the ordered moment, and hence the dip structure cannot be an anisotropy gap. As the dip feature is most prominent in the $x = 1/3$ material a purely magnetic origin for this feature that involves the ordered Ni^{2+} spins is unlikely, as the $x = 1/3$ is a two-sublattice antiferromagnet whose spin wave spectrum should only contain spin anisotropy gaps. This feature is absent in La$_2$NiO$_4$[98], therefore the dip structure is unlikely to be due to a coupling to a phonon excitation of the host lattice. Having ruled out these possibilities one remaining origin for the dip feature is a coupling of the spin excitations to an excitation associated with the stripes. Possible excitations of the stripes could be i) a collective sliding motion of the charge-stripe domain walls, that is enhanced for charge-stripes spaced three lattice spacings apart, i.e. in the $x = 1/3$, ii) a phonon associated with the local distortion of the structure around the charge stripes, or iii) a coupling between the spin degrees of freedom of the charge stripes and the spin excitations form the antiferromagnetic regions between the charge stripes.

The results of this work have identified features of the spin wave excitations of charge-ordered La$_{2-x}$Sr$_x$NiO$_4$ with $x \sim 1/3$: (i) a robustness of the magnetic interaction strengths to doping variation, (ii) a reduction of the out-of-plane single ion anistropy energy and (iii) a suppression of the spin fluctuations around $15 - 20$ meV. These findings which are not consistent with spin wave theory emphasize the importance of understanding the spin and charge degrees of freedom in charge-ordered La$_{2-x}$Sr$_x$NiO$_4$.

7.3 Spin Correlations among the charge carriers of La$_{2-x}$Sr$_x$NiO$_4$
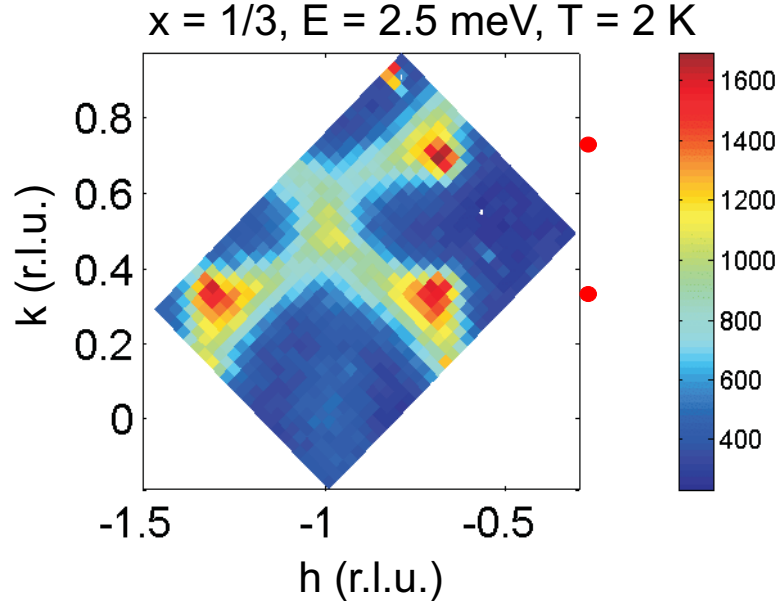
Figure 7.9: Inelastic neutron scattering from IN8 of $x = 1/3$ at 2.5 meV, displayed on a contour plot of the intensity in the $(h,\ k,\ 0)$ plane of reciprocal space at 2.5 meV. The plot is constructed from 25×35 data points from 25 parallel scans of the $(h,\ k,\ 0)$ plane. Circles have been added to indicate the location in reciprocal space of the four magnetic zone centres about the position $(-1/2,\ 1/2, 0)$.

To compliment the studies of the higher energy spin wave spectrum we carried out inelastic neutron scattering measurements on the low energy excitation spectrum. In figure 7.9 I show a contour plot of the low energy excitation spectrum from the $(h,\ k,\ 0)$ plane of reciprocal space of $x = 1/3$ material. This plot was created from a series of parallel scans performed at $E = 2.5$ meV at $T = 2$ K on IN8. This figure clearly shows sharp excitations centred on the magnetic zone centres $(-2/3,\ 1/3,\ 0)$, $(-2/3,\ 2/3,\ 0)$ and $(-4/3,\ 1/3,\ 0)$ that are consistent with the ordered structure and high energy spin wave excitation spectrum of this material. A second feature that this data shows is a series

of diffuse diagonal 'ridges' of scattering. In figure 7.10(a) I show a simplified diagram of the scattering we observed in the data of Fig. 7.9, displaying the two modes of scattering observed: excitations coming out of the magnetic zone centres and the 'ridges' of scattering.
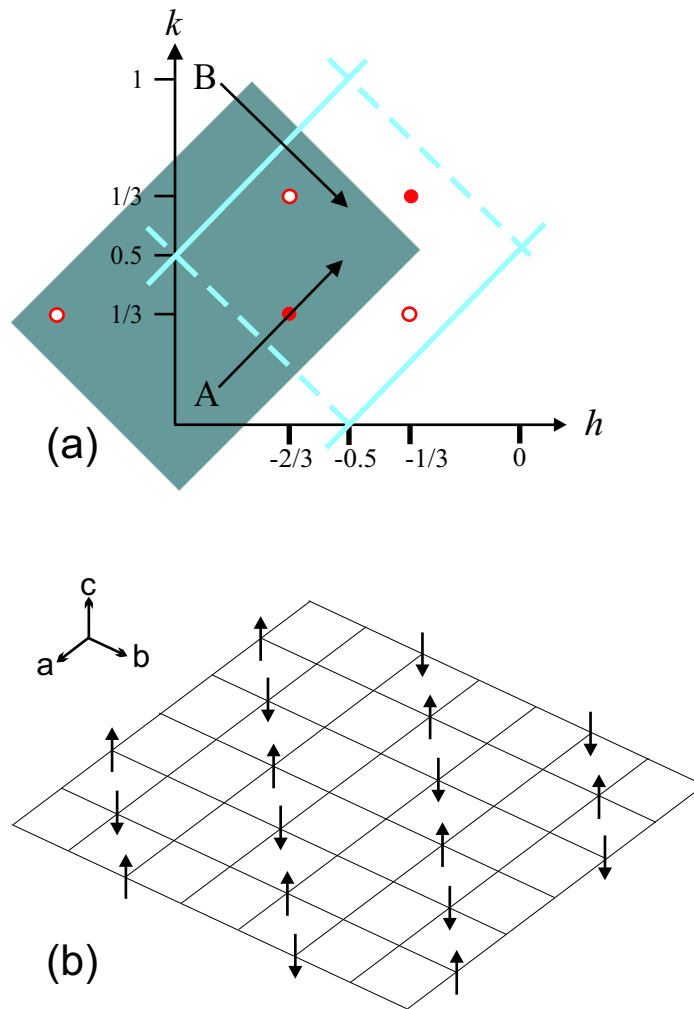
Figure 7.10: (a) A diagram of the low energy excitations for $x = 1/3$. The diagonal lines indicate where ridges of scattering would be observed if the spins of the charge stripes acted as 1-D antiferromagnets. Circles represent the zone centres of the magnetic stripe domains. Open circles and dashed diagonal lines represent scattering from the $[1, 1, 0]$ domain; filled circles and solid lines represent scattering from the $[-1, 1, 0]$ domain. The shaded area represents the area of reciprocal space scanned in Fig.7.9. (b) A diagram of a $[1, 1, 0]$ stripe domain with local 1D AF correlations on the charge stripes.

Figure 7.11 shows a scan performed along a line equivalent to path A of Fig. 7.10(a), on the $x = 1/3$ for the elastic scattering and $2\,\mathrm{meV}$ at $T = 14\,\mathrm{K}$ performed on IN22. In the excitation spectrum at $2\,\mathrm{meV}$ we observed two distinct scattering modes, one mode centred on $(1/3,\ 1/3)$ that is as expected from the stripe superlattice structure and a second mode centred on approximately $(0.27, 0.27)$. The elastic scattering performed along the same path only contains a magnetic Bragg peak for the ordered stripe superlattice structure. This shows that the 'ridge' scattering has no static component. Measurements of the l dependence of the ridge scattering showed a monotonic decrease in intensity with increasing l but no modulation.
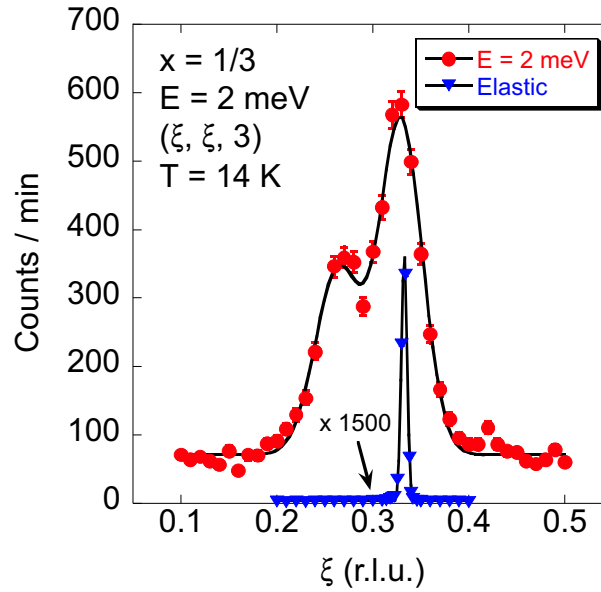
Figure 7.11: Scans of $x = 1/3$ along path A of figure 7.10(a) for $2\,\mathrm{meV}$ and the elastic scattering.

To fully determine the origin of the ridge scattering to be magnetic we performed polarized neutron scattering using the triple-axis spectrometer IN20. We began by performing polarized-neutron diffraction measurements with the neutron polarization $\mathbf{P}$ parallel to the scattering vector $\mathbf{Q}$. In this configuration a neutron's spin is flipped during a magnetic

scattering process, but remains unchanged when scattered by a non-magnetic process, e.g. from a distortion of the lattice. Thus, by measuring the spin- flip (SF) and non-spin-flip (NSF) channels one can identify whether the origin of the scattering is magnetic or not. Figure 7.12 shows SF and NSF polarized neutron scans of the $x = 1/3$ for $E = 2\,\text{meV}$ at $T = 2\,\text{K}$ along path B of Fig. 7.10(a). The ridge scattering observed in scans along both path B and path A (not shown) only occurs in the SF channel, indicating a magnetic origin of these fluctuations. This scan also shows how the ridge scattering does not follow a straight path, figures 7.9 and 7.11 both show how the scattering flexes away from a centring of (0.25, 0.25) along lines equivalent to path A of Fig. 7.10(a).
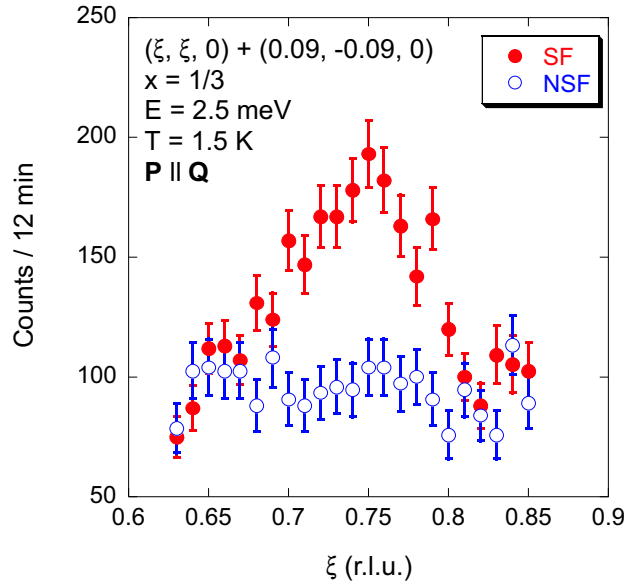
Figure 7.12: Spin-flip (SF) and non-spin-flip (NSF) scattering at $E = 2.5\,\text{meV}$ for $x = 1/3$ at $T = 2\,\text{K}$. The scan follows path B as indicated in figure 7.10(b). The scattering was measured with $\mathbf{P} \parallel \mathbf{Q}$.

Having determined the origin of the ridge scattering to be magnetic we performed neutron polarization analysis on the scattering in the same manner as performed on the spin wave excitations in section 7.2. We scanned the SF scattering of two wave vectors of the

ridge scattering $\mathbf{Q_1} = (0.25, 0.25, 3.5)$ and $\mathbf{Q_2} = (0.75, 0.75, 0)$ in three configurations (1) $\mathbf{P} \parallel \mathbf{Q}$, (2) $\mathbf{P} \perp \mathbf{Q}$ in the scattering plane, and (3) $\mathbf{P} \perp \mathbf{Q}$ with $\mathbf{P}$ vertically out of the scattering plane. As neutrons scatter from spin fluctuations perpendicular to the scattering wavevector, $\mathbf{Q_1}$ probes mainly the in-plane fluctuations and $\mathbf{Q_2}$ probes the in-plane and out-of-plane fluctuations equally. From the measurements at $\mathbf{Q_1}$ we determined the spin fluctuations to be isotropic in the ab plane within the experimental error of 20%. Measurements of $\mathbf{Q_2}$ however revealed the component of the spin fluctuations out-of-plane are a factor of 2.3 ± 0.4 stronger than in-plane. Therefore we conclude that the spin fluctuations of the ridge are a factor of two stronger along the c axis than in the ab plane.

Figure 7.13: (a) Constant energy scans along path B of figure 7.10(b) on the $x = 1/3$, where the successive scans have been offset by the addition of 2000 counts. (b) The dispersion of the ridge scattering, produced from fits of constant energy scans such as those shown in (a). The blue line is the main excitation mode of a spin-1/2 Heisenberg AF chain with $J = 3.2$ meV, and the vertical black lines indicate the zone boundaries of this fit.

We performed scans along lines equivalent to path B of Fig. 7.10(a) for different energies. Figure 7.13 shows several of these scans at different energies. At 2.5 meV the ridge scattering is one unresolved peak, and with increasing energy this peak is observed to broaden. By 6 meV the ridge scattering can clearly be resolved as two modes dispersing in opposite

directions parallel to the scan direction. In figure 7.13(b) I plot the fitted peak centres of scans such as those shown in Fig. 7.10(a). The ridge scattering shows dispersion up to $\sim 10\,\text{meV}$ with zone boundaries occurring at approximately $\xi = 1/4 \pm 1/8$.

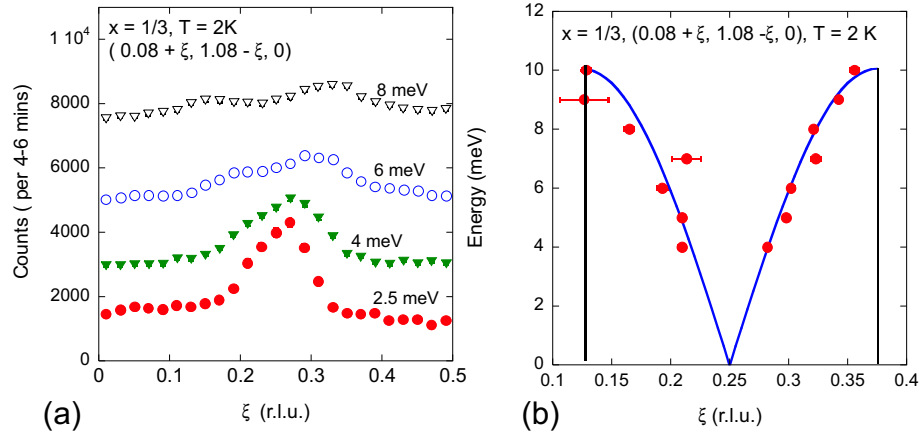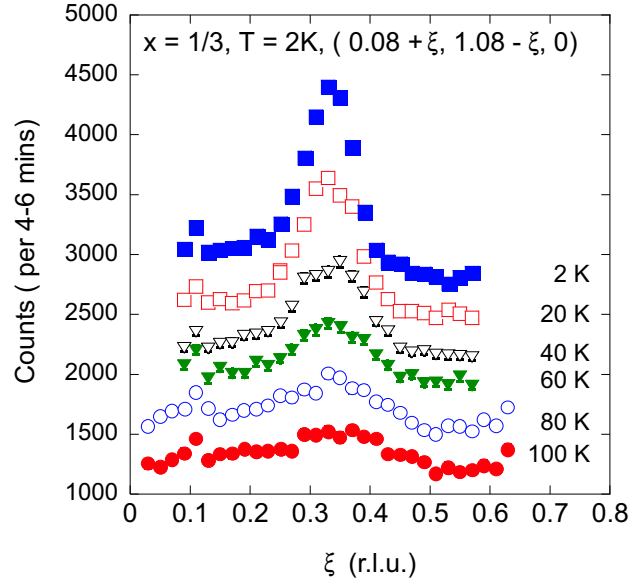Figure 7.14: (a) The temperature variation the excitations at $2\,\text{meV}$ along path B of figure 7.10(b) on the $x = 1/3$, where the successive scans have been offset by the addition of 400 counts.

Figure 7.14 shows the temperature dependence of the ridge scattering along the same path (B) at $2\,\text{meV}$ on the $x = 1/3$. We observed the peak from the ridge scattering to decrease in intensity and widen with increasing temperature. By $100\,\text{K}$ the peak almost completely loses its intensity.

I now compare the low energy excitations of the $x = 1/3$ to the low energy excitations of the $x = 0.275$ taken on MAPS. Figure 7.15(a) shows a data slice of the $(h,\ k)$ plane of reciprocal space for the $x = 0.275$ for $3 \leq E \leq 5\,\text{meV}$ at $T = 10\,\text{K}$. The data shows the four strong scattering centres evenly spaced around $(0.5,\ 0.5)$ associated with spin excitations from the ordered Ni^{2+} sites and 'ridges' of diffuse scattering similar to those observed from the $x = 1/3$ in Fig. 7.9. Figures 7.15(b) and 7.15(c) show cuts of this data
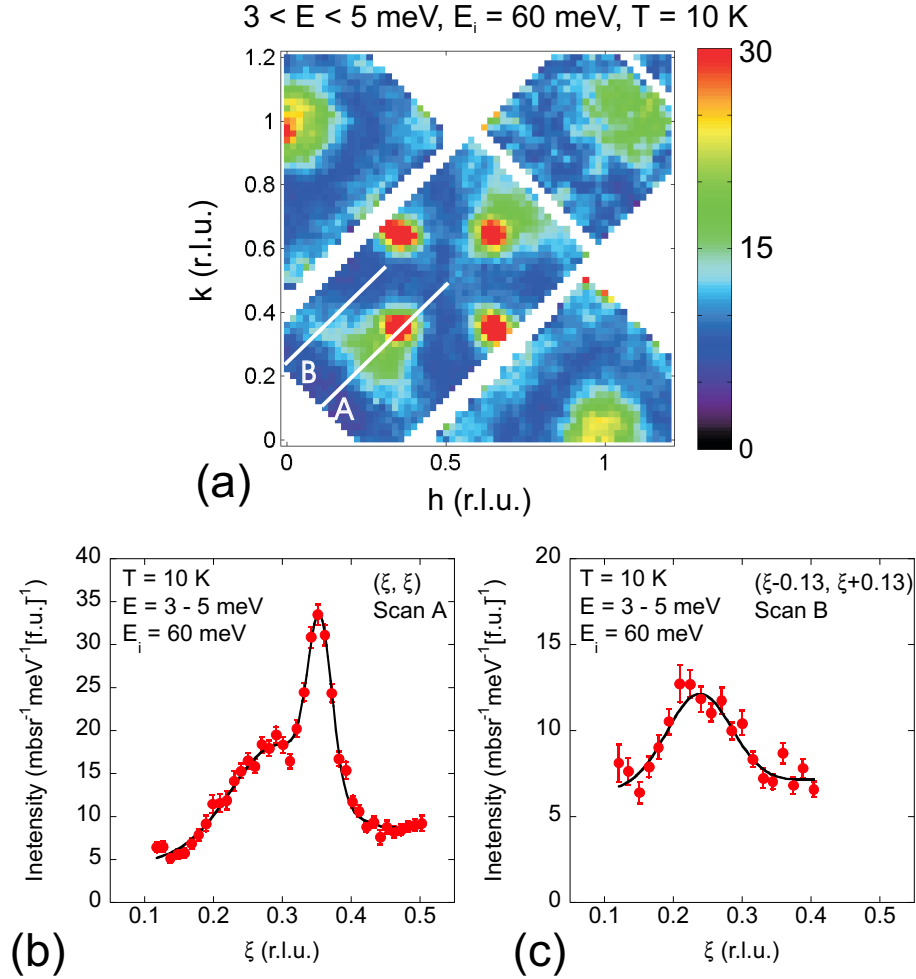
Figure 7.15: (a) A data slice taken from measurements of the $x = 0.275$ for $3 \leq E \leq 5$ meV at $T = 10$ K on MAPS. (b) and (c) are cuts obtained from the data slice in (a) along paths A and B respectively. The lines in (b) and (c) are fits to the data of respectively 2 and 1 gaussian peak shapes on a sloping background.

along paths A and B of Fig. 7.15(a) respectively. These paths are equivalent to paths A and B shown in Fig. 7.10(a). The cut in Fig. 7.15(b) shows two scattering modes along the path (ξ, ξ), with the ridge scattering centred on $\xi \approx 0.27$. The cut shown in Fig. 7.15(c) shows how the scattering along path B in the $x = 0.275$ is centred on $\xi \approx 0.25$. The trend for the centring of the ridge in the $x = 0.275$ is the same as that observed in figures 7.11 and 7.12 for the $x = 1/3$.
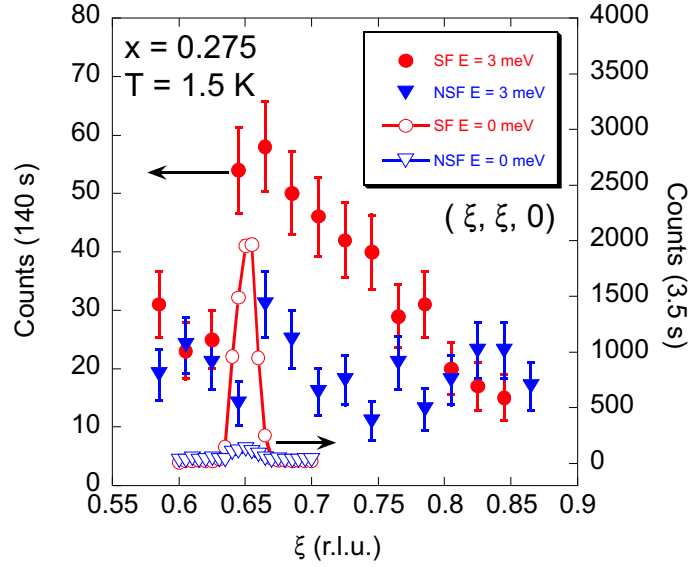
Figure 7.16: Polarized SF and NSF scattering along the (1, 1, 0) direction of the $x = 0.275$ for elastic scattering and an energy transfer of 3 meV.

We then performed polarized-neutron scattering measurements with the neutron polarization **P** parallel to the scattering vector **Q** on the $x = 0.275$, using the triple-axis spectrometer IN20. Figure 7.16 shows SF and NSF scattering from the $x = 0.275$ along a line equivalent to path A, for both elastic scattering and $E = 3$ meV. The elastic scattering shows the magnetic Bragg stripe superlattice peak in the SF channel centred on $\xi \sim 0.65$. For $E = 3$ meV no peak was observed in the NSF scattering but a broad peak centred on $\xi \sim 0.7$ is observed in the SF scattering. Excitations from the stripe superlattice can only be responsible for SF excitations on the left-hand-side of the peak at $E = 3$ meV, but the right-hand-side of the SF peak can be accounted for as originating from the ridge scattering. So the SF data in Fig. 7.16 on the $x = 0.275$ for $E = 3$ meV shows an unresolved peak due to two magnetic modes: excitations from the ordered Ni^{2+} spins and excitations from the ridge scattering. This result matches our observation of a magnetic origin for the ridge scattering in the $x = 1/3$.
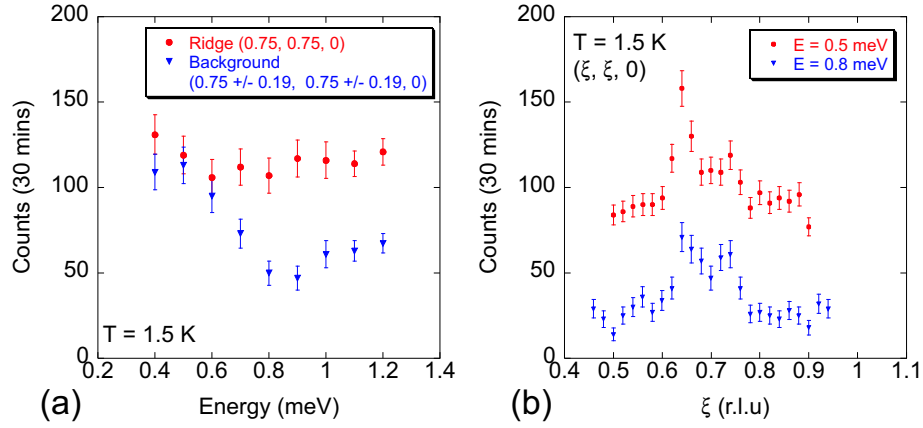
Figure 7.17: (a) A scan at constant **Q** of the energy variation of the ridge scattering amplitude intensity in the $x = 0.275$ at $T = 1.5$ K. The background scattering is estimated from an average of scans centred away from the magnetic excitations at equidistant larger and smaller wavevectors. (b) Constant energy scans along the (1, 1, 0) direction of reciprocal space for the $x = 0.275$ at $T = 1.5$ K for 0.5 and 0.8 meV. The 0.8 meV scan has been offset by the addition of 50 counts for clarity.

We carried out a preliminary investigation of the ridge scattering in both the $x = 0.275$ and 1/3 for $E < 2$ meV on the cold triple-axis spectrometer RITA II. In figure 7.17 I show the main results of this work for the $x = 0.275$, with the data taken on the $x = 1/3$ showing similar trends to those observed in the $x = 0.275$. Figure 7.17(a) shows a scan performed at a constant **Q** of the energy variation of the amplitude intensity of the ridge scattering and the background for the $x = 0.275$. For decreasing energy the amplitude of the ridge scattering remains roughly constant from 1.2 down to 0.8 meV, then the intensity of the ridge scattering decreases to zero within experimental error by 0.6 meV. To try to confirm the lack of the ridge scattering for $E < 0.6$ meV we performed constant energy scans at 0.8 and 0.5 meV along a line equivalent to path A. Figure 7.17(b) shows the data from these scans on the $x = 0.275$. For $E = 0.8$ meV the ridge scattering is clearly observed and centred on $\xi = 0.73$, but at $E = 0.5$ meV we still observe a small excess of scattering above the background at $\xi = 0.73$, which may or may not be statistical in origin. Further

work on the low energy excitations of the ridge scattering with greater neutron flux and longer counting times are required to determine if the ridge excitations are gapped with a gap energy of $\sim 0.8\,\mathrm{meV}$. From the width of the ridge peak at $E = 0.8\,\mathrm{meV}$ on the $x = 0.275$ and $1/3$ we obtain a correlation length of $\sim 35\,\text{Å}$(the inverse of the half width at half maximum).

7.3.1 Discussion

We have observed that the low energy excitation spectrum of La$_{2-x}$Sr$_x$NiO$_4$ for $x = 1/3$ and 0.275 contains two separate magnetic modes: excitations from the ordered Ni^{2+} spins and diffuse diagonal 'ridges' of excitations. The 'ridge' scattering has little modulation along it's length in the $(h,\ k)$ plane, and no modulation along the l direction. There is only a sizeable correlation length in the direction perpendicular to the ridges. This means the scattering is quasi-one-dimensional running parallel to the diagonals of the square lattice of the ab plane, i.e. the correlations are parallel to the stripe directions.

One model system which is known to exhibit one dimensional spin fluctuations is non-interacting 1-D spin chains. To understand the ridge scattering we observe in La$_{2-x}$Sr$_x$NiO$_4$ we considered a system of non-interacting antiferromagnetic (AFM) spin chains running parallel to the direction $\mathbf{d} = [1,\ 1,\ 0]$ of a square lattice, with spins attached to vertices of the lattice, as in Fig. 7.10(b). For the case of spin-1/2 Heisenberg chains the main mode of the excitation spectrum would be given by[100]

$$E(\mathbf{Q}) = \pi J |sin(2\pi\mathbf{Q}.\mathbf{d})| \tag{7.2}$$

where J is the exchange energy per spin. If we consider the excitations for energies approaching zero, the scattering cross section will be largest when $\mathbf{Q}.\mathbf{d}$ is an odd half

integer and zero when **Q**.**d** is an integer. This ordering would produce scattering that lies along the dashed diagonal lines of Fig. 7.10(a), which would be centred in scans equivalent to path A at **Q** = (0.25, 0.25), whereas a twin domain with ordering along **d** = [−1, 1, 0] would produce scattering that lies along the solid diagonal lines of Fig. 7.10(a).

The ridge scattering we observe in Fig. 7.9 on $x = 1/3$ and Fig. 7.15(a) on $x = 0.275$ closely resembles that expected for non-interacting 1-D spin chains. The scattering in these figures shows no modulation with l and only a small modulation along the ridge, the ridge only shows significant modulation in the direction parallel to the stripe direction, therefore the ridge scattering is quasi-one dimensional. There is one discrepancy between the model and the observed ridge scattering: the flexing in wavevector of the ridges. The ridge scattering is observed to be centred at $\xi = 0.27$ for scans along path A, whereas non-interacting 1-D antiferromagnetic spin chains would have scattering centred at $\xi = 0.25$ for scans performed along path A.

Polarized neutron analysis of the spin fluctuations at 2 meV revealed the ridge scattering to be anisotropic, with fluctuations primarily out-of-plane. Our work on the spin wave excitations of the ordered Ni^{2+} spins revealed that below ~ 7 meV the fluctuations lie in-plane. In figure 7.14 I showed the temperature dependence of the ridge scattering, we observed the intensity of the ridge scattering to decrease with temperature persisting only up to ~ 100 K. Previous work on the low energy spin wave excitations of the ordered Ni^{2+} spins revealed that the correlations persist up to ~ 200 K[33]. Adding to these two differences the fact that the excitations of the ordered Ni^{2+} spins are localized in **Q** while the ridge scattering is spread out in **Q**, our results imply that the ridge scattering does not originate from the ordered Ni^{2+} spins.

As the ridge scattering is not from the AFM ordered Ni^{2+} spins, we propose that the origin of the ridge scattering is from AFM spin correlations of charge stripes. Assuming the charge stripes are centred on the Ni sites (see chapter 1.3.3), the charge stripes are diagonal lines of Ni^{3+} ions, which in the strong crystal field limit would have $S = 1/2$. Using this interpretation, we have observed 1-D AFM excitations from quasi-1-D spin-1/2 chains that are dynamic on the timescale probed by neutrons and correlated over a length scale of ~ 35 Å. Hence, we can estimate the strength of the exchange interaction for these correlations using equation 7.2 to be $J \approx 3.2$ meV. This fit produces the solid line dispersion I plot in Fig. 7.13(b).

As we have observed the ridge scattering in the incommensurately ordered $x = 0.275$, the quasi-1-D AFM excitations appear to be a property intrinsic to the charge stripes of La$_{2-x}$Sr$_x$NiO$_4$, not a commensurate ordering effect. These results are to our knowledge the first evidence of spin correlations from the charge carriers in a charge-ordered material. To theoretically model charge-order accurately it is important to understand the correlations of both the ordered spins and the charge carriers. Hence these results provide the first indication of how the spins of the charge carriers correlate, which could help in the understanding of the role of charge stripes in high temperature superconductors.

There are however limits to what can be inferred about charge stripes in the cuprate high temperature superconductors from the nickelates. This is due to the differences of the stripes in these materials. As outlined in chapter 1, the orientation of the stripes in the superconducting cuprates is horizontal and vertical[19, 20, 22], as opposed to the diagonally orientated stripes of the nickelates. In the nickelates the stripes are half filled and thus insulating, but in the superconducting cuprates the stripes are quarter filled and metallic. Despite these differences useful information about charge-ordered states can be

obtained from studying the nickelates that will help our understanding of the role of charge stripes in the cuprates. If we can understand the ordering phenomena in a model charge-ordered system such as La$_{2-x}$Sr$_x$NiO$_4$ then we will be in a better position to understand their role in the cuprate superconductors. Our observation of AFM correlations in the nickelate stripes when ferromagnetic stripes have been predicted[101], is significant in understanding the coupling of the charge stripes to the AFM background. From the insights of our work we should also be in a position to better understand the mechanism for the intrastripe exchange interaction in charge-ordering.

Chapter 8

Spin Dynamics of Half-Doped

La$_{3/2}$Sr$_{1/2}$NiO$_4$

In this chapter I present inelastic neutron scattering experiments on La$_{3/2}$Sr$_{1/2}$NiO$_4$[102]. The aim of this work was to determine the effect that near 2-D checkerboard charge-ordering has on the magnetic excitations in La$_{2-x}$Sr$_x$NiO$_{4+\delta}$, compared to the magnetic excitations of charge-stripe ordered La$_{2-x}$Sr$_x$NiO$_4$ (see chapter 7).

In this work I present polarized- and unpolarized- inelastic neutron scattering measurements of the magnetic excitation spectrum in the spin-charge ordered phase of La$_{3/2}$Sr$_{1/2}$NiO$_4$. Up to energies of $\sim$30 meV we observe broad magnetic modes characteristic of a near checkerboard ordering. A linear spin-wave model for an ideal checkerboard ordering with a single antiferromagnetic exchange interaction $J' = 5.8 \pm 0.5$ meV between next-nearest-neighbour spins on Ni^{2+} sites, together with a small XY-like single-ion anisotropy, provides a reasonable description of the measured dispersion. Above 30 meV the excitations are not fully consistent with the linear spin-wave model, with modes near the two-dimensional reciprocal space wavevector $(0.5, 0.5)$ having an anomalously large intensity. Furthermore, two additional dispersive modes not predicted by the simple linear

spin wave theory are observed, both of which are probably magnetic. One disperses away from $(0.5, 0.5)$ in the energy range between 50–56 meV, and the other appears around (h, k) type positions $(h, k = \text{integer})$ in the energy range 31–39 meV. We propose a model in which these anomalous features are explained by the existence of discommensurations in the checkerboard ordering. At low energies there is additional diffuse scattering centred on the magnetic ordering wavevector. We associate this diffuse scattering with dynamic antiferromagnetic correlations between spins of the charge carriers.

8.1 Static order of x=0.5

To aid the description of excitations in the $x = 0.5$ material I will again outline the known static order of the $x = 0.5$. Figure 8.1 illustrates how the different ordered phases in $La_{3/2}Sr_{1/2}NiO_4$ can be identified in diffraction measurements. Figure 8.1(a) is a simplified model of the ground state spin–charge order within the NiO_2 layers of $La_{3/2}Sr_{1/2}NiO_4$ neglecting the small incommensurate modulation. I assume the doped holes are site-centred, so that the checkerboard pattern is derived from alternating Ni^{2+} and Ni^{3+} ions carrying spins $S = 1$ and $S = \frac{1}{2}$, respectively. The $S = 1$ spins are assumed to be ordered antiferromagnetically, but no assumption is made at this stage about magnetic order of the $S = \frac{1}{2}$ spins (this issue will be addressed later in the chapter). The positions in reciprocal space of the corresponding Bragg peaks are shown in Fig. 8.1(b). Peaks from the charge order have two-dimensional wave vectors (in units of $2\pi/a$) $(h + \frac{1}{2}, k + \frac{1}{2})$, where h and k are integers[1]. The magnetic order has double the periodicity of the charge order, so peaks from the magnetic order appear at $(h + \frac{1}{2}, k + \frac{1}{2}) \pm (\frac{1}{4}, \frac{1}{4})$. Rotation of the ordering pattern by 90° generates an equivalent magnetic structure, this time with magnetic peaks at $(h + \frac{1}{2}, k + \frac{1}{2}) \pm (\frac{1}{4}, -\frac{1}{4})$. In the absence of a symmetry-breaking interaction we expect an equal population of these two domains, so the pattern of Bragg peaks will be a superposition, as shown in Fig. 8.1(b).

The actual spin–charge ordered phase of $La_{3/2}Sr_{1/2}NiO_4$ observed below T_{ICO} does not conform to the ideal structure shown in Fig. 8.1(a). Instead, the magnetic Bragg peaks are found at the incommensurate positions $(h+\frac{1}{2}, k+\frac{1}{2}, l) \pm (\epsilon/2, \epsilon/2, 0)$ with l an odd integer, and $(h+\frac{1}{2}, k+\frac{1}{2}, l) \pm (\epsilon/2, -\epsilon/2, 0)$ with l an even integer, where $\epsilon \approx 0.44$ [34, 38, 89]. New

---

[1] In this work we describe the structural properties of $La_{2-x}Sr_xNiO_{4+\delta}$ with reference to a tetragonal unit cell with cell parameters $a \approx 3.8$ Å and $c \approx 12.7$ Å.
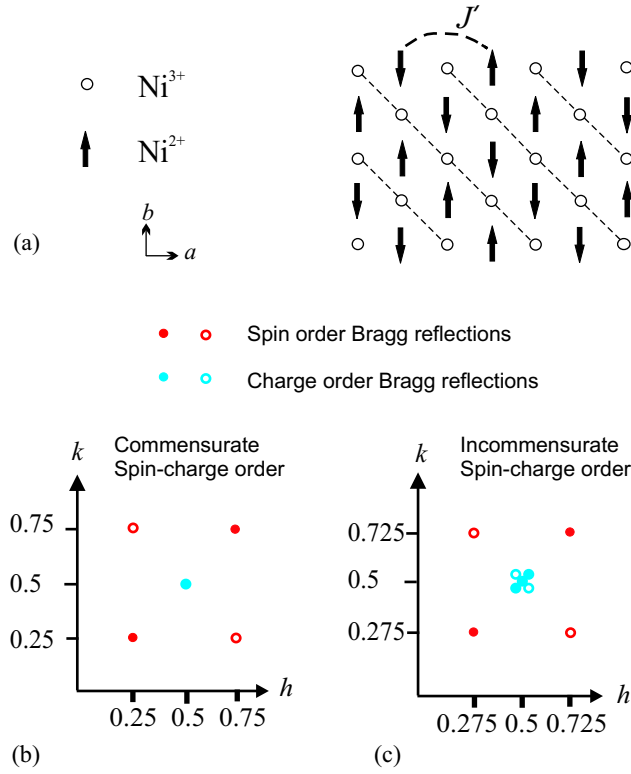
Figure 8.1: (a) Ideal checkerboard spin–charge ordering in a NiO$_2$ square lattice. Circles represent Ni^{3+} holes, and solid arrows represent spins on Ni^{2+} sites. The broken lines are included to highlight that the spin pattern breaks the 2D symmetry of the checkerboard charge ordering. J' is the exchange coupling parameter of the Ni^{2+} spins across the Ni^{3+} site. This commensurate ordering is not realized in practise in La$_{3/2}$Sr$_{1/2}$NiO$_4$. (b) Diagram of part of the (h, k) plane in 2D reciprocal space showing the positions of the first-order magnetic and charge order Bragg peaks for the ideal checkerboard ordering represented in (a). The peaks from the equivalent domain in which the magnetic ordering is rotated by 90 degrees relative to that in (a) are superimposed. (c) The same diagram as (b) except with the magnetic and charge order Bragg peaks observed in the incommensurate ordered phase of La$_{3/2}$Sr$_{1/2}$NiO$_4$. For simplicity we neglect the variation in the peak positions in the direction perpendicular to the NiO$_2$ plane.

charge-order satellite peaks appear at $(h \pm \epsilon, k \pm \epsilon)$ in addition to the checkerboard charge order peak at $(h + \frac{1}{2}, k + \frac{1}{2})$, with little or no l dependence[38, 89]. The full set of 2D magnetic and charge order wavevectors for the incommensurate phase of La$_{3/2}$Sr$_{1/2}$NiO$_4$, including those for the 90 deg domain, is shown in Fig. 8.1(c).

Kajimoto *et al.*[38] suggested that two types of charge order coexist in the incommensurate phase, one part of the system being charge-ordered in a checkerboard pattern and the other part adopting an incommensurate, stripe-like, spin-charge order. These authors developed models for the latter component based on the introduction of diagonal discommensurations in the ideal checkerboard spin-charge structure of Fig. 8.1(a). As pointed out by Kajimoto *et al.*, the stability of the incommensurate structure is probably the result of a competition between magnetic and electrostatic energy. The strong superexchange interaction favours having antiparallel spins on nearest neighbour Ni sites, whereas the Coulomb interaction tries to have a uniform charge density.

8.2 Experimental details

The neutron scattering measurements in this chapter were performed on a single crystal of La$_{3/2}$Sr$_{1/2}$NiO$_4$ grown by the floating-zone method[81] (see chapter 4). The crystal was a cylinder 35 mm in length and 7 mm in diameter. The oxygen content of the crystal was determined by thermogravimetric analysis (TGA) to be 4.02 ± 0.01. This is the same crystal that was used in our earlier neutron diffraction and magnetization study of the magnetic order (see chapter 6).

The majority of the unpolarized-neutron scattering measurements were performed on the time-of-flight chopper spectrometer MAPS at the ISIS Facility. The crystal was mounted on MAPS in a closed-cycle refrigerator and aligned with the c axis parallel to the incident beam direction. A Fermi chopper was used to select the incident neutron energy. Incident energies of 60 and 100 meV were used. The intensity was normalized and converted to units of scattering cross-section (mb sr^{-1} meV^{-1} [f.u.]$^{-1}$) by comparison with measurements from a standard vanadium sample. Scattered neutrons were recorded in large banks of position-sensitive detectors. The spin dispersion was found to be highly two dimensional. Hence, we analyzed the data by making a series of constant energy slices and projecting the intensities onto the (h, k) two-dimensional reciprocal lattice plane. For an incident energy of 60 meV the resolution was typically 2.2 meV in energy and 0.05 Å^{-1} in wavevector, whereas for an incident energy of 100 meV the resolution was typically 3.8 meV and 0.07 Å^{-1}.

Further unpolarized- and polarized-neutron measurements were performed on the triple-axis spectrometers IN8 and IN20 at the Institut Laue-Langevin. The energies of the incident and scattered neutrons were selected by Bragg reflection from a double-focusing

bent Si crystal monochromator on IN8, and an array of Heusler alloy crystals on IN20. On both instruments the data were obtained with a final neutron wavevector of $2.66\,\text{Å}^{-1}$, and a pyrolytic graphite (PG) filter was placed between the sample and analyzer to suppress higher-order harmonic scattering. For polarized-neutron scattering on IN20 the spin polarization, $\mathbf{P}$, was maintained in a specified orientation with respect to the neutron wavevector, $\mathbf{Q}$, by an adjustable guide field of a few mT at the sample position. For the experiment on IN8 the crystal was orientated with the [100] and [010] crystal directions in the horizontal scattering plane, so that $(h, k, 0)$ positions in reciprocal space could be accessed. On IN20, we mounted the crystal with the [001] and [110] directions in the horizontal scattering plane, so that (h, h, l) positions in reciprocal space could be accessed. At any energy transfer of $30\,\text{meV}$ the resolution of the IN8 instrument was $4\,\text{meV}$ in energy, $0.13\,\text{Å}^{-1}$ in wavevector parallel to the scan direction, $0.2\,\text{Å}^{-1}$ in wavevector perpendicular to the scan in the scattering plane and $0.2\,\text{Å}^{-1}$ in wavevector out of the scattering plane. For an energy transfer of $3\,\text{meV}$ the resolution was $1.4\,\text{meV}$, $0.08\,\text{Å}^{-1}$ in the scattering plane and $0.8\,\text{Å}^{-1}$ out of the scattering plane. On IN20 the typical resolution of the instrument was $2.0\,\text{meV}$ in energy, $0.06\,\text{Å}^{-1}$ in wavevector in the scattering plane and $0.15\,\text{Å}^{-1}$ out of the scattering plane.

8.3 Results

Figures 8.2(a)−(c) show constant-energy slices from runs performed at $T = 10\,\mathrm{K}$ on MAPS[2]. The slices have been averaged over a range of energies, as indicated in the figures. In (a), the range is 4–6 meV, and the intensity is seen to be enhanced at the four equivalent magnetic order wavevectors $(0.5, 0.5) \pm (\epsilon/2, \epsilon/2)$ and $(0.5, 0.5) \pm (\epsilon/2, -\epsilon/2)$, where $\epsilon \approx 0.44$. This signal, therefore, corresponds to low energy spin excitations from the magnetically ordered ground state. As the energy increases, the intensity spreads out but initially remains centred on the magnetic wavevectors. This can be seen in Fig. 8.2(b), which shows data averaged over 25–30 meV. At still higher energies the four blobs of intensity tend to merge towards $(0.5, 0.5)$. This is illustrated in (c), which corresponds to an energy range 40–45 meV.

In Figs. 8.2(d)–(f) I plot cuts through the data in the (ξ, ξ) direction for the same energy ranges as used in Figs. 8.2(a)–(c). At low energies, $E = 4 - 6$ meV, the scattering takes the form of a single peak centred on the magnetic wavevector. The fitted Gaussian width of this peak converts to a correlation length of 35 ± 1 Å(the inverse of the half width at half maximum). At energies of 25–30 meV (Fig. 8.2(e)) the lineshape is also centred on the magnetic wavevector, but it now contains two peaks which can just be resolved (another

---

[2]On a time-of-flight spectrometer with the incident neutron beam parallel to the c axis the out-of-plane wavevector component l varies with the excitation energy, and depends also on the incident neutron energy. The l values for the data shown in Fig. 8.2 are given in the figure caption. Although the magnetic excitation spectrum of La$_{2-x}$Sr$_x$NiO$_4$ is highly two-dimensional, the scattering intensity does vary with l. The variation is smooth, and depends partly on the magnetic form factor and partly on the direction of $\mathbf{Q}$, since neutrons scatter from spin fluctuations perpendicular to $\mathbf{Q}$. The ordered moment in La$_{3/2}$Sr$_{1/2}$NiO$_4$ lies in the ab plane, so the scattering becomes less sensitive to magnetic fluctuations parallel to the c axis as l increases.

Figure 8.2: Neutron scattering measurements from La$_{3/2}$Sr$_{1/2}$NiO$_4$ measured on MAPS at $T = 10$ K. $(a) - (c)$ are constant-energy slices showing the variation of the intensity in the (h, k) plane at different energies. The data are averaged over the range of energies indicated above the figures. The incident neutron energy was 60 meV for (a), and 100 meV for (b) and (c). Data from four equivalent Brillouin zones have been averaged. $(d) - (f)$ show cuts along the (ξ, ξ) direction for the same energies as shown in $(a) - (c)$. The solid lines are the results of fits with one Gaussian [(d) and (f)] or two Gaussians [(e)] on a linear background. In (d) we also display the $(0.275, 0.275, 5)$ magnetic order Bragg peak measured on IN20. The out-of-plane wavevectors for the position $(0.275, 0.275)$ are as follows: $(a)\&(d)$ $l = 0.55$, (b) $l = 2.3$, (e) $l = 3.0$, (c) $l = 3.45$ and (f) $l = 5.2$.

example can be seen in Fig. 8.6(c)). The fitted width of these peaks corresponds to a correlation length of 24 ± 2 Å. As the energy increases, the right-hand of the two peaks grows while the left-hand peak diminishes. This asymmetry is not instrumental in origin,

e.g. a resolution or background effect, because we observe it in scans measured under very different conditions on different spectrometers. Above $E \approx 40$ meV the left-hand peak has virtually no intensity, as can be seen in Fig. 8.2(f).
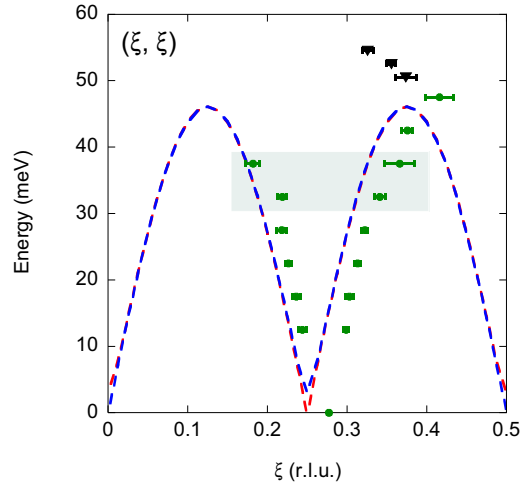
Figure 8.3: Dispersion of the magnetic excitations in La$_{3/2}$Sr$_{1/2}$NiO$_4$ parallel to the (ξ, ξ) direction. The points are the results of fits to cuts such as those shown in Fig. 8.2. The broken lines are calculated from Eq. (8.2), the spin wave dispersion for a checkerboard ordered system with exchange parameter $J' = 5.8$ meV and out-of-plane anisotropy $K_c = 0.05$ meV. The two branches of the dispersion curve are separated at low energies by a small anisotropy gap which can clearly be seen in Fig. 8.7(b). Triangles above the calculated dispersion curve indicate the positions of an additional observed scattering mode. The shaded area represents the region in which additional scattering hampers the study of the spin-wave excitations, see Fig. 8.5.

Figure 8.3 shows the dispersion of the spin excitations obtained from Gaussian fits to the peaks observed in cuts such as those displayed in Fig. 8.2(d)–(f). The points in Fig. 8.3 are the fitted peak centres corrected for the effect of the non-zero width of the cut perpendicular to the cut direction. For this purpose the scattering was taken to be a circle centred on the magnetic wavevector. Within the experimental limits of our data

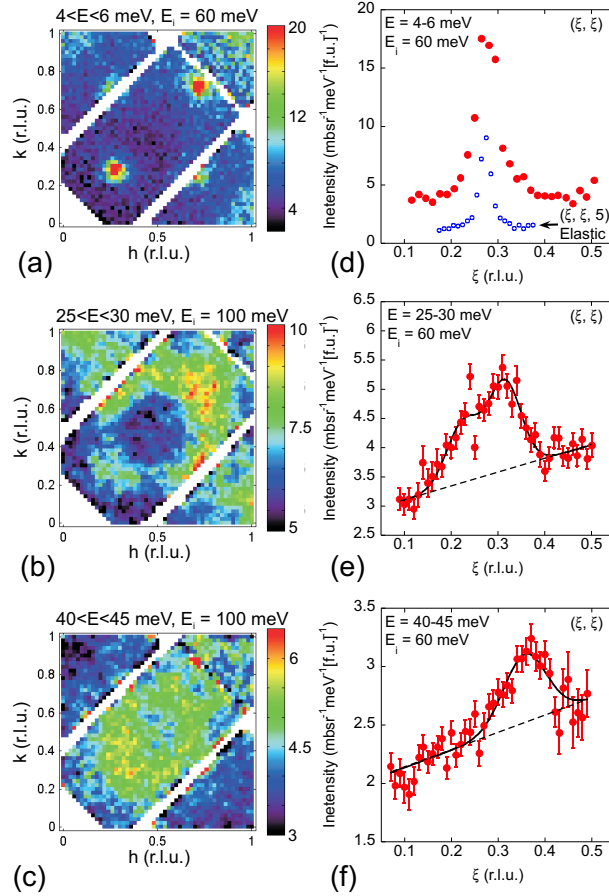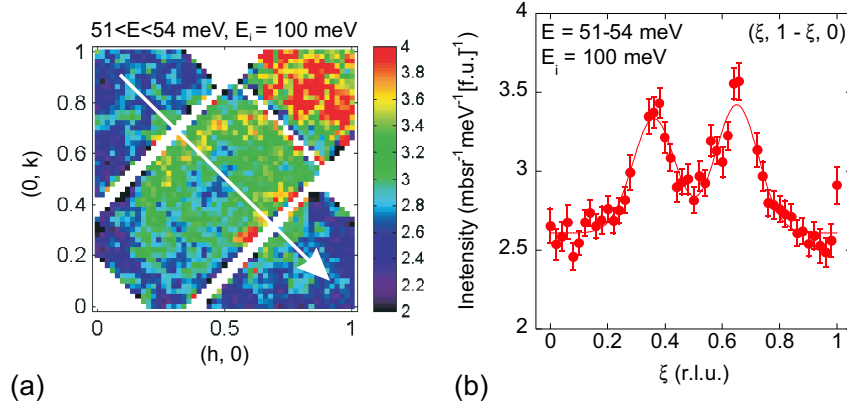Figure 8.4: Neutron scattering measurements from La$_{3/2}$Sr$_{1/2}$NiO$_4$ measured on MAPS at $T = 10$ K. (a) Constant-energy slice through the data showing the intensity distribution in the (h, k) plane in the energy range 51–54 meV. The slice reveals weak diffuse scattering symmetrically distributed around $(0.5, 0.5)$. Data from four equivalent Brillouin zones have been averaged to improve the statistics. (b) Cut through the 51–54 meV slice along the path indicated by the arrow in (a).

the dispersion was found to be the same in orthogonal cut directions.

In constructing the dispersion curve we had to take care to avoid confusing the scattering from magnetic excitations and phonons, especially in the energy range 10–40 meV where the phonon scattering is particularly strong. One check we made was to compare data obtained at 300 K with that obtained at 10 K. Phonon scattering increases in strength with temperature, whereas magnetic scattering decreases in strength above the magnetic ordering temperature.

At energies above 50 meV we observed a broad ring of scattering centred on $(0.5, 0.5)$. This is illustrated in Fig. 8.4, which shows (a) a constant-energy slice averaged over the energy range 51–54 meV, and (b) a cut through this data along the line $(\xi, 1 - \xi)$. This mode disperses away from $(0.5, 0.5)$ with increasing energy, but was too weak to measure
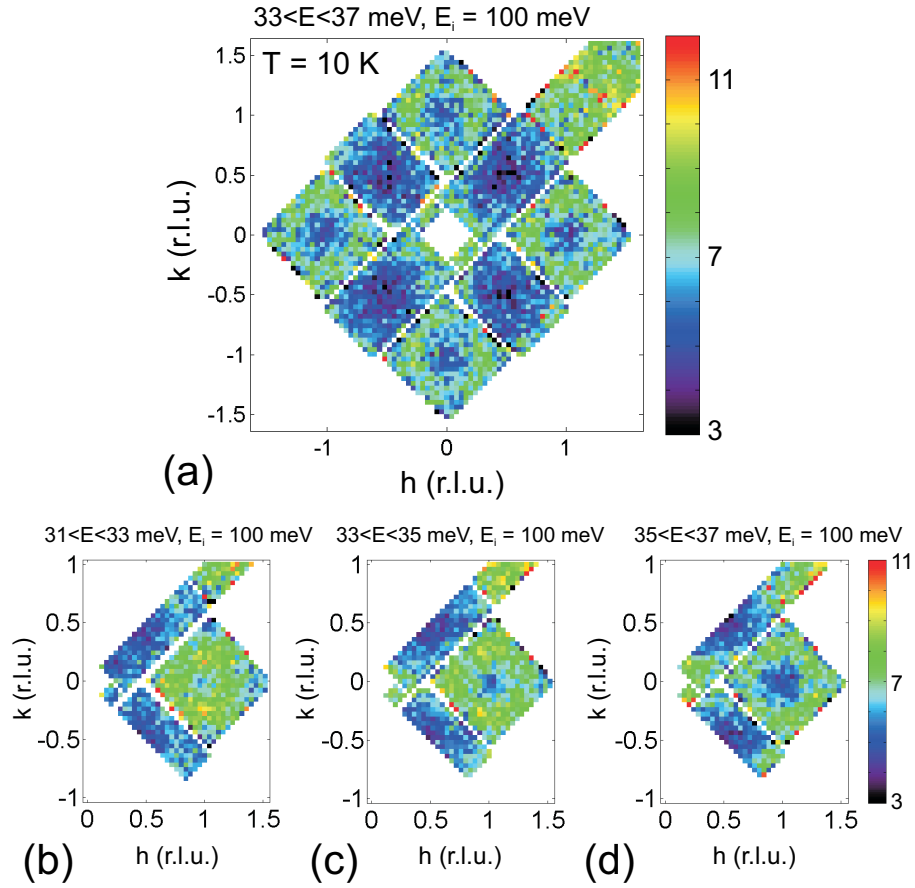
Figure 8.5: Excitations from La$_{3/2}$Sr$_{1/2}$NiO$_4$. (a) Distribution of scattering intensity in the $(h,\ k)$ plane measured on MAPS at $T = 10\,\mathrm{K}$. The scattering has been averaged over the energy range $E = 33 - 37\,\mathrm{meV}$. (b)–(d) Slices through the scattering intensity measured at $T = 10\,\mathrm{K}$ in the $(h\ ,k)$ plane averaged over the energy ranges (b) $31 - 33\,\mathrm{meV}$, (c) $33 - 35\,\mathrm{meV}$, (d) $35 - 37\,\mathrm{meV}$. The data in the MAPS detector have been folded to take advantage of the symmetry of the scattering.

above $56\,\mathrm{meV}$. This scattering was found to be slightly weaker at $300\,\mathrm{K}$ than at $10\,\mathrm{K}$, which suggests a magnetic origin for it. I have added the peak positions of this scattering to the dispersion curve in Fig. 8.3.

In the energy range $31 - 39\,\mathrm{meV}$ we observed an interesting scattering feature separate from the main spin wave scattering. Figure 8.5(a) shows the distribution of intensity measured on MAPS for energies averaged over the range 33–37 meV covering a large area

of reciprocal space. This intensity map displays strong diffuse scattering rings centred on the reciprocal lattice zone centres (h, k), where h and k are integers. Figures 8.5(b)– (d) present constant-energy slices through this scattering centred on energies of 32 meV, 34 meV and 36 meV. In these slices the symmetry-equivalent data have been folded into one quadrant to improve the statistics. The intensity is seen to disperse away from the $(1, 0)$ point. In these measurements the out-of-plane component of the scattering vector varies from $l = 2.5$ to 4. A search was made with the IN8 spectrometer of other Brillouin zones in the $(h, k, 0)$ reciprocal lattice plane. This survey confirmed the results found on MAPS, showing that the scattering was not restricted to a particular out-of-plane component of the scattering vector.

To assess whether or not this scattering is magnetic in origin we performed measurements as a function of temperature. Cuts through the MAPS data at 10 K and 300 K are shown in Fig. 8.6(a). These data show the scattering to decrease slightly with temperature, being approximately $45 \pm 12\%$ stronger at 10 K than at 300 K. We also observed similar scattering in the range 25–30 meV. Fig.8.6(b) shows $\mathbf{Q}$ scans through the point $(2, 0, 0)$ at an energy of 25 meV for temperatures of 1.5 K and 300 K, measured on IN8. The scattering here appears to be temperature independent. To understand these temperature effects we need to take into account that this diffuse scattering ring overlaps the magnetic ordering wavevectors, so will contain some spin-wave scattering. The spin wave scattering itself will, of course, be temperature dependent. To illustrate this we show in Fig. 8.6(c) scans through the spin-wave scattering associated with the magnetic wavevector $(1.5, 1.5) - (\epsilon/2, \epsilon/2)$ measured at a slightly higher energy ($E = 30$ meV) on IN8 at $T = 1.5$ K and 300 K. The amplitude of the spin wave scattering clearly decreases with temperature. From this loss of intensity we can infer the temperature dependence of
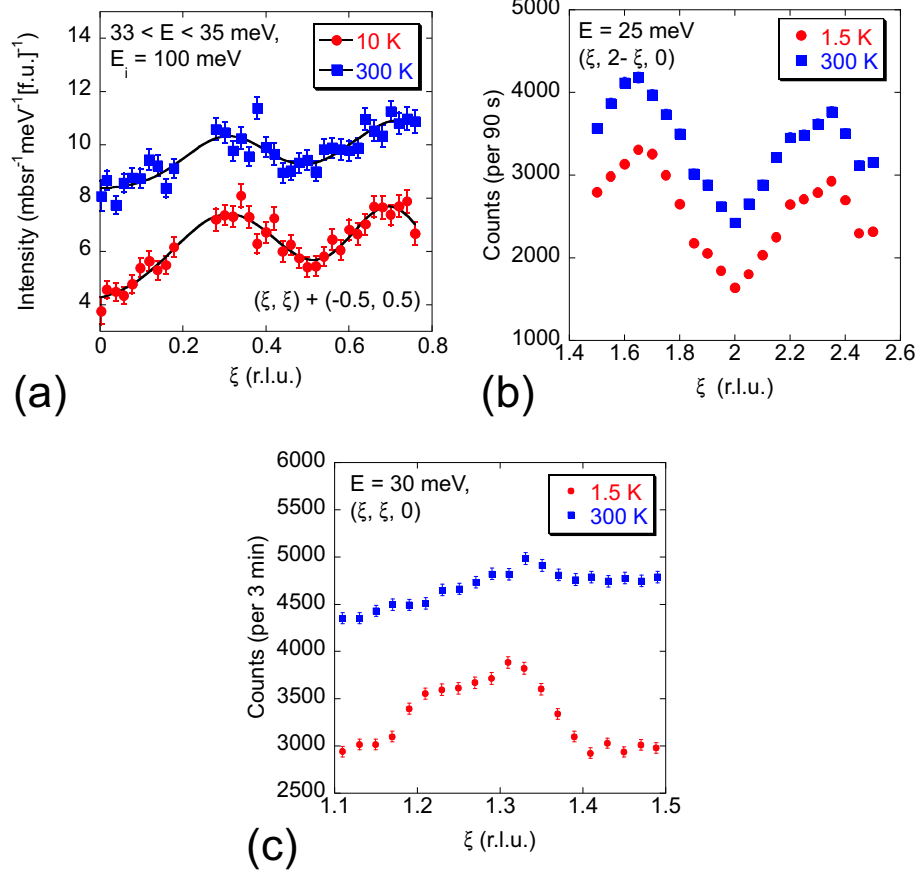
Figure 8.6: (a) Cuts through the data shown in 8.5(c) along a line parallel to the (h, h) direction passing through $(1, 0)$. The data at $T = 10\,\text{K}$ and $300\,\text{K}$, have been offset by 5 units. The lines in (b) are the result of fitting the points with two gaussian functions on a sloping background. (c) Scans of the scattering observed at $E = 25\,\text{meV}$ for $T = 1.5\,\text{K}$ and $300\,\text{K}$ measured on IN8. (g) A scan through the spin wave dispersion at $E = 30\,\text{meV}$ for $T = 1.5\,\text{K}$ and $300\,\text{K}$ measured on IN8. The $300\,\text{K}$ data in (b) and (c) have been offset by the addition of 1000 counts.

the remaining component of the scattering in Figs. 8.5(a)–(d) and Figs. 8.6(a)–(b). Our analysis indicates that at $E \sim 35\,\text{meV}$ the non-spin-wave component of the diffuse scattering ring presented in Figs. 8.5(a)–(d) decreases in intensity with temperature, whereas at $E = 25\,\text{meV}$ (Fig. 8.5(b)) it increases with temperature. This leads us to conclude that the diffuse scattering around the Brillouin zone centres shown in Figs. 8.5(a)–(d) is most likely magnetic in origin.

Further support for this conclusion was provided by examining data we have collected on crystals of La$_{2-x}$Sr$_x$NiO$_4$ with $x = 1/3$ and 0.275 under similar condition during a separate experiment on MAPS[99] (see chapter 7.2). Constant-energy slices for $x = 1/3$ and 0.275 in the energy range $31 - 39$ meV do not show any diffuse scattering rings like those shown in Figs. 8.5(a)–(d), so this feature seems to be specific to $x = 1/2$. This makes it highly unlikely that this scattering comes from phonons intrinsic to the host lattice of La$_{2-x}$Sr$_x$NiO$_4$.

For energies below 30 meV we performed additional measurements with polarized neutrons. In this energy range there is strong scattering from phonons, and polarized neutrons were necessary to provide an unambiguous separation of the magnetic and non-magnetic scattering. We were particularly interested in studying the magnetic scattering as a function of energy because earlier measurements on La$_{2-x}$Sr$_x$NiO$_4$ compositions with $x = 0.275$, 0.33 and 0.37 had revealed unexpected structure in the energy spectrum (see chapter 7.2). For these measurements the neutron polarization $\mathbf{P}$ was aligned parallel to the scattering vector $\mathbf{Q}$ so that the spin-flip (SF) channel would contain purely magnetic scattering.

The most interesting finding is reproduced in Fig. 8.7, which shows energy scans measured in the SF channel on samples with compositions $x = 1/3$ and $x = 1/2$ at their respective magnetic ordering wavevectors. The $x = 1/3$ data contains two peaks, one centred on 7 meV and the other on 26 meV. The $x = 1/2$ data contains a single peak at 5 meV. The lower energy peaks were shown to be gaps due to spin anisotropy (see chapter 7.2). Below these gaps the out-of-plane spin fluctuations are quenched. The origin of the higher energy peak in the $x = 1/3$ data, which was also found in similar data from crystals with $x = 0.275$ and $x = 0.37$, remains a mystery (see chapter 7.2 for a discussion of this
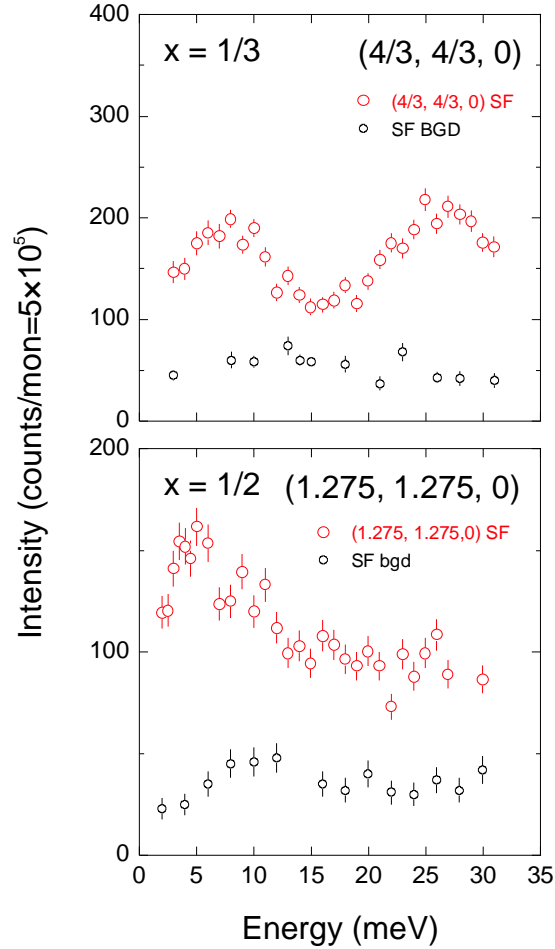
Figure 8.7: Polarized-neutron scattering from charge-ordered La$_{2-x}$Sr$_x$NiO$_4$ with $x = 1/3$ and $1/2$. The plots show energy scans performed at the magnetic ordering wavevector appropriate to each composition. The spin-flip (SF) scattering was measured with $\mathbf{P} \parallel \mathbf{Q}$, and the SF background was estimated from scans centred away from the magnetic ordering wavevector. The measurements were made at $10\,\mathrm{K}$ for $x = 1/2$ and $13.5\,\mathrm{K}$ for $x = 1/3$.

feature). Of all the compositions studied, the one with $x = 1/3$ exhibits this feature most strongly. The absence of a corresponding peak in the $x = 1/2$ data seems to suggest that this peak is a property of compounds with static stripe order with a periodicity of ~3 lattice spacings. The monotonic decrease in intensity above $5\,\mathrm{meV}$ in the $x = 1/2$
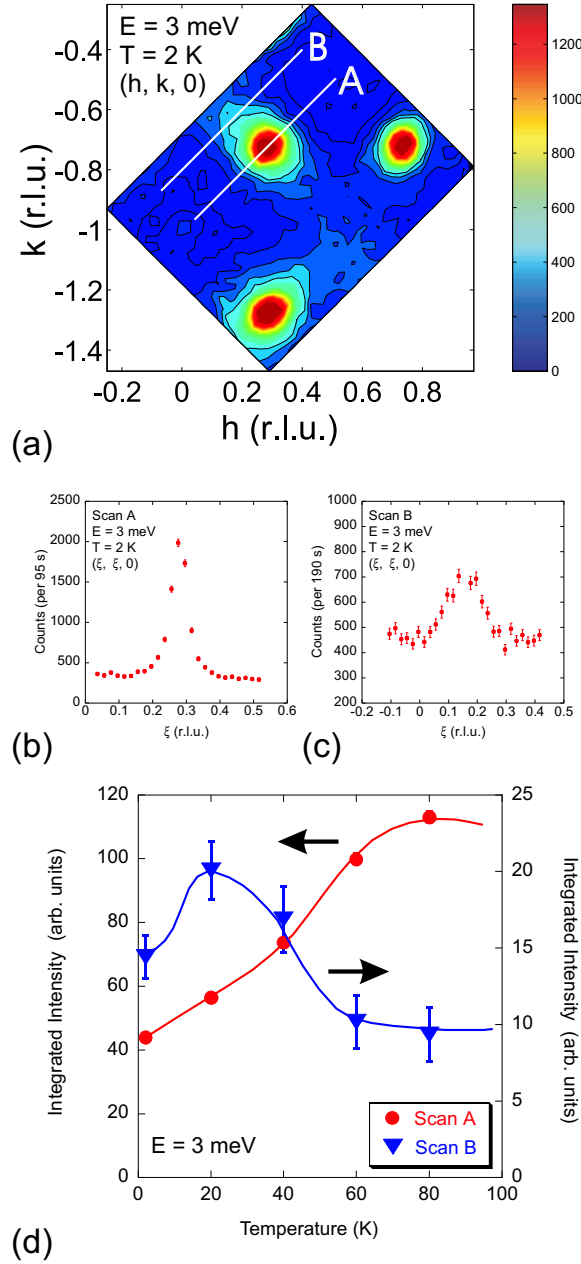
Figure 8.8: Low energy scattering from La$_{3/2}$Sr$_{1/2}$NiO$_4$ measured on IN8 at an energy of 3 meV and a temperature of 2 K. (a) Map of the scattering intensity in the $(h, k, 0)$ reciprocal lattice plane. (b) and (c) Cuts along the lines marked A and B in (a). (d) Temperature dependence of the integrated intensity of the peaks shown in (b) and (c). The lines are guides to the eye.

data is qualitatively consistent with the expected $1/E$ dependence of the cross section for scattering from antiferromagnetic spin waves.

Finally, we describe a feature observed in the scattering from La$_{3/2}$Sr$_{1/2}$NiO$_4$ at low ener-gies. Figure 8.8(a) is a map of the intensity measured on IN8 covering part of the $(h, k, 0)$ plane in reciprocal space. The map was constructed from a series of scans performed parallel to $(h, h, 0)$ at an energy of $3\,\mathrm{meV}$ and a temperature of $2\,\mathrm{K}$. Strong scattering can be seen centred on the magnetic ordering wavevectors, but additional weak diffuse scattering can also be seen centred on these same positions. This diffuse scattering is slightly elongated in the diagonal directions, parallel to the discommensuration lines in the distorted checkerboard structure. There was no observable elastic diffuse scattering, so this feature represents a short-range dynamic magnetic correlation. We were able to follow the diffuse inelastic scattering up in energy to $\sim 10\,\mathrm{meV}$.

In Fig. 8.8(b) and (c) are shown scans through the spin wave scattering and the diffuse scattering made along the lines marked A and B, respectively, in Fig. 8.8(a). Figure 8.8(d) displays the temperature dependence of the integrated intensity of the peaks in these two scans. The intensity for scan A is seen to increase with increasing temperature. This is due partly to thermal population of the spin waves, and partly to the reorientation of the ordered moment of the Ni^{2+} spins that takes place at $57\,\mathrm{K}$[89] (see chapter 5). Scan B, on the other hand, shows an initial increase in intensity on warming which peaks at around $20\,\mathrm{K}$ before decreasing at higher temperatures. This decrease suggests that the diffuse scattering is magnetic in origin, and the striking difference in temperature dependence between the spin wave scattering and the diffuse scattering strongly indicates that they arise from two different magnetic components in the system.

8.4   Discussion

Let me first summarize the key observations, and then provide some quantitative analysis. From the various neutron scattering measurements we have performed on spin- and charge-ordered La$_{3/2}$Sr$_{1/2}$NiO$_4$ we have been able to identify four distinct features: (1) dispersive spin excitation associated with the magnetic ordering wavevector; (2) low energy diffuse spin dynamics also associated with the magnetic ordering wavevector but with a distinct temperature dependence; (3) a probable magnetic mode dispersing from $(0.5, 0.5)$ at energies in the range 50–56 meV; (4) a probable magnetic mode dispersing from (h, k) type positions in the energy range 31–39 meV. All these features are relatively broad in wavevector, and therefore arise from dynamic correlations that are short-range in nature.

An obvious starting point for any analysis of the magnetic excitations in La$_{3/2}$Sr$_{1/2}$NiO$_4$ is the ideal checkerboard spin–charge ordering pattern shown in Fig. 8.1(a). As far as the spins are concerned, this is a simple two-sublattice antiferromagnet built from $S = 1$ spins on the Ni^{2+} sites. Spins attached to the Ni^{3+} sites are ignored for the time being. Following our previous work on stripe-ordered La$_{5/3}$Sr$_{1/3}$NiO$_4$[49], we adopt a spin Hamiltonian of the form

$$H = J' \sum_{\langle i,j \rangle} \mathbf{S}_i \cdot \mathbf{S}_j + K_c \sum_i (\mathbf{S}_i^z)^2, \tag{8.1}$$

where the first summation describes the exchange interactions between pairs of Ni^{2+} spins in linear Ni^{2+}–O–Ni^{3+}–O–Ni^{2+} bonds, and the second summation describes the small, XY-like, single-ion anisotropy. Here, as in Ref. [49], J' is defined as the exchange energy *per spin* (multiply by 2 to obtain the exchange energy *per bond*, i.e. the exchange energy *per pair of spins*). We neglect the diagonal exchange couplings between Ni^{2+} sites which

are needed to stabilize the spin arrangement but are assumed to be small relative to J'. In effect, therefore, the system is treated as 2 uncoupled square-lattice antiferromagnets with lattice parameter $2a$.

The magnon dispersion derived from Eq. (8.1) by standard linear spin wave theory (see Appendix A) is given by

$$E(\mathbf{Q}) = 8J'S\{(1 + K_c/8J')^2 - [\gamma(\mathbf{Q}) \pm K_c/8J']^2\}^{1/2}, \tag{8.2}$$

where

$$\gamma(\mathbf{Q}) = \frac{1}{2}[\cos(2Q_x a) + \cos(2Q_y a)]. \tag{8.3}$$

The splitting of the two branches of the dispersion curve is such that at the magnetic zone centre one mode is gapped and the other isn't. The size of the gap is $4S(2J'K_c)^{1/2}$. When $K_c \ll J'$ the maximum energy of the dispersion curve is approximately $8J'S$.

In Fig. 8.3 I have plotted the spin wave dispersion along the (ξ, ξ) direction calculated from Eq. (8.2) with $S = 1$, $J' = 5.8\,\mathrm{meV}$ and $K_c = 0.05\,\mathrm{meV}$. These parameters were chosen to match the observed maximum spin wave energy ($\sim 45\,\mathrm{meV}$) and anisotropy gap ($\sim 3\,\mathrm{meV}$). The spin-wave dispersion curve is seen to provide a reasonable description of the experimental data, apart from the obvious shift from the observed incommensurate wavevector $(0.275, 0.275)$ to the ideal checkerboard wavevector of $(0.25, 0.25)$. There is no detectable scattering from spin wave modes on the dispersion curve near $\xi = 0$ and $\xi = 0.5$ because the antiferromagnetic structure factor is small in the magnetic Brillouin zones centred on $(0, 0)$ and $(0.5, 0.5)$.

From this analysis we can give a rough estimate of the exchange and anisotropy parameters for La$_{3/2}$Sr$_{1/2}$NiO$_4$. After consideration of the experimental errors, these are $J' = 5.8 \pm 0.5\,\mathrm{meV}$ and $K_c = 0.05 \pm 0.02\,\mathrm{meV}$. It is interesting to compare these values with those

derived from similar spin-wave analyses performed on other La$_{2-x}$Sr$_x$NiO$_4$ compositions. For $x = 1/3$ the exchange parameters were found to be $J = 15 \pm 1.5$ meV, $J' = 7.5 \pm 1.5$ meV and $K_c = 0.07 \pm 0.01$ meV[49], where J is the exchange interaction between Ni^{2+} spins on nearest-neighbour lattice sites. For undoped La$_2$NiO$_4$ the results were $J = 15.5$ meV and $K_c = 0.52$ meV[98]. This comparison shows that J' and K_c are similar for $x = 1/3$ and $x = 1/2$, but that K_c is very much larger in undoped La$_2$NiO$_4$. An explanation for why the single-ion anisotropy reduces so dramatically with doping is so far lacking.

I now discuss some of the obvious shortcomings of the model. I have already mentioned that the magnetic ordering wavevector in La$_{3/2}$Sr$_{1/2}$NiO$_4$ is $\mathbf{q}_m = (0.275, 0.275)$ not $(0.25, 0.25)$. Other problems are: (1) the spin-wave scattering intensity above ~ 25 meV becomes progressively more asymmetric about $\mathbf{q}_m$ with increasing energy, i.e. stronger on the side nearest to $(0.5, 0.5)$ — see Figs. 8.2(e) and (f), and Fig. 8.6(c). This asymmetry disagrees with the spin wave theory for the model described above, which predicts a symmetric scattering intensity about the magnetic zone centre. (2) The extra scattering intensity observed around $(0.5, 0.5)$ above 50 meV, and around $(1,0)$ and equivalent positions in the energy range $31 - 39$ meV suggest extra magnetic modes not present for a checkerboard ordering. (3) The spin wave scattering is very broad, implying that the spin waves propagate only a few lattice spacings before being scattered or decaying into another excitation channel. (4) The source of the low energy diffuse scattering needs to be identified.

To explain these features unequivocally we need a complete description of the static ordering, which we don't have. However, the idea that the static incommensurate order in La$_{3/2}$Sr$_{1/2}$NiO$_4$ can be understood in terms of an ideal checkerboard pattern broken up

periodically by discommensurations is physically appealing[38], and might provide some clues as to the origin of the various features in the spin excitation spectrum.

The two simplest types of discommensuration in the checkerboard pattern are illustrated in Fig. 8.9. The first (Fig. 8.9(a)) has a line of nearest-neighbour antiparallel spin pairs coupled by a superexchange interaction J expected to be close to $15\,$meV as found in the $x = 0$ and $x = 1/3$ compounds. Around the discommensuration the local hole density is below average. The second (Fig. 8.9(b)) has a line of holes on oxygen sites, which increases the local hole density and forces parallel alignment on neighbouring Ni spins through the double exchange mechanism. I will refer to these as antiferromagnetic (AFM) and ferromagnetic (FM) discommensurations. More complex discommensurations involving a greater degree of perturbation of the ideal checkerboard pattern are also possible.

Discommensurations provide a mechanism for producing an incommensurate spin density wave modulation of the checkerboard pattern, as discussed earlier. At low energies, the magnon dispersion is expected to be similar to that of the ideal checkerboard antiferromagnetic ordering, except that the magnon dispersion is shifted away from $(0.25, 0.25)$ to the incommensurate wavevector, as observed.

Let us focus, however, on the specific structure of the discommensurations themselves, which is expected to influence the spin excitation spectrum at higher energies. The AFM discommensuration can be regarded as a zig-zag chain with AFM intra-chain exchange J coupled to the checkerboard AFM background. The latter has exchange J', and $J \approx 2J'$. Above the maximum energy of the spin wave dispersion ($\sim 45\,$meV) we might expect to observe spin excitations characteristic of an AFM zig-zag chain. Because there will be discommensurations running along both diagonals the scattering will take the

(a) AFM Discommensuration
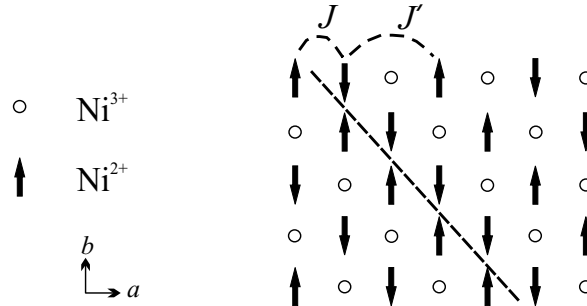
(b) FM Discommensuration
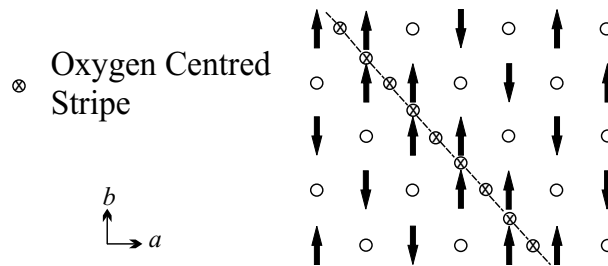
Figure 8.9: (Color online) Two types of discommensuration that could exist in La$_{3/2}$Sr$_{1/2}$NiO$_4$[38]. The spins on nearest neighbor Ni sites have (a) antiparallel and (b) parallel alignment, respectively, in the discommensuration (indicated by a dashed line). Circles and arrows denote holes and $S = 1$ spins, respectively, on the Ni sites. The encircled crosses in (b) denote the positions of an oxygen-centered charge stripe. The exchange interactions J and J' indicated in (a) couple spins on Ni^{2+} ions either on neighboring Ni sites (J) or on next-nearest-neighbor Ni sites separated by a Ni^{3+} ion (J').

form of a square of scattering dispersing away from $(0.5, 0.5)$ type positions, where the structure factor of the AFM zig-zag chain is largest. This could explain the observed 'ring' of scattering apparently dispersing from $(0.5, 0.5)$ at energies above $50\,\mathrm{meV}$. At lower energies the spin excitations will have mixed checkerboard and zig-zag chain character, and this could explain why the spin wave scattering becomes stronger on the side nearest to $(0.5, 0.5)$.

Similarly, FM discommensurations resemble FM zig-zag chains. Spin excitations with

FM zig-zag chain character are expected to be observable near to the structural zone centres. The strength of the intra-chain double exchange is not known, but this effect could account for the mode dispersing from (h, k) type positions observed in the energy range 31–39 meV.

Discommensurations could also be responsible for the substantial widths of the spin wave modes. In a region of commensurate checkerboard order a spin wave can propagate freely, but when it encounters a discommensuration the uniformity of the magnetic order is interrupted sharply, which could scatter the spin wave. In this case, the correlation length of the spin wave peaks should correspond roughly to the average spacing between discommensurations. Earlier we found the correlation length to be 24 ± 2 Å for energies in the range 25–30 meV, which corresponds to approximately $9a/\sqrt{2}$, i.e. 9 Ni positions when projected along the diagonal of the square lattice, which is the distance between discommensurations according to the model proposed by Kajimoto *et al.*[38]. Further support for the broadening mechanism proposed here can be found from a comparison of the widths of spin wave peaks observed in neutron scattering measurements of La$_{2-x}$Sr$_x$NiO$_4$ with $x = 0.275$ and $x = 1/3$ (see chapter 7). The $x = 1/3$ spin wave peaks show no measurable broadening, whereas the $x = 0.275$ peaks are broadened. This is consistent with our broadening mechanism since the stripe order of $x = 1/3$ is commensurate and without discommensurations, whereas that of $x = 0.275$ is incommensurate and does have discommensurations.

I would like to compare the spin excitations of La$_{3/2}$Sr$_{1/2}$NiO$_4$ with the spin wave excitations observed in the high temperature superconductors[25, 26, 27]. (Ignoring the fact that the zone centres of the magnetic excitations are displaced vertically and horizontally around the (1/2, 1/2) position in reciprocal space in the cuprate superconductors, com-

pared with diagonally displaced around the (1/2, 1/2) position in La$_{3/2}$Sr$_{1/2}$NiO$_4$.) In the cuprate superconductors the incommensurate spin fluctuations are observed to disperse towards the (1/2, 1/2) antiferromagnetic (AFM) position in reciprocal space with increasing energy. The incommensurate spin excitations in the cuprates merge before a higher energy mode disperses away from (1/2, 1/2) to far higher energies. The observance of only one mode dispersing out of incommensurate magnetic zone centres in the cuprates could be due to a highly anisotropic structure factor where the second mode has a very small weighting. The origin of the relatively small anisotropy of the spin excitations in La$_{3/2}$Sr$_{1/2}$NiO$_4$ could be due to the same process that cause there to be only one excitation mode at low energies in the cuprates. Above the energy where the incommensurate excitations merge the cuprates apparently have a second spin excitation mode that disperses to much higher energies. It is tempting to compare the second cuprate mode with the excitation mode above 50 meV in La$_{3/2}$Sr$_{1/2}$NiO$_4$, although I note that the excitation mode in La$_{3/2}$Sr$_{1/2}$NiO$_4$ occurs over a relatively narrow energy range.

This leaves us one remaining feature of the spin excitation spectrum to consider, namely the low energy diffuse scattering distributed around the magnetic ordering wavevectors, shown in Fig. 8.8. As mentioned earlier, this scattering has a different temperature dependence to the spin wave scattering, and from this we can conclude that it arises from a different magnetic component to the ordered spins. Low energy diffuse scattering was also observed in the spin excitation spectrum of La$_{2-x}$Sr$_x$NiO$_4$ with $x = 0.275$ and $x = 1/3$ (see chapter 7.3). In those cases the diffuse scattering was almost one-dimensional and, like the present case, there was no static component.

We attributed the quasi-1D diffuse scattering from La$_{5/3}$Sr$_{1/3}$NiO$_4$ to dynamic AFM correlations among the $S = \frac{1}{2}$ spins attached to lines of Ni^{3+} holes in the charge stripes, and

the origin of the diffuse scattering from La$_{3/2}$Sr$_{1/2}$NiO$_4$ is probably the same. Because the Ni^{3+} holes are arranged on a near-checkerboard pattern in La$_{3/2}$Sr$_{1/2}$NiO$_4$ the spin correlations among the Ni^{3+} sites are expected to be quasi-2D, consistent with the observed diffuse scattering. The slight elongation of the scattering distribution is consistent with the introduction of a stripe-like texture into the checkerboard pattern by discommensurations. The width of the peak shown in Fig. 8.8(c) is roughly twice that of an equivalent cut through the diffuse scattering from La$_{5/3}$Sr$_{1/3}$NiO$_4$. This indicates that the correlations between the Ni^{3+} spins are weaker in La$_{3/2}$Sr$_{1/2}$NiO$_4$. The interpretation of the diffuse scattering in La$_{3/2}$Sr$_{1/2}$NiO$_4$ presented here implies that there exists an AFM coupling between the Ni^{3+} spins that generates short-range fluctuations towards a checkerboard ordering. The absence of static magnetic order on the Ni^{3+} sites could have implications for recent predictions of orbital ordering in La$_{3/2}$Sr$_{1/2}$NiO$_4$[68].

Finally, it is worth comparing our results with those obtained on other checkerboard charge-ordered compounds. To our knowledge, the only other such compound whose spin excitation spectrum has been measured in detail is La$_{3/2}$Sr$_{1/2}$CoO$_4$[103]. The spin-charge order is much closer to a perfect checkerboard pattern in the half-doped cobaltate than in the half-doped nickelate. The incommensurability observed at low temperatures for La$_{3/2}$Sr$_{1/2}$CoO$_4$ is $\epsilon = 0.49$[61], compared with $\epsilon = 0.44$ for La$_{3/2}$Sr$_{1/2}$NiO$_4$. Recall that for a perfect checkerboard order $\epsilon = 0.5$. The measured spin excitation spectrum of La$_{3/2}$Sr$_{1/2}$CoO$_4$ exhibits a simple spin wave dispersion extending up 16 meV, and a second mode at energies around 30 meV which is relatively flat[103]. The spin wave dispersion does not exhibit any of the unusual features found in the case of La$_{3/2}$Sr$_{1/2}$NiO$_4$. This can be understood if, as argued above, the deviations from a simple spin wave picture are due to discommensurations: the very small incommensurability of the cobaltate implies

very few discommensurations are present. The absence of low energy diffuse scattering from the cobaltate also makes sense if the Co^{3+} ions are in a non-magnetic singlet ground state, as is believed to be the case[61].

The spin excitation spectrum of $La_{3/2}Sr_{1/2}NiO_4$ has been found to contain a number of interesting features. I have argued that the low energy diffuse scattering, which resembles a similar signal previously observed in measurements on $La_{5/3}Sr_{1/3}NiO_4$, originates from antiferromagnetic correlations among spins attached to the Ni^{3+} ions. I have also argued that other strange features in the excitation spectrum of $La_{3/2}Sr_{1/2}NiO_4$, such as the probable magnetic modes of scattering dispersing from $(0.5, 0.5)$ and $(1, 0)$ type positions and the large intrinsic widths of the spin excitations, can be understood (at least at the level of hand waving) in terms of a discommensuration model. The main obstacle in the way of a more quantitative account of the spin excitation spectrum of $La_{3/2}Sr_{1/2}NiO_4$ is the lack of a detailed model for the ground state order.

Chapter 9

Conclusions and Future work

In this thesis I have presented magnetization and neutron diffraction measurements on the ordering, and inelastic neutron scattering measurements on the spin wave excitations, of charge-ordered $La_{2-x}Sr_xNiO_{4+\delta}$.

I have found that the magnetization measurements for $0 \leq x \leq 0.5$ show a two-component magnetic irreversibility, observed through a ZFC-FC splitting. At low temperatures $(T < 50\,\text{K})$ there is a large ZFC-FC splitting, and above this temperature there is a smaller ZFC-FC splitting that persists to approximately the charge-ordering temperature. In the $x = 1/3$ material the large splitting persists approximately to the spin ordering temperature. Measurements of the remnant induced magnetization reveal two components: a fast decaying component and a slow decaying component. The remnant magnetization can mainly be described by a simple description of a two component spin glass like state that is possibly a stripe glass. The origin of a stripe glass could be due to different interaction lengths scales creating disorder, such as spin disorder at the ends of the charge stripes. A suppression of the remnant magnetization observed in the low temperature spin orientation of $x = 0.275, 1/3, 0.37$, but more prominently at $x = 1/3$, cannot be simply explained by this model.

A new unidentified transition was observed in the magnetization measurements. By use of unpolarized and polarized-neutron diffraction I found that this transition is due to a spin reorientation, where on cooling the spins rotate away from the stripe direction. The transition was found to occur in all five samples studied for $0.275 \leq x \leq 0.5$, occurring at $\sim 15\,\mathrm{K}$ for a general doping level but at $\sim 50\,\mathrm{K}$ for the $x = 1/3$ and $1/2$. The spin reorientation was observed to be approximately twice as large in the $x = 1/2$ as that for other doping levels. I also found for the ground state the spins orientated themselves at an increasingly larger angle away from the stripe direction the higher the charge-ordering temperature is. In magnetization measurements this spin reorientation was also observed to be suppressed by application of a field.

Measurements of the spin wave dispersion from the ordered Ni^{2+} spins for the $x = 0.275$ and $1/3$ indicated little variation in the interaction strengths with doping. The main difference between the observed spin wave dispersions was a relatively larger intrinsic width of the excitations at $x = 0.275$, which may be attributed to the incommensurate charge-ordering. The spin wave excitations of charge-stripe ordered $\mathrm{La}_{2-x}\mathrm{Sr}_x\mathrm{NiO}_{4+\delta}$ showed a dip in intensity centred on $E = 15 - 20\,\mathrm{meV}$. The evidence of this work suggests the dip structure is due to a coupling of the Ni^{2+} spin wave excitations to a collective motion of the stripes.

The measurements of the spin wave dispersion of the $x = 1/2$ indicated an interstripe interaction of strength $J' = 5.8 \pm 0.5\,\mathrm{meV}$. This value is only slightly lower than $J' = 7.5 \pm 1.5\,\mathrm{meV}$ for the $x = 1/3$[49], despite the occurrence of two-dimensional checkerboard charge-order in the $x = 1/2$. In the $x = 1/2$ we observe two additional modes that appear to be magnetic in origin. A qualitative explanation of these new modes can be made by considering two types of variation in the spin order period, AFM and FM

discommensurations.

We observed the out-of-plane single ion anistropy energy for $x = 0.275, 1/3, 0.37$ and $1/2$ to be greatly reduced compared to La_2NiO_4. The cause of this reduction of K_c in the doped compounds is unknown.

At low energies measurements of the spin wave excitation spectrum for $x = 0.275, 1/3$ and $1/2$ all showed an additional quasi-one-dimensional mode. In the $x = 1/3$ compound the mode was observed to be dispersive with a maximum energy of $\sim 10\,meV$. The excitation mode was observed by polarized neutron scattering in the $x = 1/3$ to be predominately out-of-plane. The results indicate that this excitation mode is due to dynamic antiferromagnetic correlations of the stripe electrons.

The spin excitations in this work are compared with a spin only model of decoupled localized Ni^{2+} and Ni^{3+} spins, but this description does not describe all the features of the spin wave excitations. In the spin wave dispersion from the Ni^{2+} spins no dip structure in the excitation intensity is predicted, and in the spin excitations from the Ni^{3+} spins no flexing of the scattering is predicted. A main conclusion of this work is that spin excitations cannot be described by decoupled localized Ni^{2+} and Ni^{3+} spins, indicating that there must be additional couplings to the spin system.

It is worth comparing the spin wave excitations observed in this work on $La_{2-x}Sr_xNiO_4$ with the spin wave excitations observed in the high temperature superconductors[25, 26, 27]. Ignoring the difference in orientation of the excitations in these two classes of materials. In the cuprate superconductors the incommensurate spin fluctuations are observed to disperse towards the (1/2, 1/2) antiferromagnetic (AFM) position in reciprocal space with increasing energy. The incommensurate spin excitations in the cuprates merge be-

fore a higher energy mode disperses away from (1/2, 1/2) to far higher energies. The dip structure observed in the intensity of the spin excitations of LSNO bears a passing resemblance to the spin excitations in the cuprates when the scattering intensity increases as the spin excitations merge at the AFM position[26, 27]. The dip structure of LSNO could also be thought of as a shift of scattering intensity from lower to high energies as the material undergoes the phase transition from a state without charge-stripe ordering for undoped La_2NiO_4, into a state with charge-stripe ordering for hole doped LSNO. In this way the dip structure resembles the shift in spin excitation intensity observed in $x = 0.16$ LSCO when the material is cooled into the superconducting phase[25]. In spin excitations of LSNO with $x = 0.275, 1/3$ and $1/2$ we observe two excitation modes from the ordered magnetic zone centres in scans parallel to $(h, h, 0)$, one that disperses towards the AFM positions and one that disperses away from the AFM positions. At $x = 1/2$, the spin excitation mode that disperses away from the AFM positions has a very weak structure factor at higher energies, whereas in the $x = 0.275, 1/3$ no strong asymmetry in the structure factor of the two excitation modes is observed. For the cuprates, it is possible that only one mode of spin excitations is observed at low energies due to the other mode having a very weak structure factor. The cause of such a strong asymmetry in the spin excitations of the cuprates clearly has little effect in charge-ordered LSNO. At higher energies in LSNO with $x = 0.275$ and $1/3$ there are no other observed spin excitations, but in the $x = 1/2$ there is an additional spin excitation mode at higher energies that disperses away from AFM positions, and at lower energies a spin excitation mode disperses away from ferromagnetic (FM) positions in reciprocal space. The two additional modes in the $x = 1/2$ are relatively flat (occurring over a narrow energy range) and can be qualitatively explained as originating from discommensurations in the charge ordering. So in LSNO at

high energies there is no observed additional mode dispersing away from AFM positions that extends over a large range of energies, unlike the cuprates. Finally, at low energies in LSNO with $x = 0.275$, 1/3 and 1/2 diffuse 1-D scattering is observed from the spins of the charge carriers in the charge stripes, whereas there has so far been no observation of such an excitation mode in the cuprates.

In this work we have studied the spin excitations of LSNO for $x \geq 0.275$. These doping levels are significantly higher than the doping levels that have been studied in the high temperature superconductors[25, 26, 27]. As the cuprates have been studied at lower doping levels the incommensurability of the magnetic excitations is smaller than in lSNO with $x \geq 0.275$. This means a comparison of the spin excitations of a cuprate and a LSNO material with a similar value of the incommensurability has not been carried out. At such low doping levels ($x < 0.2$) the charge order in LSNO becomes very short range, so the LSNO system does not appear to provide a model charge-ordered system in which to study a material with an incommensurability as small as the cuprates. Another model charge-ordered system must be found to carry out such a comparison.

There are similarities between the incommensurate spin excitations in the cuprates to the spin excitations from the ordered Ni^{2+} spins in charge-ordered LSNO but the work carried out in this thesis shows there are significant differences. Identifying the causes of the differences in the spin excitations of cuprates and charge-ordered LSNO could play an important part in understanding charge-ordering and what its role is in high temperature superconducting materials.

After this work there are still details that are unknown about the ordered state of $La_{2-x}Sr_xNiO_{4+\delta}$. First of all there is no complete ground state model of $La_{3/2}Sr_{1/2}NiO_{4+\delta}$

: phase separation into part commensurate state without spin order and part incommensurate state with spin order has not been ruled out yet by experiment[38]. A μSR study of two closely doped materials with $x = 1/2$ and $x < 1/2$ should be able to determine the fraction of the $x = 1/2$ that is magnetically ordered compared with the $x < 1/2$, so determining whether the Ni^{2+} spins in the $x = 1/2$ are fully ordered or partially ordered. Below $x \sim 0.2$ stoichiometric single crystals of $La_{2-x}Sr_xNiO_{4+\delta}$ are hard to grow, but stoichiometric polycrystalline samples can be made. Powder neutron diffraction could be used to study the magnetic ground state between $0 < x < 0.2$. In this doping region one could study the transition from the Néel state, and could search for phase separation which has been reported to occur in the Néel state of $La_{2-x}Sr_xCuO_4$[21].

The measurements from inelastic neutron scattering presented in this thesis have revealed features that cannot be explained by a simple model of two non-interacting spin systems, i.e. (i) the ordered Ni^{2+} spins and (ii) the spins on the Ni^{3+} ions created by hole doping. Further inelastic neutron scattering measurements can be carried out to investigate the coupling between these two spin systems. For example, the temperature dependence of the dip structure in the spin excitation spectrum could be investigated and compared to the temperature dependencies of the low energy excitations from the ordered Ni^{2+} spins and the correlations of the charge stripe electrons. A correlation between the temperature dependence of the dip structure and that of the low energy excitations of the Ni^{3+} spins would indicate that a coupling between the two spin systems causes the dip structure. My co-researchers in the work of this thesis have proposed an experiment to measure the temperature dependence of the dip structure. An investigation of the effect of decoupling the spin systems by application of a magnetic field could also be insightful. The application of a magnetic field could drive the antiferromagnetic correlations of the Ni^{3+} spins into

a static ordering, so that there would be ordered 1-D spin-1/2 antiferromagnetic chains embedded in the relatively 3 dimensionally ordered Ni^{2+} spins. A magnetic field could also be employed to determine if the magnetic ordering can be enhanced so that there is no variation away from $\varepsilon = x$ ordering, this would establish the relative strengths of the charge and spin ordering in driving the periodicity of the charge-stripe structure.

Appendix A

Linear Spin Wave Calculation of a Checkerboard Charge-ordering.

The strengths of the magnetic interactions in $\mathrm{La_{3/2}Sr_{1/2}NiO_{4+\delta}}$ were estimated from comparison of the data to the linear spin wave model of an deal checkerboard charge ordered state on a square lattice. Figure A.1 shows the model of an ideal checkerboard charge-ordered state for site centred charge ordering on a square lattice, where the charges reside on the metallic sites. In the ideal ordering there two sublattices of spins, sublattice 1 where the spin point downwards and sublattice 2 where the spins point upwards. The two sublattices interact through a next nearest neighbour interaction across the charge ordering J'. We considered a spin only Heisenberg model with the Hamiltonain;

$$H = J' \sum_{\langle i,j \rangle} \mathbf{S}_i \cdot \mathbf{S}_j + K_c \sum_{\mathbf{i}} (\mathbf{S}_i^z)^2, \tag{A.1}$$

where the first summation describes the exchange interactions between pairs of ordered spins in along Ni$-$O$-$Ni linear bonds along x or y, and the second summation describes the small, XY-like, single-ion anisotropy. Here, as in Ref. [49], J' is defined as the exchange energy *per spin* (multiply by 2 to obtain the exchange energy *per bond*). We neglect the diagonal exchange couplings between Ni^{2+} sites which are needed to stabilize

the spin arrangement but are assumed to be small relative to J'. We also neglect any in-plane-anisotropy gap, as experiments place an upper limit of $0.4\,\mathrm{meV}$ on this gap. In effect the system is treated as two uncoupled square-lattice antiferromagnets with lattice parameter $2a$.
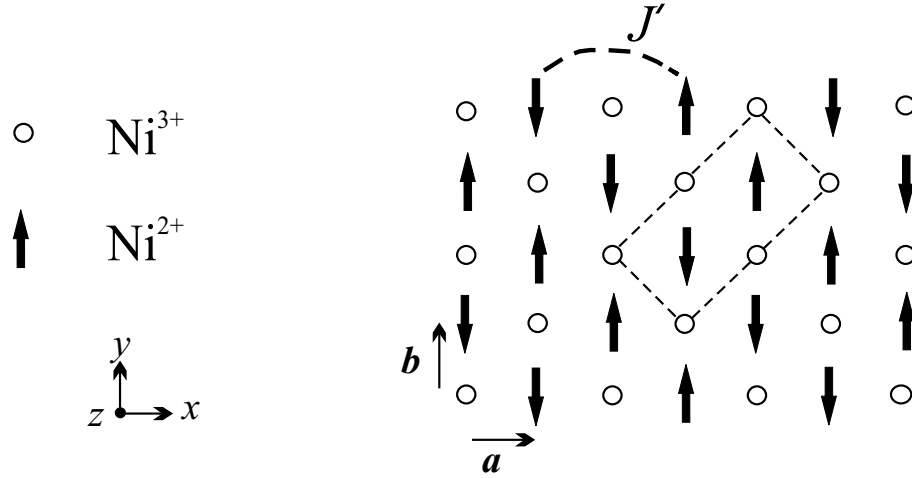

Figure A.1: Ideal checkerboard spin–charge ordering in a NiO_2 square lattice. Circles represent Ni^{3+} holes, and solid arrows represent spins on Ni^{2+} sites. The broken lines indicate the magnetic unit cell of the ideal checkerboard spin–charge ordering. J' is the exchange coupling parameter of the Ni^{2+} spins across the Ni^{3+} site. With the base vectors a and b of the crystal latice indicated.

By using the linear approximation of the Holstein-Primakoff transformation this Hamiltonian is transformed into Bose operators. For the sublattice with the spins pointing down the transformations are;

$$S_{\mathbf{m}}^{y} = S - \mathbf{a}_{\mathbf{m}}^{+}\mathbf{a}_{\mathbf{m}} \tag{A.2}$$

$$S_{\mathbf{m}}^{+} = S_{\mathbf{m}}^{z} + iS_{\mathbf{m}}^{x} = (2S)^{1/2}\mathbf{a}_{\mathbf{m}} \tag{A.3}$$

$$S_{\mathbf{m}}^{-} = S_{\mathbf{m}}^{z} - iS_{\mathbf{m}}^{x} = (2S)^{1/2}\mathbf{a}_{\mathbf{m}}^{+} \tag{A.4}$$

$$S_{\mathbf{m}}^{z} = \left(\frac{S}{2}\right)^{1/2}(\mathbf{a}_{\mathbf{m}} + \mathbf{a}_{\mathbf{m}}^{+}) \tag{A.5}$$

$$S_{\mathbf{m}}^{x} = \left(\frac{S}{2}\right)^{1/2}\frac{1}{i}(\mathbf{a}_{\mathbf{m}} - \mathbf{a}_{\mathbf{m}}^{+}) \tag{A.6}$$

where $S_{\mathbf{m}}^y$ is the spin component in the y direction of the spin at position $\mathbf{m}$, S is the magnitude of the spin, $\mathbf{a}_{\mathbf{m}}^+$ creates a magnon at position $\mathbf{m}$ and $\mathbf{a}_{\mathbf{m}}$ destroys a a magnon at position $\mathbf{m}$.

After performing the Holstein-Primakoff transformation, we Fourier transform the Hamiltonian into reciprocal space, where

$$\mathbf{a_q} = \frac{1}{\sqrt{N}} \sum_{\mathbf{m}} e^{-i\mathbf{q}.\mathbf{m}} \mathbf{a_m} \tag{A.7}$$

$$\mathbf{a_q^+} = \frac{1}{\sqrt{N}} \sum_{\mathbf{m}} e^{i\mathbf{q}.\mathbf{m}} \mathbf{a_m^+} \tag{A.8}$$

where N is total number of spins of the sublattice. Then diagonalize the Hamiltonian using the Bogoliubov transformation.

To determine magnon dispersion this Hamiltonain H is then solved by calculating the eigenvalues of:

$$|gH - \lambda_i I| = 0 \tag{A.9}$$

where I is the identity matrix, λ_i are the eigenvalues and from the commutation relations of the Bogoliubov spin operators g is

$$g = \begin{pmatrix} 1 & 0 & 0 & 0 \\ 0 & 1 & 0 & 0 \\ 0 & 0 & -1 & 0 \\ 0 & 0 & 0 & -1 \end{pmatrix} \tag{A.10}$$

Leading to the magnon dispersion:

$$E(\mathbf{Q}) = 8J'S\{(1 + K_c/8J')^2 - [\gamma(\mathbf{Q}) \pm K_c/8J']^2\}^{1/2}, \tag{A.11}$$

where

$$\gamma(\mathbf{Q}) = \frac{1}{2}[\cos(2Q_x a) + \cos(2Q_y a)]. \tag{A.12}$$

There are two dispersion branches, where the splitting of the two branches of the dispersion curve is such that at the magnetic zone centre one mode is gapped and the other isn't. The size of the gap is $4S(2J'K_c)^{1/2}$. When $K_c \ll J'$ the maximum energy of the dispersion curve is approximately $8J'S$. In figure A.2 I show the dispersion from this linear spin wave calculation for $S = 1$, the exchange parameter $J' = 5.8\,\text{meV}$ and out-of-plane anisotropy $K_c = 0.05\,\text{meV}$ (the values estimated in our work for the exchange interactions of $\text{La}_{3/2}\text{Sr}_{1/2}\text{NiO}_4$).
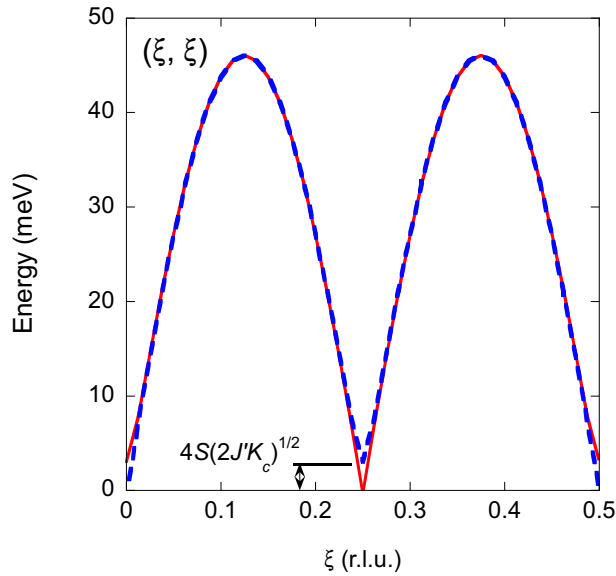
Figure A.2: The calculated dispersion of the magnetic excitations in an $S = 1$ ideal checkerboard charge-ordered material. Solid and broken lines are the two branches of the spin waves for a checkerboard ordered system with the exchange parameter $J' = 5.8\,\text{meV}$ and out-of-plane anisotropy $K_c = 0.05\,\text{meV}$. At the magnetic zone centre the two branches of the dispersion curve are separated at low energies by a small anisotropy gap of $4S(2J'K_c)^{1/2}$.

References

[1] J. G. Bednorz and K. A. Müller, Z. Phys. B **64**, 189 (1986).

[2] J. Bardeen, L. N. Cooper, and J. R. Schrieffer, Phys. Rev. **102**, 1175 (1957).

[3] J. M. Tranquada, B. J. Sternleib, J. D. Axe, Y. Mkaamura and S. Uchida, Nature (London) **375**, 561 (1995); J. M. Tranquada, J. D. Axe, N. Ichikawa, Y. Nakamura, S. Uchida and B. Nachumi, Phys. Rev. B **54**, 7489 (1996).

[4] V. J. Emery, S. A. Kivelson and O. Zachar, Phys. Rev. B **56**, 6120 (1997); Yu. A. Krotov, D-H. Lee and A. V. Balatsky, Phys. Rev. B **56**, 8367 (1997).

[5] R. J. Cava, B. Batlogg, T. T. Palstra, J. J. Krajewski, W. F. Peck, Jr., A. P. Ramirez, and L. W. Rupp, Jr., Phys. Rev. B **43**, 1229 (1991).

[6] K. Sreedhar and J. M. Honig, J Sol. State Chem. **111**, 147 (1994)

[7] J. M. Tranquada, J. E. Lorenzo, D. J. Buttrey and V. Sachan , Phys. Rev. B **52**, 3581 (1995).

[8] M. Kato, Physica B 312-313, 545 (2002)

[9] H. J. Schulz, J. Phys. France **50**, 2833 (1989); H. J. Schulz, Phys. Rev. Lett. **64**, 1445 (1989).

[10] D. Poilblanc, and T. M. Rice , Phys. Rev. B **39**, 9749 (1989).

[11] V. J. Emery, and S. A. Kivelson, Physica C **209**, 597 (1993).

[12] J. Zaanen, and O. Gunnarsson, Phys. Rev. B **40**, 7391 (1989).

[13] K. Machida, Physica C **158**, 192 (1989).

[14] B. Batlogg, A. P. Ramirez, R. J. Cava, R. B. van Dover, and E. A. Rietman, Phys. Rev. B **35**, 5340 (1987).

[15] T. R. Thurston, R. J. Birgeneau, M. A. Kastner, N.W. Preyer, G. Shirane, Y. Fujii, K. Yamada, Y. Endoh, K. Kakurai, M. Matsuda,Y. Hidaka and T. Murakami , Phys. Rev. B **40**, 4585 (1989); S-W. Cheong, G.Aeppli, T. E. Mason, H. Mook, S. M. Hayden,

P. C. Canfield, Z. Fisk, K. N. Clausen and J. L. Martinez, Phys. Rev. Lett. **67**, 1791 (1991); T. E. Mason, G. Aeppli, and H. A. Mook, Phys. Rev. Lett. **68**, 1414 (1992); T. R. Thurston, P. M. Gehring, G. Shirane, R. J. Birgeneau, M. A. Kastner, Y. Endoh, M. Matsuda, K. Yamada, H. Kojima and I. Tanaka, Phys. Rev. B **46**, 9128 (1992).

[16] F. C. Chou, N. R. Belk, M. A. Kastner, R. J. Birgeneau, and Amnon Aharony, Phys. Rev. Lett. **75**, 2204 (1995).

[17] B. Battlogg and C. Varma, Physics World, Vol. 3, No. 2, 33 (2000)

[18] A. R. Moodenbaugh, Youwen Xu, M. Suenaga, T. J. Folkerts and R. N. Shelton, Phys. Rev. B **387**, 4596 (1988).

[19] K. Yamada, C. H. Lee, K. Kurahashi, J. Wada, S. Wakimoto, S. Ueki, H. Kimura, Y. Endoh, S. Hosoya, G. Shirane, R. J. Birgeneau, M. Greven, M. A. Kastner, and Y. J. Kim, Phys. Rev. B **57**, 6165 (1998).

[20] S. Wakimoto, G. Shirane, Y. Endoh, K. Hirota, S. Ueki, K. Yamada, R. J. Birgeneau, M. A. Kastner, Y. S. Lee, P. M. Gehring and S. H. Lee, Phys. Rev. B **60**, R769 (1999); S. Wakimoto, R. J. Birgeneau, M. A. Kastner, Y. S. Lee, R. Erwin, P. M. Gehring, S. H. Lee, M. Fujita, K. Yamada, Y. Endoh ,K. Hirota and G. Shirane, Phys. Rev. B **61**, 3699 (2000); M. Matsuda, M. Fujita, K. Yamada, R. J. Birgeneau, M. A. Kastner, H. Hiraka, Y. Endoh, S. Wakimoto and G. Shirane, Phys. Rev. B **62**, 9148 (2000).

[21] M. Matsuda, M. Fujita, K. Yamada, R. J. Birgeneau, Y. Endoh and G. Shirane, Phys. Rev. B **65**, 134515 (2002).

[22] M. Fujita, K. Yamada, H. Hiraka, P. M. Gehring, S. H. Lee, S. Wakimoto and G. Shirane, Phys. Rev. B **65**, 064505 (2002).

[23] A. Lucarelli, S. Lupi, M. Ortolani, P. Calvani, P. Maselli, M. Capizzi, P. Giura, H. Eisaki, N. Kikugawa, T. Fujita, M. Fujita, and K. Yamada, Phys. Rev. Lett. **90**, 037002 (2003)

[24] L. Tassini, F. Venturini, Q.-M. Zhang, R. Hackl, N. Kikugawa, T. Fujita, cond-mat/0406169

[25] N. B. Christensen, D. F. McMorrow, H. M. Rønnow, B. Lake, S. M. Hayden, G. Aeppli, T. G. Perring, M. Mangkorntong, M. Nohara, and H. Takagi, Phys. Rev. Lett. **93**, 147002 (2004).

[26] J. M. Tranquada, H. Woo, T. G. Perring, H. Goka, G. D. Gu, G. Xu, M. Fujita, K. Yamada, Nature (London) **429**, 534 (2003).

[27] S. M. Hayden, H. A. Mook, P. Dai, T. Perring, F. Doğan, Nature (London) **429**, 531 (2003).

[28] G.S. Uhrig, K.P. Schmidt, and M. Grninger, J. Mag. Mag. Mater. 290-291, 330 (2005).

[29] G. Seibold, and J. Lorenzana, Phys. Rev. Lett. 94, 107006 (2005).

[30] V.I. Anisimov, M.A. Korotin, A.S. Mylnikova, A.V. Kozhevnikov, and J. Lorenzana, Phys. Rev. B 70, 172501 (2004)

[31] B. M. Andersen, and P. Hedegård, cond-mat/0411065 (2004).

[32] S. M. Hayden, G. H. Lander, J. Zarestky, P. J. Brown, C. Stassis, P. Metcalf and J. M. Honig, Phys. Rev. Lett. **68**, 1061 (1992); V. Sachan, D. J. Buttrey, J. M. Tranquada, J. E. Lorenzo, and G. Shirane, Phys. Rev. B **51**, 12742 (1995); J. M. Tranquada, D. J. Buttrey, and V. Sachan, Phys. Rev. B **54**, 12318 (1996).

[33] S-H. Lee and S.-W. Cheong, Phys. Rev. Lett. **79**, 2514 (1997).

[34] H. Yoshizawa, T. Kakeshita, R. Kajimoto, T.Tanabe, T. Katsufuji and Y. Tokura, Phys. Rev. B **61**, R854 (2000); H. Yoshizawa, T. Kakeshita, R. Kajimoto, T. Tanabe, T. Katsufuji and Y. Tokura, Physica B 241-243, 880 (1998).

[35] S-H. Lee, S.-W. Cheong, K. Yamada, and C. F. Majkrzak, Phys. Rev. B **63**, R060405 (2001).

[36] R. Kajimoto, T. Kakeshita, H. Yoshizawa, T. Tanabe, T. Katsufuji, and Y. Tokura, Phys. Rev. B **64**, 144432 (2001).

[37] S.-H. Lee, J. M. Tranquada, K. Yamada, D. J. Buttrey, Q. Li, and S.-W. Cheong, Phys. Rev. Lett. **88**, 126401 (2002).

[38] R. Kajimoto, K. Ishizaka, H. Yoshizawa, and Y. Tokura, Phys Rev B **67**, 014511 (2003).

[39] K. Ishizaka, T. Arima, Y. Murakami, R. Kajimoto, H. Yoshizawa, N. Nagaosa, and Y. Tokura, Phys. Rev. Lett. **92**, 196404 (2004)

[40] E. D. Isaacs, G. Aeppli, P. Zschack, SW. Cheong, H. Williams, and D. J. Buttrey *et al.*, Phys. Rev. Lett. **72**, 3421 (1994); A. Vigliante, M. von Zimmermann, J. R. Schneider, T. Frello, N. H. Andersen, J. Madsen, D. J. Buttrey, Doon Gibbs and J. M. Tranquada, Phys. Rev. B **56**, 8248 (1997).

[41] C-H. Du, M. E. Ghazi, Y. Su, I. Pape, P. D. Hatton, S. D. Brown, W. G. Stirling, M. J. Cooper, and S-W. Cheong, Phys. Rev. Lett. **84**, 3911 (2000).

[42] P. D. Hatton, M. E. Ghazi, S. B. Wilkins, P. D. Spencer, D. Mannix , T. d'Almeida, D. Prabhakaran , A. Boothroyd, S.-W. Cheong, Physica B **318**, 289 (2002).

[43] M. E. Ghazi, P. D. Spencer, S. B. Wilkins, P. D. Hatton, D. Mannix , T. d'Almeida, D. Prabhakaran , A. Boothroyd, S.-W. Cheong, Phys. Rev. B **70**, 144507 (2004).

[44] G. Blumberg, M. V. Klein, and S-W. Cheong, Phys. Rev. Lett. **80**, 564 (1998).

[45] Yu. G. Pashkevich, V. A. Blinkin, V. P. Gnezdilov, V. V. Tsapenko, V. V. Eremenko, P. Lemmens, M. Fischer, M. Grove, G. Guntherodt, L. Degiorgi, P. Wachter, J. M. Tranquada, and D. J. Buttrey, Phys. Rev. Lett. **84**, 3919 (2000).

[46] P. Calvani, A. Paolone, P. Dore, S. Lupi, P. Maselli, P. G. Medaglia and S -W. Cheong, Phys. Rev. B **54**, R9592 (1996).

[47] J. H. Jung, D.-W. Kim, T. W. Noh,H. C. Kim, H.-C. Ri, S. J. Levett, M. R. Lees, D. McK. Paul, and G. Balakrishnan, Phys. Rev. B **64**, 165106 (2001).

[48] P. Wochner, J. M. Tranquada, D. J. Buttrey, and V. Sachan, Phys. Rev. B **57**, 1066 (1998).

[49] A. T. Boothroyd, D. Prabhakaran, P. G. Freeman, S. J. S. Lister, M. Enderle, A. Hiess, and J. Kulda, Phys. Rev. B **67**, 100407(R) (2003).

[50] T. Katsufuji, T. Tanabe, T. Ishikawa, S. Yamanouchi, Y. Tokura,T. Kakeshita, R. Kajimoto, and H. Yoshizawa, Phys. Rev. B 60, R5097(1999).

[51] M. Kato, Y. Maeno and T. Fujita, J. Phys Soc. Jap. **60**, 1994 (1991); W-J Jang and H. Takei, Jap. J Applied Phys. **30**, 251 (1991); G. H. Lander, K. Westerholt and H. Bach, Phys. Rev. B **43**, 448 (1991); Th Strangfeld, K. Westerhold and H. Bach, Physcia C **183**, 1 (1991); S-W. Cheong, H. Y. Hwang, C. H. Chen, B. Batlogg, L. W. Rupp Jr., and S. A. Carter , Phys. Rev. B **49**, 7088 (1994).

[52] Tuson Park, Z. Nussinov, K. R. A. Hazzard, V. A. Sidorov, A. V. Balatsky, J. L. Sarrao, S.-W. Cheong, M. F. Hundley, Jang-Sik Lee, Q. X. Jia, and J. D. Thompson, Phys. Rev. Lett. **94**, 017002 (2005).

[53] T. Katsufuji, T. Tanabe, T. Ishikawa, Y. Fukuda, T. Arima, and Y. Tokura, Rev. B **54**, 14230 (1996).

[54] C. Hess, B. Bchner, M. Hcker, R. Gross, and S-W. Cheong, Phys. Rev. B **59**, R10397 (1999).

[55] K. Yamamoto, T. Katsufuji, T. Tanabe, and Y. Tokura , Phys. Rev. Lett. **80**, 1493 (1998).

[56] Personal communications with S. Blundell (2003).

[57] A. P. Ramirez, P. L. Gammel, S-W. Cheong, D. J. Bishop, and P. Chandra, Phys. Rev. Lett. **76**, 447 (1996).

[58] A. Matsushita, T. Matsumoto, S. Takayanagi, and N. Mori, Physica B **165-166**, 1351 (1990); M. Kato, Y. Maeno, and T. Fujita, J. Phys. Soc. Jap. **60**, 1994 (1991).

[59] C. H. Chen, S-W. Cheong, and A. S. Cooper, Phys. Rev. Lett. **71**, 2461 (1993).

[60] Y. Moritomo, Y. Tomioka, A. Asamitsu, Y. Tokura, and Y. Matsui, Phys. Rev. B **51**, R3297 (1995); B. J. Sternlieb, J. P. Hill, U. C. Wildgruber, G. M. Luke, B. Nachumi, Y. Moritomo, and Y. Tokura, Phys. Rev. Lett. **76**, 2169 (1996); Y. Murakami, H. Kawada, H. Kawata, M. Tanaka, T. Arima, Y. Moritomo, and Y. Tokura, Phys. Rev. Lett. **80**, 1932 (1998).

[61] I. A. Zaliznyak, J. P. Hill, J. M. Tranquada, R. Erwin, and Y. Moritomo, Phys. Rev. Lett. **85**, 4353 (2000).

[62] J. E. Hoffman, E. W. Hudson, K. M. Lang, V. Madhavan, H. Eisaki, S. Ucida and J. C. Davis, Science **295**, 466 (2002).

[63] T. Hanaguri, C. Lupien, Y. Kohsaka, D.-H. Lee, M. Azuma, M. Takano, H. Takagi and J. C. Davis, Nature **430**, 1001 (2004).

[64] H-D. Chen, J-P. Hu, S. Capponi, E. Arrigoni, and S-C. Zhang, Phys. Rev. Lett. **89**, 137004 (2002)

[65] B. M. Andersen, P. Hedegård, and H. Bruus, Phys. Rev. B **67**, 134528 (2003)

[66] B. Lake, G. Aeppli, K. N. Clausen, D. F. McMorrow, K. Lefmann, N. E. Hussey, N. Mangkorntong, M. Nohara, H. Takagi, T. E. Mason, and Schroder A , Science **291**, 1759 (2001); B. lake, H. M. Ronnow, N. B. Christensen, G. Aeppli, K. Lefmann, D. F. McMorrow, P. Vorderwisch, P. Smeibidl, N. Mangkorntong, T. Sasagawa, M. Nohara, H. Takagi, and T. E. Mason, Nature (London) **415**, 299 (2002).

[67] K. Yamamoto, K. Ishizaka, E. Saitoh, S. Shinomori, T. Tanabe, T. Katsufuji, and Y. Tokura , Phys Rev B **67**, 014414 (2003).

[68] T. Hotta and E. Dagotto, Phys. Rev. Lett. **92**, 227201 (2004).

[69] Jianqi Li, Yimei Zhu, J. M. Tranquada, K. Yamada and D. J. Buttrey, Phys. Rev. B **67**, 012404 (2003).

[70] I. M. Abu-Shiekah, O. Bakharev, H. B. Brom and J. Zaanen, Phys. Rev. Lett. **87**, 237201 (2001).

[71] E. Winkler, F. Rivadulla, J.-S. Zhou, and J. B. Goodenough, Phys. Rev. B **66**, 094418 (2002).

[72] J. M. Tranquada, P. Wochner, A. R. Moodenbaugh, and D. J. Buttrey, Phys. Rev. B **55**, R6113 (1999).

[73] P. Kuiper, J. Van Elp, G. A. Sawatzky, A. Fujimori, S. Hosoya and D. M. De Leeuw, Phys. Rev. B **44**, 4570 (1991).

[74] P. Bourges, Y. Sidis, M. Braden, K. Nakajima, and J.M. Tranquada , Phys. Rev. Lett. **90**, 147202 (2003).

[75] F. Krüger, and S. Scheidl, Phys. Rev. B **67**, 134512 (2003).

[76] E. W. Carlson, D.X. Yuo and D. K. Campbell, Phys. Rev. B **70**, 064505 (2004).

[77] S. W. Lovesey, Theory of Neutron Scattering from Condensed Matter (Oxford University Press, Oxford, U.K. 1984).

[78] G. L. Squires, Introduction to the Theory of Thermal Neutron Scattering, (Dover Publications Inc., Minoela, New York, U.S.A., 1996).

[79] R. M. Moon, T. Riste, and W. C. Koehler, Phys. Rev. **181**, 920 (1969).

[80] L. Pintschovius, J. M. Bassat, P. Odier, F. Gervais, G. Chevrier, W. Reichardt, and F. Gompf, Phys. Rev. B **40**, 2229 (1989).

[81] D. Prabhakaran, P. Isla, and A. T. Boothroyd, J. Cryst. Growth **237**, 815 (2002).

[82] P. G. Freeman, A. T. Boothroyd, D. Prabhakaran, and D. González, J. Mag. Mag. Mater. 272-276, Part 2, 958 (2004).

[83] Th. Jestädt, K. H. Chow, S. J. Blundell, W. Hayes, F. L. Pratt, B. W. Lovett, M. A. Green, J. E. Millburn, and M. J. Rosseinsky, Phys. Rev. B **59**, 3775 (1999).

[84] J. M. Tranquada, D. J. Buttrey, D. E. Rice, Phys. Rev. Lett. **70**, 445 (1993).

[85] J. M. Tranquada, D. J. Buttrey, V. Sachan, and J. E. Lorenzo, Phys. Rev. Lett. **73**, 1003 (1994).

[86] J. M. Tranquada, P. Wochner and D. J. Buttery, Phys. Rev. Lett. **79**, 2133 (1997).

[87] N. Poirot-Reveau, P. Odier, P. Simon, and F. Gervais, Phys. Rev. B **65**, 094503 (2002).

[88] I. A. Campbell, Phys. Rev. B **37**, 9800(1988).

[89] P. G. Freeman, A. T. Boothroyd, D. Prabhakaran, D. González and M. Enderle, Phys. Rev. B **66**, 212405 (2002).

[90] J. Schmalian, and P. G. Wolynes, Phys. Rev. Lett. **85**, 836 (1997).

[91] P. Sibani, and H. J. Jensen, JSTAT P10013 (2004).

[92] Young Sun, M. B. Salamon, K. Garnier, and R. S. Averback, Phys. Rev. Lett. **91**, 167206 (2003).

[93] M. Sasaki, P. E. Jönsson, H. Takayama, and H. Mamiya, Phys. Rev. B **71**, 104405 (2005).

[94] P. G. Freeman, A. T. Boothroyd, D. Prabhakaran, M. Enderle, and C. Niedermayer, Phys. Rev. B **70**, 024413 (2004).

[95] A. T. Boothroyd, P. G. Freeman, D. Prabhakaran, H. Woo, K. Nakajima, J. M. Tranquada, K. Yamada and C. D. Frost, J. Mag. Mag. Mater. 272-276, Part 1, 265 (2004).

[96] A. T. Boothroyd, P. G. Freeman, D. Prabhakaran, M. Enderle, and J. Kulda, Physica B **345**, 1-5 (2004).

[97] A. T. Boothroyd, P. G. Freeman, D. Prabhakaran, A. Hiess, M. Enderle, J. Kulda, and F. Altorfer, Phys. Rev. Lett. **91**, 257201 (2003).

[98] K. Nakajima, K. Yamada, S. Hosoya, T. Omata and Y. Endoh, J. Phys. Soc. Jpn. **62**, 4438 (1993).

[99] H. Woo, A. T. Boothroyd, K. Nakajima, T.G. Perring, C. D. Frost, P. G. Freeman, D. Prabhakaran, K. Yamada and J. M. Tranquada, unpublished.

[100] J. des Cloizeaux and J. J. Pearson, Phys. Rev. **128**, 2131 (1962).

[101] J. Zaanen, and P. B. Littlewood, Phys. Rev. B **50**, 7222 (1994).

[102] P. G. Freeman, A. T. Boothroyd, D. Prabhakaran, C. D. Frost, M. Enderle, and A. Heiss, Phys. Rev. B **71**, 174412 (2005).

[103] L. M. Helme, A. T. Boothroyd, D. Prabhakaran, F. R. Wondre, C. D. Frost, and J. Kulda, Physica B **350**, e273 (2004).